

University of Southampton Research Repository

Copyright © and Moral Rights for this thesis and, where applicable, any accompanying data are retained by the author and/or other copyright owners. A copy can be downloaded for personal non-commercial research or study, without prior permission or charge. This thesis and the accompanying data cannot be reproduced or quoted extensively from without first obtaining permission in writing from the copyright holder/s. The content of the thesis and accompanying research data (where applicable) must not be changed in any way or sold commercially in any format or medium without the formal permission of the copyright holder/s.

When referring to this thesis and any accompanying data, full bibliographic details must be given, e.g.

Thesis: Author (Year of Submission) "Full thesis title", University of Southampton, name of the University Faculty or School or Department, PhD Thesis, pagination.

Data: Author (Year) Title. URI [dataset]

University of Southampton

Faculty of Engineering and Physical Sciences

School of Electronics and Computer Science

Nanocellulose-based Battery Electrodes

by

Evangelia Founta

ORCID ID <u>0000-0001-6459-8417</u>

Thesis for the degree of Doctor of Philosophy

June 2025

University of Southampton Abstract

Faculty of Engineering and Physical Sciences
School of Electronics and Computer Science

<u>Doctor of Philosophy</u>

Nanocellulose-based Battery Electrodes

by

Evangelia Founta

Modern wearable electronic devices are limited by the development of power sources that are mechanically flexible and safe at the same time. The development of flexible Li-ion batteries has been demonstrated; however, the remaining challenges include the re-design of all battery components in order to make each one flexible. Graphite electrodes are the most widely used anodes in Li-ion batteries, but their conventional structure suffers from rigidity and brittleness. Here, nanocellulose which is a natural biopolymer, is integrated with graphite and is used as component for the fabrication of inherently flexible electrodes, that also address battery sustainability concerns.

In this work, flexible nanocellulose/graphite electrodes are manufactured, and their mechanical and electrochemical performance characteristics are examined via SEM, AFM, CV and EIS in Liion environment. The electrode can undergo a deformation of a 180° bending angle, trading-off 1/3 of conductivity. It is also shown that nanocellulose not only works as a flexible additive, but it can also promote ion mass transport, enabling ion access from the electrolyte, even to the bulk of the graphite electrode with reduced diffusion limitations. Parameters like nanocellulose content and nanoarchitecture are also correlated with fluctuations in ion mass transport. Molecular interactions between Li-ions and nanocellulose are examined by solid state NMR.

Wearable devices where safety is of crucial importance would potentially benefit more by the implementation of beyond Li-ion technologies, like aluminum-graphite batteries which are inherently safe. In this case, nanocellulose/graphite electrodes are also tested in the Al-ion battery chemistry and are proven to improve mass transport properties by 17%. This demonstrates the versatility of nanocellulose in different battery chemistries.

This work offers a perspective on the material-driven design of flexible nanocellulose/graphite electrodes, by investigating the contribution of nanocellulose to charge storage mechanisms and mechanical resilience, aligning with modern energy storage requisites. The use of nanocellulose/graphite electrodes in both Li-ion and Al-ion systems paves the way towards the diversification of the battery market.

Table of Contents	3
Table of Tables	8
Table of Figures	9
Research Thesis: Declaration of Authorship	17
Acknowledgements	18
Definitions and Abbreviations	21
Chapter 1 Introduction	26
1.1 The need for flexible and sustainable energy storage solutions	26
1.2 From cellulose to nanocellulose	27
1.3 Li-ion and beyond: the future of energy storage	28
1.3.1 Improving Li-ion batteries	28
1.3.2 Beyond Li-ion: The case of aluminium-graphite batteries	29
1.4 Electrode design and operation hypothesis	30
1.5 Aims and Objectives	31
1.6 Novel contributions of this work	32
Chapter 2 Literature review	33
2.1 Cellulose and nanocellulose fundamentals	33
2.1.1 Classification and isolation methods	33
2.1.1.1 Other methods for nanofibril synthesis	36
2.1.1.1.1 Electrospinning	36
2.1.2 Surface modification techniques	36
2.1.3 Integration strategies	38
2.1.4 Why is nanocellulose considered for energy storage applications?	39
2.2 State of the art in cellulose and nanocellulose-based flexible batteries	40
2.2.1 Considerations	40
2.2.2 Nanocellulose in Lithium-ion batteries	<i>1</i> 1
2.2.2 Nanocollatoso in Ellinani-lon pattorios	— '

		2.2.2.2 Graphite electrodes	42
2.3	3 Alu	minium-graphite rechargeable batteries	48
	2.3.1	Operation mechanism	48
	2.3.2	Challenges and remaining progress	52
2.4	l Cha	arge storage mechanisms in electrochemical systems	53
	2.4.1	Categories	53
	2.4.2	Current deconvolution and quantifying	55
Cha	apter 3	3 Experimental Methods	57
3.1	I Ele	ctrode fabrication	57
	3.1.1	Preparation of nanocellulose/graphite electrodes (NCF/G)	57
	3.1.2	Preparation of electrospun cellulose nanofiber/graphite electrodes	58
		3.1.2.1 Nanocellulose electrospinning	58
		3.1.2.2 Fabrication of electrospun cellulose nanofiber/graphite electros	les
		(EL-NCF/G)	58
3.2	2 Stru	uctural characterisation techniques	58
	3.2.1	Scanning electron microscopy	58
	3.2.2	Atomic force microscopy	59
	3.2.3	Solid-state nuclear magnetic resonance spectroscopy	59
3.3	B Pre	paration of electrochemical cells	60
	3.3.1	Three-electrode cell for assessment in Li-ion environment	60
	3.3.2	Aluminium-graphite two-electrode cells	61
3.4	l Ele	ctrochemical characterisation techniques	62
	3.4.1	Cyclic voltammetry	62
	3.4.2	Electrochemical impedance spectroscopy	63
	3.4.3	Galvanostatic cycling	63
3.5	5 Fle	xibility tests	63
	3.5.1	Electrochemical impedance spectroscopy under flexion of electrode	63
	3.5.2	Electrochemical impedance spectroscopy under flexion of full aluminium	1-
		graphite pouch cell	64

3.6	Pre	paration	of covalently bonded electrode/electrolyte interface	.65
	3.6.1	Preparat	tion of deposition solution	.67
	3.6.2	Cell ass	embly and electrochemical sol-gel deposition	.67
	3.6.3	Structur	al characterisation	.67
		3.6.3.1	Scanning electron microscopy coupled with energy dispersive x-r	ray
			spectroscopy	.67
		3.6.3.2	Fourier transform infrared spectroscopy	.67
Cha	pter 4	1 Study	of the nanocellulose/graphite electrode system	68
4.1	Stru	uctural cl	naracterisation	.68
	4.1.1	Electrod	e microstructure investigation with scanning electron microscopy	y
		paired w	rith focused ion beam	.68
	4.1.2	Atomic f	orce microscopy	.70
4.2	e Eva	luation o	f mechanical flexibility	.71
4.3	Fun	damenta	al understanding of charge storage mechanisms	.73
	4.3.1	Effect of	nanocellulose content on the electrode charge storage	
		contribu	tions	.73
		4.3.1.1	Electrolyte stability limits	.74
		4.3.1.2	Nanocellulose/graphite electrode study using variable-rate CV	.74
		4.3.1	.2.1 Dunn analysis	.76
	4.3.2	Determi	nation of diffusion coefficients	.77
		4.3.2.1	Correlation to electrode morphology	.79
	4.3.3	Evaluati	on of electrode charge transfer resistance	.80
		4.3.3.1	Nyquist and Bode plots	.80
	4.3.4	Molecul	ar-level understanding of nanocellulose-ion interactions	.82
		4.3.4.1	Solid state NMR	.82
4.4	Cha	apter sun	nmary	.84
Cha	pter 5	5 Corre	lation of nanocellulose architecture to ion mass transport	t
		•••••		86
5.1	The	electros	pun nanocellulose/graphite electrode	.86

į	5.1.1	Electrode morphology	87
5.2	Inve	estigation of charge storage mechanisms	88
5.3	Eva	luation of diffusion coefficients	90
5.4	Eva	luation of charge transfer resistance	92
í	5.4.1	Nyquist and Bode plots	92
5.5	Cha	pter overview	94
Chap	oter 6	Nanocellulose in the Aluminium-graphite battery	95
6.1	Exa	mination of the role of nanocellulose in the charge transport and	
	inte	rcalation of chloroaluminate ions into graphite	95
(6.1.1	Current deconvolution	95
(6.1.2	Comparison of diffusion coefficients	99
6.2	Gal	vanostatic charge-discharge of aluminium-graphite/nanocellulose cel	ls
	••••		100
6.3	Flex	kible aluminium-graphite/nanocellulose pouch cell assessment	104
6.4	Elec	ctrochemical sol-gel deposition for the fabrication of covalently bonde	d
	elec	ctrode-electrolyte interfaces	105
6.5	Cha	pter summary	111
Chap	oter 7	Conclusions and Future Work	113
7.1	Con	nclusions	113
7.2		ure work	
		Optimisation and fulfilment of electrochemical sol-gel deposition of ionic	
•		liquid electrolyte	
-	7.2.2	In depth structural studies of graphite/NCF charged and discharged	
		electrodes	116
-	7.2.3	Modelling and machine learning	117
-	7.2.4	Monolithic integration with flexible electronic devices	117
lia* -		blications	140
		blications	
ADDE	naix	A Supporting solid state NMR data	119

liot o	of References	21
A.2	NMR Fitting parameters from DMFit1	20
A.1	Solid state NMR Li spectra of graphite/nanocellulose fibre electrodes 1	19

Table of Tables

Table 2-1 Summarized nanocellulose types, properties and TEM images. 35	
Table 2-2 Graphite electrode composites with different cellulose and derivative types, correlated to the electrode fabrication method, cellulose content, and specific discharge capacity at a given charge/discharge rate	oific
Table 2-3 Summary of Lewis acidity, molar ratio r (AlCl₃:EMImCl), and corresponding reaction	n.
Table 4-1 Calculated Ohmic resistance and conductivity values corresponding to different electrode bending angles	
Table 4-2 Charge transfer resistance value as calculated from the Nyquist plot in Figure 4. in correlation with wt.% NCF content, within composite graphite/NCF electrodes	11,
Table 6-1 Charge transfer resistance and Ohmic resistance values at the non-vent and bent states of the flexible Al-graphite/NCF pouch cell. 105	
Table 6-2 Comparative Silicon to Oxygen mass ratio	
Table 6-3 IR characteristic peak interpretation for a 60 wt.% NCF/graphite electrode that is pristine and after performing electrochemical sol-gel deposition110	

Figure 1.1 Nanocellulose polymer molecular structure [24]27	
Figure 1.2 Elect	rode design and operation hypothesis. In a composite graphite/nanocellulose
	electrode, ion mass transport is realised via the nanocellulose channel network
	with reduced diffusion limitations, while electron conduction occurs via the
	graphite particle pathway. The porous nanocellulose structure enables access
	of ions to the bulk of the graphite electrode30
Figure 2.1 Hiera	archical structure of cellulose, the polysaccharide biopolymer that is the main
	element of the plant cell wall. Cellulose fibres are composed of microfibril
	bundles, which are further made up of closely-packed cellulose molecular
	chains. Cellulose molecular chains are parallelly stacked due to the formation
	of hydrogens bonds between the surface hydroxyl groups, and the existence of
	van der Waals forces. Reproduced with permission from [52]. Copyright 2020
	by the authors. Licensee MDPI, Basel, Switzerland. Available under a CC-BY 4.0 $$
	licence33
Figure 2.2 Acid hydrolysis can be applied to NCFs to remove the amorphous regions and yield	
	rod-shaped NCCs. Reproduced from [55]. Copyright 2014 H. V. Lee et al.
	Available under a CC-BY 3.0 licence
Figure 2.3 Typic	cal electrospinning setup composed of a needle containing the polymer solution,
	a high voltage source and a grounded collector. Reproduced from [62].
	Copyright 2022 Thielke et al. Available under a CC BY 4.0 licence36
Figure 2.4 Illust	ration of nanocellulose integration strategies with active materials. Reproduced
	and adapted from [15] with permission from Elsevier. Image of NCF reproduced
	and adapted with permission from [81]. Copyright 2012, American Chemical
	Society. Image of NCC reproduced and adapted from [82] with permission from
	the Royal Society of Chemistry. Image of BNC reproduced and adapted with
	permission from [83]. Copyright 2007, American Chemical Society38
Figure 2.5 Comparative plot of nominal discharge potential vs. areal capacity for flexible and	
	stretchable batteries reported in comparison to commercial batteries.
	Reproduced (adapted) with permission from [1]. Copyright 2020 WILEY-VCH
	Verlag GmbH & Co. KGaA. Weinheim41

Figure 2.6 Sche	matic representation of the Li-ion battery operation principle. Li ⁺ intercalation
	into graphite takes place upon charging, while the reverse process occurs when
	it is discharged. Reproduced with permission from [104]. Copyright 2012
	Springer Science + Business Media, LLC
Figure 2.7 Li ⁺ int	tercalation and deintercalation into graphite happens with a staging
	mechanism, where the redox reaction does not proceed simultaneously in
	every graphite layer. An already increased interlayer spacing that results from
	already-intercalated ions that cause layer expansion, favour further
	intercalation on site, instead of intercalation in unoccupied layer. Reproduced
	from [110]. Copyright 2020 The Authors. Available under a CC-BY 4.0 licence.
	43
Figure 2.8 SEM	images of the MFC/graphite anodes at a) lower, b) higher magnification. An
	entangled, porous structure is seen, where MFC fibres are placed around
	graphite particles. Reproduced (adapted) from [38] with permission from the
	Royal Society of Chemistry46
Figure 2.9 a) Sir	ngle-paper battery configuration composed of an NCF/graphite/carbon black
	negative electrode, an NCF/LiFePO ₄ positive electrode, and an NCF/SiO ₂
	separator, demonstrating cell flexibility, b) SEM image of the unitized battery
	where three clear layers representing the components are distinguished.
	Reproduced from [44] with permission from the Royal Society of Chemistry.
	47
Figure 2.10 Bar	chart showing the abundance and theoretical gravimetric and volumetric
	capacities, for different elements that have been investigated in battery
	chemistries. Al metal exhibits a 8.23% abundancy in the Earth's crust, which is
	the highest compared to rest of the metals. Reproduced with permission from
	[39]. Copyright 2016 WILEY-VCH Verlag GmbH & Co. KGaA, Weinheim. 48
Figure 2.11 Ope	eration mechanism of the Al-graphite battery. During discharge, AlCl4 ⁻ anions de-
	intercalate from the graphite host at the cathode, while at the same time $AlCl_4$
	react with Al at the anode yielding $Al_2Cl_7^-$ (Al dissolution). The reverse process
	occurs upon charging, where Al is electrodeposited at the anode and $AlCl_4^{\scriptscriptstyle{-}}$
	anions undergo intercalation into the graphite cathode. Reproduced with
	permission from [41]. Copyright 2015, Springer Nature Limited50
Figure 2.12 Molecular structure of EMImCl used to synthesise chloroaluminate ionic liquids.	
	51

Figure 2.13 Illustration of capacitive, faradaic diffusion-limited and faradaic non-diffusion-	
	limited (pseudocapacitive) charge storage mechanisms. The flower-like shapes
	indicate solvated ions. Reproduced with permission from [169]. Copyright 2022
	Published by Elsevier Ltd54
Figure 3.1a) Ele	ectrode slurry composed of graphite and nanocellulose fibres, casted into a 8.5
	mm diameter polystyrene petri dish mould to dry, b) acquirement of the dried,
	free-standing and flexible electrode57
Figure 3.2 Focu	used ion beam coupled with scanning electron microscopy setup. Reproduced
	(adapted) with permission from [173]. Copyright 2011 Elsevier Ltd. Published by
	Elsevier Ltd. All rights reserved59
Figure 3.3 Sche	ematic of the three-electrode 3/8" PFA Swagelok electrochemical cell (half-cell),
	composed of a nanocellulose/graphite working electrode ($A = 0.28 \text{ cm}^2$), two
	glassy carbon rods ($A = 0.38 \text{ cm}^2$) as counter electrode and current collectors
	respectively and an Ag AgCl (sat. NaCl) reference electrode. The cell space
	was filled with 0.1M LiCl/ethanol electrolyte, and the working and counter
	electrodes are separated by two GF/D separators ($A = 0.38 \text{ cm}^2$), at a 3.5 mm
	distance61
Figure 3.4 Sche	ematic of the two-electrode 1/4" PTFE Swagelok electrochemical cell (full cell),
	composed of a nanocellulose/graphite positive electrode ($A = 0.28 \text{ cm}^2$), an Al
	negative electrode ($A = 0.28 \text{ cm}^2$) and two molybdenum rods ($A = 0.28 \text{ cm}^2$) as
	collectors. The cell space was filled with Lewis acidic (r = 1.5) EMImClAlCl ₃
	ionic liquid electrolyte and the electrodes are separated by a GF/D (A = 0.38
	cm²) separator62
Figure 3.5 Fabr	ication of flexible pouch aluminium-graphite cells based on
	nanocellulose/graphite and aluminium electrodes, and Lewis acidic ($r = 1.5$)
	EMImCl-AlCl ₃ electrolyte, in order to test conductivity retention65
Figure 3.6 Sche	ematic illustration of electrochemical sol-gel deposition. A sol precursor based
	on alkoxysilanes undergoes hydrolysis yielding silanol groups. The silanol
	groups then adsorb on the electrode surface and a condensation reaction
	takes place via cross-linking. The sol-gel process is triggered by water
	electrolysis which generates OH ⁻ and changes the pH only in close proximity to
	the electrode, leaving the rest of the bulk solution unaltered. Reproduced from
	with permission from [176]. Copyright 2015 Wiley-VCH Verlag GmbH & Co.
	VC 0 A

riguie 4. i ocai	ining electron microscopy images revealing unreferices in the surface
	morphology of the electrodes containing a) 40 wt.% NCF/G, b) 50 wt.% NCF/G,
	c) 60 wt.% NCF/G, d) 67 wt.% NCF/G, e) 70 wt.% NCF/G. Graphite particles and
	the NCF network are marked by a white label. f) Vertical cross section of 60
	wt.% NCF/G electrode showing a compact structure and good graphite-NCF
	particle interconnectivity69
Figure 4.2 Scar	nning electron microscopy images after Ga ⁺ focused ion beam treatment of the
	surface, revealing a horizontal cross-section and inner morphology of the 60
	wt.% NCF/G electrode, showing a) the difference between the non-treated,
	smooth electrode area versus the FIB-treated area where a porous structure is
	apparent, b) zoomed region in the FIB-treated area showing porous distribution
	ranging from ~12–70 nm
Figure 4.3 Aton	nic force microscopy images of a) graphite grain covered with the continuous
	NCF network where the green marked rectangular area represents the zoomed
	region depicted in b) showing NCF individual fibres that are organised into
	larger bundles. c) Three-dimensional image of the electrode surface 71
Figure 4.4 Dem	ionstrated flexibility of the 60 wt.% NCF/G electrodes under mechanical
1.60.0	deformation, specifically wrapped around a a) 2.5 cm diameter vial, b) a 1.1 cm
	diameter vial, c) twisted around a 0.7 cm diameter glass pipette without
	fracturing72
Figure 4.5 a) 60	wt.% NCF/G electrode bent at progressively increasing angles (140°, 180°, >
	180°). b) Electrochemical impedance spectra represented as Nyquist plot of
	the imaginary $(-ZIm)$ vs. real (ZRe) part of impedance corresponding to the 60
	wt.% NCF/G electrode non-bent state and to 140°, 180°, and >180° bending
	angles. The x-intercept ($R\Omega$) at the same frequency (~ 1.5 Hz) for all electrode
	bending states is used to calculate the electrode conductivity σ 72
Figure 4.6 CV c	urve of the electrolyte (0.1M LiCl/EtOH) background performed in a three-
	electrode cell with glassy carbon working and counter electrodes ($A = 0.38 \text{ cm}^2$)
	$vs.$ Ag AgCl, at a scan rate of 0.6 mV s ⁻¹ and T = 25°C. The figure shows the 3^{rd}
	cycle74
Figure 4.7 Varia	able-rate CV curves performed in a three-electrode cell vs. Ag AgCl, with an
	NCF/G working electrode ($A = 0.28 \text{ cm}^2$), a glassy carbon counter electrode ($A = 0.28 \text{ cm}^2$)
	0.38 cm 2), at scan rates varying from 0.8 mV s $^{-1}$ to 0.2 mV s $^{-1}$. CV curves are
	shown for NCE/G composite electrodes containing a) 40 wt % b) 50 wt % c) 60

	wt.%, d) 67 wt.% and e) 70 wt.% NCF. Each scan rate is shown for the 3 rd cycle.
	75
Figure 4.9 Door	anyalutad ayalia yaltammagrama narfarmad in a three alaatrada aall ya AglAgCl
rigure 4.6 Deci	onvoluted cyclic voltammograms performed in a three-electrode cell vs. Ag AgCl,
	with an NCF/G working electrode ($A = 0.28 \text{ cm}^2$) and glassy carbon counter
	electrode ($A = 0.38 \text{ cm}^2$) at 0.6 mV s ⁻¹ scan rate, demonstrating the relative
	faradaic diffusion-limited (light red area), and (pseudo)capacitive current
	contributions (blue area) for a) 40 wt.%, b) 50 wt.%, c) 60 wt.% and d) 67 wt.%
	NCF in composite NCF/G electrodes. (Pseudo)capacitive current is further
	deconvoluted to true capacitive and pseudocapacitive contributions, the
	respective percentages of which are also indicated. For each wt.% NCF
	content, the 3 rd cycle of the recorded voltammograms was used in this
	analysis77
Figure 4.9 Cath	nodic peak current (ipc) \emph{v} s. scan rate (\emph{v} $^{1/2}$) plots. Linear fitting applied for slope
	calculation and subsequently diffusion coefficient evaluation via the Randles-
	Ševčík equation. Analysis is performed for samples containing a) 40 wt.%, b) 50
	wt.%, c) 60 wt.%, and d) 67 wt.% NCF in composite NCF/G electrodes78
Figure 4.10 Diff	fusion coefficients and relative proportion of pseudocapacitive current
	contributions as function of wt.% NCF in NCF/G composite electrodes.79
Figure 4.11 Ele	ctrochemical impedance spectra shown as Nyquist plot of the imaginary $(-ZIm)$
	vs. real (ZRe) part of impedance. The high-frequency region (500 kHz to 40 Hz)
	of the spectra is depicted, for variable-NCF content electrodes. The electrodes
	were assessed in half-cells with glassy carbon counter electrode ($A = 0.38 \text{ cm}^2$)
	vs. Ag AgCl. Equivalent circuit representing the NCF/G electrode system (inset).
	81
Figure 4.12 Co	mparative Bode plots for the variable-NCF content NCF/G electrodes ($A = 0.28$
	cm ²), assessed in half-cells with a glassy carbon counter electrode ($A = 0.38$
	cm²) vs. Ag AgCl, showing a) the phase angle as a function of frequency, b)
	log Z as a function of frequency81
Figure 4.13 Sol	id state ¹ H spectra before (top) and after (bottom) intercalation within a 60 wt.%
	NCF/G electrode82
.	1 · · · · · · · · · · · · · · · · · · ·
rigure 4.14 Cro	oss polarisation ⁷ Li– ¹ H solid state NMR spectra, a) before and b) after
	intercalation within a 60 wt.% graphite/NCF electrode. The brown and teal
	signals represent the fitted data as relative signal integrals83

Figure 4.15 Sing	gle pulse solid state ⁷ Li NMR spectra, a) before and b) after intercalation for a 60
	wt.% NCF/G electrode. The brown and teal signals represent the fitted data, as $$
	relative signal integrals84
Figure 5.1 EL-N	CF/G composite electrode structure. Ion mass transport happens through the
	electrospun fibrous network, while electron transfer occurs in the interlayers of
	the graphite particles. The highly porous structure absorbs Li ⁺ from the organic
	electrolyte, transferring them to the redox active material (graphite) where ion
	intercalation takes place
Figure 5.2 Scan	ning electron microscopy images revealing the surface morphology of the 60
	wt.% EL-NCF/G electrode, where distinguished, high aspect-ratio electrospun
	cellulose nanofibrils are entangled and interconnected with graphite particles.
	88
Figure 5.3 Varia	ble-rate CV curves from experiments performed in a three-electrode cell
	assembled with glassy carbon counter electrode ($A = 0.38 \text{ cm}^2$) vs. Ag AgCl
	reference, at scan rates varying from 0.8 mV s ⁻¹ to 0.2 mV s ⁻¹ , for electrodes
	containing a) 50 wt.%, b) 60 wt.% and c) 67 wt.% EL-NCF in composite EL-
	NCF/G electrodes. Each scan rate is shown for the 3 rd cycle89
Figure 5.4 Deco	onvoluted cyclic voltammograms at 0.6 mV s ⁻¹ demonstrating the relative
	faradaic, true capacitive and pseudocapacitive current contributions for a) 50
	wt.% and b) 60 wt.% EL-NCF in composite EL-NCF/G electrodes. Each scan
	rate is shown for the 3 rd cycle90
Figure 5.5 Bar o	harts showing the relative current distributions at each scan rate for the a) 60
J	wt.% NCF/G and b) 60 wt.% EL-NCF/G electrode compositions90
Figure 5.6 Cath	odic peak current (ipc) v s. scan rate ($v^{\scriptscriptstyle 1/2}$) plots. Linear fitting was applied for
	slope calculation and subsequently diffusion coefficient evaluation via the
	Randles-Ševčík equation. Analysis is performed for samples containing a) 50
	wt.% and b) 60 wt.% EL-NCF in composite EL-NCF/G electrodes91
Figure 5.7 Diffu	sion coefficients and relative proportion of pseudocapacitive contributions
	$(\%Q_{\text{pseudo}})$ as a function of electrospun cellulose nanofiber content (wt.% EL-
	NCF) for EL-NCF/G composite electrodes92
Figure 5.8 Elect	rochemical impedance spectra shown as Nyquist plot of the imaginary ($-ZIm$)
	vs. real ($\it ZRe$) part of impedance. The frequency region of 500 kHz to 15 Hz is
	shown, for 60 wt.% NCF/G and 60 wt.% EL-NCF/G electrodes93

Figure 5.9 Com	parative Bode plots for the 60 wt.% EL-NCF/G and 60 wt.% NCF/G electrodes
	assessed in half-cells with glassy carbon counter electrode ($A = 0.38 \text{ cm}^2$) vs .
	Ag AgCl, showing a) phase angle as a function of frequency, b) $\log Z $ as a
	function of frequency93
Figure 6.1 Varia	able-rate CV curves performed in a two-electrode cell, with an NCF/G positive
	electrode ($A = 0.28 \text{ cm}^2$), and an Al metal negative electrode ($A = 0.28 \text{ cm}^2$), at
	scan rates varying from 1 mV s $^{-1}$ to 0.4 mV s $^{-1}$. CV curves are shown for NCF/G
	electrodes containing a) 50, b) 60, and c) 67 and e) 70 wt.% NCF. Each scan
	rate is shown for the 7 th cycle96
Figure 6.2 Deco	onvoluted cyclic voltammograms at 0.8 mV s ⁻¹ demonstrating the relative
	faradaic diffusion-limited (light red area), and (pseudo)capacitive current
	contributions (blue area) for a) 50, b) 60 and c) 67 wt.% NCF in composite
	NCF/G electrodes. (Pseudo)capacitive current is deconvoluted to true
	capacitive and pseudocapacitive contributions, as described by the respective
	percentages. Each scan rate is shown for the 7 th cycle
Figure 6.3 Rela	tive proportion of pseudocapacitive charge storage contributions ($\%Qpseudo$) as
	a function of NCF content (wt.% NCF) for NCF/G composite electrodes in Al-
	graphite cells99
Figure 6.4 a) C	V curve of 60 wt.% NCF/G showing the redox peak pair of the anodic P3A and
	cathodic P1C peaks of interest. b) Anodic peak P3A current (ipa) $vs.$ scan rate
	$(v^{\scriptscriptstyle 1/2})$ plot. c) Cathodic peak P1C current (ipc) vs. scan rate $(v^{\scriptscriptstyle 1/2})$ plot. d) CV
	curve of 67 wt.% NCF showing the redox peak pair of the anodic P3A and
	cathodic P1C peaks of interest. e) Anodic peak P3A current (<i>ipa</i>) vs. scan rate
	$(v^{\scriptscriptstyle 1/2})$ plot. f) Cathodic peak P1C current (ipc) vs. scan rate $(v^{\scriptscriptstyle 1/2})$ plot. Linear
	fitting was applied for slope calculation and subsequently diffusion coefficient
	evaluation via the Randles-Ševčík equation100
Figure 6.5 a) Ga	alvanostatic charge-discharge curves of an Al-graphite/67 wt.% NCF cell with
	Lewis acidic EMImCl-AlCl $_3$ electrolyte cycled at 5 mA g^{-1} to 100 mA g^{-1} to cut-off
	potential of 2.45 V. b) Coulombic efficiencies and specific discharge capacities
	of the Al-graphite/67 wt.% NCF cell at various cycling rates101
Figure 6.6 a) Ga	alvanostatic charge-discharge curves comparing the specific capacities of Al-
	graphite/NCF cells with 60 wt.% and 67 wt.% NCF in a Lewis acidic EMImCl-
	AlCl $_3$ electrolyte, cycled to a cut-off potential of 2.45 V at 100 mA g^{-1} , b) plots of

differential capacity (dQdV) against cell potential at 100 mA $\rm g^{-1}.~c)$

	graphite/NCF cells of the same cell at 60 mA g ⁻¹ and d) plots of differential
	capacity ($dQdV$) against cell potential at 60 mA g $^{ extstyle 1}$ 103
Figure 6.7 Elec	trochemical impedance spectra shown as Nyquist plot of the imaginary ($-ZIm$)
	$\emph{vs.}$ real (\emph{ZRe}) part of impedance. The frequency region of 500 kHz–10 mHz is
	shown, for a flexible Al-graphite/NCF pouch cell composed of a positive 60
	wt.% NCF/G electrode, a negative Al metal electrode, separated by a GF/D
	separator in a Lewis acidic chloroaluminate EMImCl-AlCl₃ ionic liquid. A flexible
	polypropylene pouch was implemented. Inset shows the impedance spectra at
	frequency region of 500 kHz–0.5 Hz104
Figure 6.8 Com	nparative Bode plots showing a) the phase angle as a function of frequency, b)
	$\it Z$ as a function of frequency, for a flexible Al-graphite/NCF pouch cell
	composed of a positive 60 wt.% NCF/G electrode, a negative Al metal
	electrode, separated by a GF/D separator in a Lewis acidic chloroaluminate
	EMImCl-AlCl₃ionic liquid105
Figure 6.9 a) C	hronoamperometry graph for electrochemical sol-gel deposition from a
	water/ethanol/TEOS/KCl/HCl solution, in a three-electrode cell using a 60 wt.%
	NCF/G working electrode ($A = 0.13 \text{ cm}^{-2}$), glassy carbon counter electrode ($A = 0.13 \text{ cm}^{-2}$)
	0.2 cm ⁻²), vs. Ag AgCl and for a deposition time of b) 10 min and c) 20 min.
	106
Figure 6.10 a) S	SEM image of the pristine 60 wt.% NCF/G. EDX images showing the distribution of
	b) carbon and c) oxygen atoms on the electrode surface107
Figure 6.11 a) S	SEM image of a 60 wt.% NCF/G electrode after 10 min electrochemical sol-gel
	deposition time. EDX images showing the distribution of b) carbon, c) oxygen
	and d) silicon atoms on the electrode surface108
Figure 6.12 a) S	SEM image of a 60 wt.% NCF/G electrode after 20 min electrochemical sol-gel
	deposition time. EDX images showing the distribution of b) carbon, c) oxygen
	and d) silicon atoms on the electrode surface108
Figure 6.13 a) S	SEM image of a zoomed region on a 60 wt.% NCF/G electrode after 20 min
	electrochemical sol-gel deposition time. EDX images showing the distribution
	of b) carbon, c) oxygen and d) silicon atoms on the electrode surface. 109
Figure 6.14 FT-	IR spectra for a 60 wt.% NCF/G electrode a) after performing electrochemical
	sol-gel deposition, b) at the pristine state111

Galvanostatic charge-discharge curves comparing the specific capacities of Al-

Research Thesis: Declaration of Authorship

Research Thesis: Declaration of Authorship

Print name: Evangelia Founta

Title of thesis: Nanocellulose-based Battery Electrodes

I declare that this thesis and the work presented in it are my own and has been generated by me as the result of my own original research.

I confirm that:

 This work was done wholly or mainly while in candidature for a research degree at this University;

2. Where any part of this thesis has previously been submitted for a degree or any other qualification at this University or any other institution, this has been clearly stated;

3. Where I have consulted the published work of others, this is always clearly attributed;

4. Where I have quoted from the work of others, the source is always given. With the exception of such quotations, this thesis is entirely my own work;

5. I have acknowledged all main sources of help;

6. Where the thesis is based on work done by myself jointly with others, I have made clear exactly what was done by others and what I have contributed myself;

7. Parts of this work have been published as:

E. Founta, M. Caravetta, M. Thielke, A. J. B. Sobrido, L. W. Gordon, T. Prodromakis, C. Ponce de León, D.G. Georgiadou and T. Schoetz, "Understanding Charge Storage Mechanisms in Flexible Nanocellulose/Graphite Battery Electrodes",
 ChemElectroChem (2025) doi: 10.1002/celc.202500096. Copyright 2025 The Author(s). ChemElectroChem published by Wiley-VCH GmbH. Available under a CC BY 4.0 licence.

Signature:	Date: 21 May	v 2025

Acknowledgements

"As you start to walk on the way, the way appears"; a quote from Rumi that has been catalytic to this 4-year journey. This journey which overall taught me that moving forward and finding direction, does not necessarily mean that you will always feel ready, or need to wait for the perfect circumstances. You just have to take each opportunity and make the first step, even small, towards your goal. My path might have not always been easy, but getting to walk through it supported by the right people, did definitely make the whole experience meaningful, and memorable.

Thus, I would like to start by thanking each and every one of my supervisors. Their trust, guidance and support have made me grow into the researcher that I always aspired to become. I would like to primarily thank Dr Dimitra Georgiadou for her mentorship inside and outside of the lab, and for always being there to support me through both PhD's and life's hardships. I am deeply appreciative for all the advice, the opportunities and the encouragement that I received from her side through all these years. I am also truly grateful towards Dr Theresa Schoetz for believing in me back in 2020, when I applied to work with her on next generation batteries. I will always cherish our meaningful conversations, and the memories I made during my research visits to her group both at the University of Illinois Urbana-Champaign and the City College of New York, which have been among the greatest highlights of my doctoral studies. I would also like to express my sincere gratitude towards Professor Carlos Ponce de León for always being available to provide his guidance, advice and help through my studies. I am truly glad that he joined this supervisory team and for always bringing his positive energy to our weekly meetings, creating a supportive environment. I would like to also extend my genuine appreciation towards Professor Themis Prodromakis for his guidance, his encouragement and support in joining the University of Southampton.

I was also fortunate enough to have met and collaborated with great researchers and academics along the way, who have profoundly contributed to the realisation of this work. I would like to thank Professor Ana Sobrido and Dr Michael Thielke from Queen Mary University of London for the provision of the electrospun cellulose nanofibers, Professor Marina Caravetta from the School of Chemistry and Chemical Engineering for helping me run and analyse crucial solid state NMR experiments, Dr Leo Gordon from the University of California - Santa Barbara and Associate Professor Robert Messinger from City College New York for providing their expertise on NMR interpretation, Dr Oleksandr Buchnev from the Optoelectronics Research Centre for the collaboration on conducting SEM/FIB measurements, and finally, Harini Srinkat from the University of Illinois Urbana-Champaign, for working together on the electrochemical

Acknowledgements

sol-gel deposition of ionic liquid electrolyte on nanocellulose/graphite electrodes, a niche technique which has been developed by Dr Theresa Schoetz's Electrochemistry Laboratory.

I would like to also express my deep appreciation towards the A.G. Leventis Foundation for funding my 3-year academic scholarship and enabling me to study in the UK.

Thank you to all the (extended) Flexible Nanoelectronics group members including Emilie, Oi Man, Chris, Mohit, Sujay, Yuxin, Roshni & Albert for the nice lunch breaks, picnics, dinners and conference trips that we spent together throughout all these years.

I would also like to thank all of my friends back in Greece, especially Giannis M. and Giannis D., for always making the time and circumstances to come visit. I am also extremely grateful to have crossed paths here with people that became invaluable friends – Vangelis, Ilias, Theo, Dimitra, Vasilis, Christos and Konstantinos, who filled this journey with light and colour.

A wholeheartedly thank you to my beloved family; without their continuous support all these years, I would definitely not be here today. To my father Kostas and my brother Vasilis for always supporting my education, my vision and for believing in me without any doubt. To my dear grandparents Vangelis and Vasiliki whose absence is felt deeply, but whose influence remains a light that never goes out within. To the rest of my family members including my aunts Rizoula & Magda, my uncles Kostas & Thomas, and my cousins Sakis, Konstantinos & Akis, that have always been there for me even from afar. Finally, and above all, I want to thank my partner Kostas for believing in me more than I do, for supporting me unconditionally, and for being my compass – always bringing me back to my path.

"Per aspera ad astra"

Seneca

Symbol	Meaning	Unit or value
Z	Absolute value of total impedance	Ohm
A	Electrode area	cm²
С	Molar concentration	mmol cm ⁻³
C_{DL}	Electrical double-layer capacitance	F
d	Diameter	mm or cm
D	Diffusion coefficient	cm² s ⁻¹
E	Electrode potential	V
ΔE^*	Potential window in which the current scales linearly with the scan rate	V
F	Faraday constant	96485 A s mol ⁻¹
f	Frequency	Hz
i	Current	mA
i_p	Peak current	mA
i_{pc}	Peak cathodic current	mA
j	Current density	mA cm ⁻¹
k_1	slope	Dimensionless
k_2	Intercept-x	Dimensionless
l	Distance between electrodes	cm
m	Mass	g

n	Number of electrons transferred	Dimensionless
Ø	Diameter	cm
рКа	Acid dissociation constant	Dimensionless
Q	Specific capacity of a cell	mAhg ⁻¹
$Q_{capacitive}$	Capacitive charge	mA h g ⁻¹
$Q_{faradaic}$	Faradaic charge	mAhg ⁻¹
Q_{pseudo}	Pseudocapacitive charge	mA h g ⁻¹
R	Universal gas constant	8.314 J K ⁻¹
r	Molar ratio of AlCl3:EMImCl	Dimensionless
R^2	Coefficient of determination for a mathematical fit	Dimensionless
R_{ct}	Charge transfer resistance	Ohm
$R_{\it \Omega}$	Ohmic resistance	Ohm
$R_{arOmega}$	Ohmic resistance Temperature	Ohm K or °C
T	Temperature	K or °C
T t	Temperature Time	Kor°C s
T t v	Temperature Time Scan rate	K or °C s mV s ⁻¹
t v wt.%	Temperature Time Scan rate Weight percentage	K or °C s mV s ⁻¹ Dimensionless

List of Abbreviations

EMImCl

Abbreviation	Meaning
AFM	Atomic force microscopy
Al/Al³+	Aluminium/Aluminium ion
Al ₂ Cl ₇ -	Heptachloroaluminate anion
AlCl₃	Aluminium chloride
AlCl ₄ -	Chloroaluminate anion
BNC	Bacterial nanocellulose
CA	Cellulose acetate
СВ	Carbon black
CE	Coulombic efficiency
CF	Carbon fibres
CH₂COO⁻	Carboxymethyl anion
CMC	Carboxymethyl cellulose
CNT	Carbon nanotubes
COCH₃	acetyl group
CV	Cyclic voltammetry
DEC	Diethyl carbonate
DFT	Density functional theory
DMAc	Dimethyl acetamide
DME	1,2-dimethoxyethane
DOL	1,3-dioxolane
DS	Degree of substitution
EC	Ethylene carbonate
EDX	Energy-dispersive x-ray
EIS	Electrochemical Impedance Spectroscopy
EMIm ⁺	1-Ethyl-3-methylimidazolium chloride cation

1-Ethyl-3-methylimidazolium chloride

FIB Focused ion beam

FT-IR Fourier-transform infrared spectroscopy

GF/D Glass fibre separator

IL Ionic liquid

Internet of Things

Li/Li⁺ Lithium/Lithium ion

Li-S Lithium-Sulphur battery

LSV Linear sweep voltammetry

MFC Microfibrillated cellulose

MW Molecular weight

NaBr Sodium Bromide

NaClO Sodium hypochlorite

NCC Nanocellulose crystals

NCF Nanocellulose fibres

NMP N-methyl-2-pyrrolidinone

NMR Nuclear magnetic resonance

OCP Open circuit potential

OH- Hydroxyl anion

PANI Polyaniline

PEDOT Poly(3,4-ethylenedioxythiophene)

PEO (Poly)ethylene oxide

PFA Perfluoroalkoxy

PP Polypropylene

PPy Polypyrrole

PTFE Polytetrafluoroethylene

PVDF Polyvinylidene fluoride

SBR Styrene-butadiene rubber

SEI Solid electrolyte interphase

SEM Scanning electron microscopy

SHE Standard hydrogen electrode

TEMPO 2,2,6,6-tetramethyl-1-piperidinyloxy

TEOS Tetraethyl orthosilicate

Chapter 1 Introduction

This Chapter contains adapted material from E. Founta et al., *ChemElectroChem* (2025), DOI 10.1002/celc.202500096. Available under a CC BY 4.0 licence.

1.1 The need for flexible and sustainable energy storage solutions

The modern energy storage landscape is being shaped by the demand for flexible batteries designed to power emerging electronics like wearables, medical, and Internet of Things (IoT) devices. [1-3] At the same time, there is an inarguable need to shift to the use of materials that adhere to the idea of a more circular economy, and abstain from depleting natural resources. [4, 5] Aside from high energy density, current requirements to power mechanically flexible devices involve the design of electrodes that are resilient under mechanical deformation, safe, as wearable and biomedical devices are in proximity to the human body, and finally cost-effective and easy to scale-up, ideally posing minimal environmental impact [5].

Currently, Li-ion batteries constitute the prevalent power source of consumer electronics, and their projected demand is forecasted, to grow by 600% in 2030. This is anticipated to yield a bottleneck in the availability of crucial battery elements, while at the same time concerns have been raised on their recyclability. [6, 7] Flexible Li-ion technologies have been already reported, however practical application is still limited as their performance, especially upon deformation, cannot compete with their conventional, rigid counterparts. The challenge here, is to manufacture inherently flexible battery components by engineering devices from a fundamental, material aspect. [1, 8] Graphite electrodes in particular, are used in different battery chemistries including Li-ion batteries [9-12]; however, their conventional configuration is inflexible and brittle making these unsuitable for use in wearables and flexible electronic devices [1, 2].

Consequently, both ecological and design-related constraints, underscore the urgency to reengineer modern graphite electrodes using a bottom-up approach from the material, up to the device scale [13]. In pursuit of a new generation of battery building blocks that encompass sustainability, abundancy and safety, bio-inspired materials have spurred extensive interest over the last decade [14]. Nanocellulose in particular, is a biopolymer that can be implemented in electrochemical storage systems in view of the element's profusion in nature, recyclability and exceptional mechanical properties [15, 16]. Here, nanocellulose is integrated with graphite to create inherently flexible and recyclable battery electrodes, which can be used in both Li-ion battery batteries and beyond. Specific applications including wearables would potentially

benefit more from the use of beyond-Li-ion technologies [1, 17] such as aluminum (Al)-graphite batteries, as they are safer and implement more environmentally profound materials. For example, disposable medical devices where risk minimization is of paramount importance, would ideally also generate a smaller ecological footprint if sustainable battery components are used. This work is in the direction of diversification of the battery market and utilization of tailored battery solutions in different flexible electronic applications. [18]

1.2 From cellulose to nanocellulose

By incorporating nanocellulose into state-of-the-art electrodes, such as graphite, batteries can be made inherently flexible. Cellulose in its bulk form is a polysaccharide $[(C_6H_{10}O_5)_n]$ natural polymer consisting of repeating β(1,4)-D glucose monomers (Figure 1.1) and it is the predominant constituent of plant cells, rendering it as the most environmentally-rich polymer occurring on Earth. This can be translated to profound material abundancy, non-toxic character, and low production cost. [19, 20] It is extracted primarily from biomass, but it can be also synthesized from certain bacterial strains. Cellulose can be further processed until acquiring nanoscale fibres (nanocellulose). Nanocellulose is defined as the type of cellulose where at least one of its dimensions (diameter) lies within the nanometre range (<100 nm). It is characterised by the existence of a fibrous, intertwined and porous network as well as surface hydroxyl (–OH) groups responsible for the intra- and inter- molecular polymer chain interactions. [21] The fibres offer a large surface area and form mechanically robust configurations owed to a high tensile strength of 100-130 GPa, depending on the nanocellulose type. [21] The surface –OH groups exhibit a wide range of pKa values, firstly due to the site variation along the polymer, and secondly due to the polyacid effect. Generally, the pKa value of glucose is around 12.5–13.5, and thus similar values are expected for unmodified cellulosic materials [22]. As an example, Saric et al. calculated a pKa value of 13.3, hypothesising the dissociation of one –OH group only per anhydroglucose unit [23].

Figure 1.1 Nanocellulose polymer molecular structure [24].

In plants, where it is the most abundant, nanocellulose is part of the water- and essential-minerals transport system. The surface –OH groups which are exposed on the surface, would be able to complex with ions near the fibre outer layer. As a result, nanochannels created between

the fibres can effectuate ion transport. [13, 25, 26] This nature-inspired ion transfer mechanism could also benefit energy storage systems, by promoting ion mass transport of electroactive ions in the bulk of the electrode. Intrinsically, the material does not conduct electrons and thus, it must be integrated with battery active materials that are electron conductors [27]. The surface –OH groups and hydrophobic polymer backbone can enable the interaction and combination with a plethora of active materials including graphite, via hydrogen bonding or van der Waals interactions [14, 28]. The material can undergo aqueous processing after surface modification, rendering the electrode fabrication process safe and inexpensive. Thinner and more lightweight electrode structures can be realised due to the nanocellulose large surface area (typically in the range of 200–300 m² g⁻¹), which simultaneously allows for improved access of ions to the electrochemically active component. [29] The role of nanocellulose in the potential benefit of mass transport phenomena in graphite-based electrodes, is not yet elucidated. Thus, fundamentally understanding the material's contributions and the underlying energy storage mechanisms is crucial in order to design electrode architectures with properties that can be controlled from the molecular, up to the macroscopic scale.

1.3 Li-ion and beyond: the future of energy storage

1.3.1 Improving Li-ion batteries

Graphite-based electrodes are widely used as the negative Li-ion battery electrode, due to the material's wide availability, high electron conductivity and ability to act as lithium ion intercalation host [11]. Conventional graphite-based electrodes are combined with a polyvinylidene fluoride (PVDF) binder, a rigid polymer that during fabrication is processed with highly toxic solvents like n-methyl-2-pyrrolidone (NMP).[30, 31] As a result, the graphite/PVDF electrode, suffers from lack of plasticity and recyclability, making the batteries unfit for specific application including the afore-mentioned flexible electronic devices. Unlike PVDF which is a major integrant of the electrode's dead mass, cellulosic materials have demonstrated the ability to serve as a flexible scaffold, and as a platform that can enhance capacity retention, rate capability and cycling stability.[3, 32, 33] Dead mass is defined as the proportion of the electrode materials which do not participate in active electrode phenomena and thus do not contribute to the overall charge storage. Despite the beneficial role of nanocellulose in electrodes where the dead mass is reduced [34-36], there is still lack of understanding of the fundamental role of this material in energy storage mechanisms, e.g. identifying and quantifying the effect of nanocellulose content and structure on ion transport phenomena, as well as molecular-level interactions of the ions with the nanocellulose surrounding environment. This would provide the link to the improved performance characteristics that have been reported,

like the achievement of a 180 mAh g^{-1} specific capacity for LiFePO₄ electrodes, which was 17.6% higher compared to the PVDF-based counterpart. In addition, longer cycling stability was shown for the cellulose-based binder with a 3.8% capacity loss after 200 cycles, compared to PVDF [37]. Another example concerns a graphite/microfibrillated cellulose (MFC) electrode which demonstrated a higher specific capacity (230 mAh g^{-1} at C/5) and capacity retention of 77% after 50 cycles, as compared to a values of 150 mAh g^{-1} capacity at C/5 and 54% retention for a graphite/PVDF anode in Li-ion cells [38].

1.3.2 Beyond Li-ion: The case of aluminium-graphite batteries

In pursuit of more sustainable and safer energy storage solutions, research has shifted to alternative battery chemistries beyond lithium, including aluminium-based systems. Aluminium (Al) has been identified as a material of choice as it is characterised by properties that align with modern field demands, like abundance in nature, low cost and safety during manufacturing and post-processing procedures. Al is stable under air, non-flammable and recyclable, which restricts the potential release of toxic substances into the landfill. Performance-wise, an Alnegative electrode has a theoretical specific capacity of 2980 mAh g⁻¹ which is competitive of the corresponding lithium value at 3860 mAh g⁻¹. [39, 40] Graphite-based electrodes have gained broad appeal as the positive electrode of choice in Al batteries, acting as an ion intercalation host material. The operation principle of the Al-graphite battery relies on the reversible intercalation and deintercalation of chloroaluminate anions into the layered graphite structure of the positive electrode, and electrodeposition of metallic Al at the Al negative electrode surface. [39, 41, 42] Thus far, the most investigated electrolytes for this system are chloroaluminate ionic liquids such as ethyl-3-methylimidazolium chloride-aluminium chloride (EMImCl-AlCl₃) [39]. Further advancements would include the optimisation of the conventionally-used, rigid and non-recyclable graphite/PVDF positive electrode, by replacing the fluoropolymer with a biopolymer with advanced properties like nanocellulose. This would enhance the battery's recyclable character, bending ability and ease of integration with flexible wearable devices, as well as ion transport properties.

In general, in terms of chemical stability of nanocellulose in solvents, the stability is highly dependent on the type of nanocellulose and its surface functional groups, on solvent polarity, pH and temperature. For instance, strong acidic and alkaline environments would cause hydrolysis and patrial degradation, respectively [43]. So far nanocellulose has been tested as an electrode binder in different battery electrolyte environments, e.g. in Li-ion batteries in EC/DEC [44], Li-S batteries in DME/DOL [45], aqueous Zn-ion batteries [46], Na-ion batteries in EC/DEC [47], thus exhibiting good versatility.

1.4 Electrode design and operation hypothesis

Free-standing and flexible graphite/nanocellulose fibre electrodes are prepared via a straightforward and non-toxic aqueous-processing route. The electrodes are composed of graphite particle integrated with a nanocellulose porous and fibrous network (Figure 1.2). Here, the nanocellulose fibres used, have a diameter ranging from 4–10nm, and a length of 1–3 µm, while graphite particles have an average diameter of <20 µm. Within the electrode structure, electrons are transferred at the graphite surfaces, while nanocellulose offers ion transport pathways, conveying ions from the organic electrolyte, to the bulk of the graphite electrode. Nanocellulose reduces mass transport limitations [34] and enables ion access even deep in the bulk of the graphite electrode. Hence, the charge storage contributions to the total current, in relation to nanocellulose content, are examined. Charge storage mechanisms are further discussed in Section 2.4.

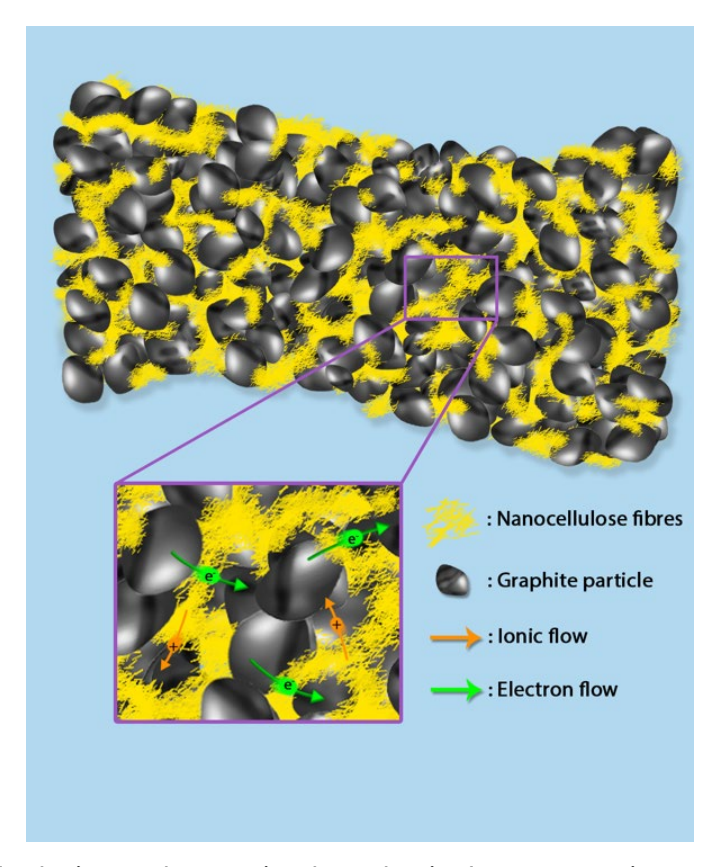


Figure 1.2 Electrode design and operation hypothesis. In a composite graphite/nanocellulose electrode, ion mass transport is realised via the nanocellulose channel network with reduced diffusion limitations, while electron conduction occurs via the graphite particle pathway. The porous nanocellulose structure enables access of ions to the bulk of the graphite electrode.

1.5 Aims and Objectives

The overarching aim of this thesis is the design and characterisation of inherently flexible nanocellulose/graphite electrodes, that are versatile for use in Li-ion and Al-ion rechargeable batteries. To that end, five main research objectives are identified. Each one of the objectives entails the implementation of materials, fabrication and electrochemical characterisation techniques to enable the realisation of the greater scope. As a result, each objective described below is a standalone research endeavour towards the realisation of the next-generation of batteries that require tailored, material-level, design, mechanical flexibility and safety.

Objective 1: Fabrication of flexible nanocellulose/graphite (NCF/G) electrodes with 180° bending ability.

Objective 2: Elucidation of charge storage mechanisms within nanocellulose/graphite electrodes in Li⁺ half-cells. Correlation of nanocellulose content and structure to ion mass transport through electrochemical techniques like variable-rate CV and EIS, and structural characterisation methods like SEM/FIB and AFM. Solid-state NMR is used to identify molecular interactions between Li⁺ and the surrounding nanocellulose environment.

Objective 3: Study of nanocellulose architecture impact on charge storage mechanisms, by implementing electrospun cellulose nanofibers (EL-NCF) with higher surface area.

Objective 4: Investigation of nanocellulose/graphite electrodes as cathodes in the Al-graphite battery. Charge storage mechanisms are studied via variable-rate CV. Specific capacity, coulombic efficiency and rate capability are evaluated via GVC.

Objective 5: Realisation of flexible Al-graphite/nanocellulose batteries. Bendable pouch cells are assembled and tested via EIS under flexion. Electrochemical sol-gel deposition of ionic liquid electrolytes is performed for the synthesis of a covalently-bonded electrode/electrolyte interface, for future all solid-state Al-graphite/nanocellulose batteries.

1.6 Novel contributions of this work

This thesis demonstrates the development and characterisation of mechanically flexible nanocellulose/graphite electrodes, and sheds light on the role of nanocellulose within both Liion and beyond Li-ion (particularly Al-graphite) battery chemistries. The fundamental understanding of the role of nanocellulose in composite nanocellulose/graphite electrodes, enables the conceptualization of flexible battery architectures, that pave the way towards greener and alternative electrochemical energy storage solutions. The main contributions of this thesis are:

- Demonstration of flexible nanocellulose/graphite electrodes with bending ability up to 180°, with ≈30% conductivity loss.
- Elucidation of charge storage mechanisms, showing reduction of diffusion-limitations by a total of 186% with increasing nanocellulose content within Li⁺ environment, and 18% within Al-graphite cells.
- Correlation of nanocellulose architecture to charge storage mechanisms, showing a 56% decrease in charge transfer resistance by increasing the nanocellulose fibre surface area, and minimisation of unwanted capacitive current.
- Revelation of Li⁺ molecular interactions within the nanocellulose/graphite electrode, exhibiting distribution in both graphite and nanocellulose environments with a <1nm proximity to nanocellulose surface functional groups.
- Integration and benchmarking of Al-graphite/nanocellulose batteries with a specific capacity of 64 mAh g⁻¹ at 5 mA g⁻¹ charge rate. Full battery bendability of pouch cells at a bending angle of 114° with a negligible 16% increase in Ohmic resistance compared to the flat state.
- Proof-of-concept of electrochemical sol-gel deposition from an alkoxy silane precursor and covalent bonding of an electrode/electrolyte intermediate layer for future fabrication of flexible graphite/nanocellulose/ionic liquid electrolyte interfaces.

Chapter 2 Literature review

This Chapter contains adapted material from E. Founta et al., *ChemElectroChem* (2025), DOI 10.1002/celc.202500096. Available under a CC BY 4.0 licence.

2.1 Cellulose and nanocellulose fundamentals

2.1.1 Classification and isolation methods

Cellulose is the most abundant polysaccharide natural polymer and has gathered research interest due to the low-cost, sustainability, biodegradable character and mechanical properties of the material. It is the predominant constituent of plant cells and is specifically located at the plant cell wall along with lignin and hemicellulose. Cellulose fibres are characterised by a hierarchical structure, made up of macrofibrils, which are in turn composed of microfibril bundles, made up of cellulose molecular chains, as seen in Figure 2.1. The molecular cellulose chains are described by the $[(C_6H_{10}O_5)_n]$ formula and consist of repeating $\beta(1,4)$ -D glucose monomers. Surface hydroxyl (–OH) groups enable the development of strong inter- and intramolecular hydrogen bonds, and in combination with van der Waals forces, the parallel stacking of cellulose chains is fostered, thus enabling the formation of larger fibrils. [48, 49] The abundant surface -OH groups offer a plethora of functionalisation options, for example the introduction of surface carboxyl groups to attribute ion exchange properties, for applications like water purification from toxic metals [50, 51].

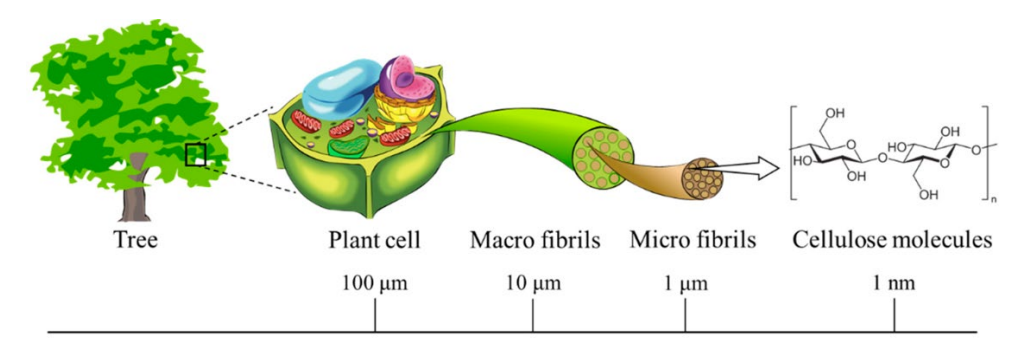


Figure 2.1 Hierarchical structure of cellulose, the polysaccharide biopolymer that is the main element of the plant cell wall. Cellulose fibres are composed of microfibril bundles, which are further made up of closely-packed cellulose molecular chains. Cellulose molecular chains are parallelly stacked due to the formation of hydrogens bonds between the surface hydroxyl groups, and the existence of van der Waals forces. Reproduced with permission from [52]. Copyright 2020 by the authors. Licensee MDPI, Basel, Switzerland. Available under a CC-BY 4.0 licence.

Cellulose can be processed until acquiring nanoscale fibrils. Nanocellulose is mainly extracted from trees, cotton, and biomass, however, bacterial synthesis and isolation from certain algae is also possible. In the first case, the procedure commences with bleaching of wood pulp [20], using acidified sodium chlorite and potassium hydroxide for the removal of lignin and hemicellulose, respectively [53]. Next, some commonly used nanofiber isolation mechanical techniques involve high pressure homogenization, mechanical grinding, ball milling, cryocrushing and microfluidisation, most of which are however high-energy demanding processes [15]. The resulting fibres consist of two coexisting regions, the crystalline where the molecular chains are densely packed, and amorphous where the chains are entangled and disordered [29].

Taking these properties into account, nanocellulose can be classified based on the overall structure and origin into nanocellulose fibres (NCF), nanocellulose crystals (NCC) and bacterial nanocellulose (BNC). The structure and crystallinity percentage can fluctuate depending on the source of nanocellulose and the isolation procedure that was followed. As mentioned above, NCFs can be isolated from plant sources, and the high aspect ratio fibres form entangled, porous networks. On the other hand, NCCs can be obtained after performing acid hydrolysis to remove the amorphous fibre regions and isolate the highly ordered ones (Figure 2.2). This results in the production of highly crystalline, distinct, rod-shaped cellulose nanoparticles, which are marked by shorter length and lower aspect ratio compared to NCFs. The length (L) to diameter (D) ratio (L/D) of NCC varies with values being reported from 11.8 to 67, depending on the cellulose source [54]. Both of the procedures aiming to the acquirement of NCFs and NCCs, are considered top-down fabrication approaches, starting from bulk cellulose and resulting in nanoscale particles. [48]

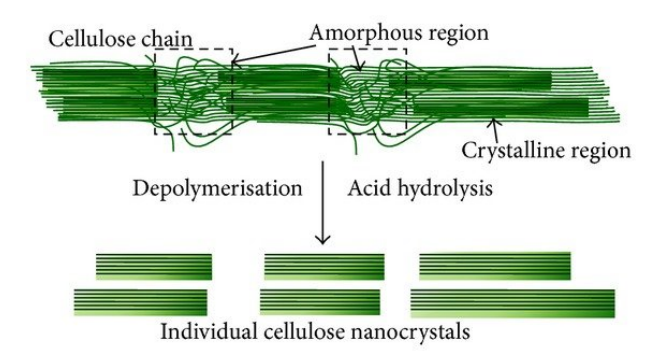


Figure 2.2 Acid hydrolysis can be applied to NCFs to remove the amorphous regions and yield rod-shaped NCCs. Reproduced from [55]. Copyright 2014 H. V. Lee et al. Available under a CC-BY 3.0 licence.

This is contrary to the synthesis of BNC which is the outcome of microbial synthesis (bottom-up fabrication approach). BNC is the secreted product of certain bacteria belonging to the genera *Acetobacter, Agrobacterium, Alcaligenes, Pseudomonas, Rhizobium, or Sarcina*. Cultivation of

Chapter 2

the bacteria in aqueous media, leads to the production of a thick gel called pellicle, which is made up of a 3D porous, web-like structure [56]. The structure of the nanofiber network of BC can be controlled by changing the type of bacterial strain, the additives in the culture medium, the type and conditions of cultivation, and the drying processes in the post-processing stage. The production happens in two steps: first β -1,4-glucan chains are synthesised, and second, BNC crystallisation takes place [57]. The material is characterised by high purity, crystallinity and web-like morphology. Nonetheless, upscaling is challenging due to the high cost of the process, and the smaller quantities that can be produced compared to NCF and NCC. The types and properties of the different nanocellulose types are summarised in Table 2-1.

Table 2-1 Summarized nanocellulose types, properties and TEM images.

Nanocellu	Source	Extraction	Dimensions	TEM image	Image
lose type		process	(l: length, d: width)		Reference
NCF	Plants,	Mechanical	l: several µm,		[58] ¹
	cotton, biomass,		5 nm < d < 100 nm		
	algae		Network-shaping		
			fibres		
NCC	Plants,	Acid	100 nm < l < 250 nm,		[59]²
	cotton, biomass,	hydrolysis	5 nm < d < 70nm		
	tunicate		Rod-shaped particles		
BNC	Gram	Bacterial	1 < l < 9 um		[60] ³
	negative bacteria	synthesis	20 nm < d < 50 nm		
	Dacteria		Web-like networks		

¹ Reproduced with permission from [58]. Copyright 2011 Elsevier Ltd. Published by Elsevier Ltd. All rights reserved.

² Reproduced with permission from [59]. Copyright 2019 Elsevier Inc. All rights reserved.

³ Reproduced from [60]. Copyright 2022 The Authors. Available under a CC BY NC ND licence.

2.1.1.1 Other methods for nanofibril synthesis

For the isolation of NCFs, aside from the mechanical methods described in Section 2.1.1, alternative methods can be also implemented including electrospinning, solution blow spinning, hybrid dry-jet wet spinning and dry spinning [61].

2.1.1.1.1 Electrospinning

Electrospinning is a versatile technique that is used to obtain nanofibers [21]. A polymer solution is pumped via a needle with constant flow, and a high potential is applied to the solution so that the polymer droplet at the tip of a needle is charged. When the surface tension is overcome, a Taylor cone is formed and then a jet flows from the blunt needle towards a grounded electrospun fibre collector. Finally, solvent evaporation takes place and the mat is received. A typical electrospinning setup can be seen in Figure 2.3. Care should be taken upon choosing the solvent, as highly volatility could possibly block the needle due to rapid evaporation, whereas a low volatility one promotes fibre entanglement and film formation on the collector [62, 63].

This method offers the opportunity to modify the material architecture, as fibres in the nano/micro scale can be acquired, while at the same time, the porosity and overall structure of the resulting film can be controlled. For instance, the final morphology can be affected by fine-tuning experimental variables like solution composition, collector types etc [64].

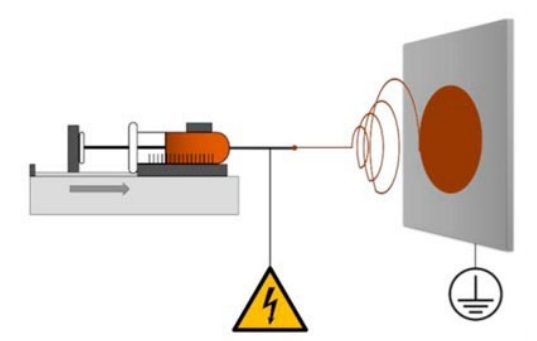


Figure 2.3 Typical electrospinning setup composed of a needle containing the polymer solution, a high voltage source and a grounded collector. Reproduced from [62]. Copyright 2022 Thielke et al. Available under a CC BY 4.0 licence.

2.1.2 Surface modification techniques

The availability of surface functional –OH groups on the nanocellulose surface, renders the polymer as an ideal candidate for surface modification to tailor the material properties, and render it compatible with specific applications. In particular, there are three –OH groups in total, one of which is primary alcoholic, while the rest are secondary alcoholic. A plethora of

functionalisation techniques can be applied, among of which are carboxymethylation, esterification and TEMPO oxidation. [64]

TEMPO (2,2,6,6-tetramethylpiperidine-1-oxyl) oxidation is one of the most commonly applied functionalisation techniques, where the primary alcoholic –OH groups are converted to carboxylate groups, attributing a strong negative surface charge to nanocellulose [65]. This leads to increased hydrophilic character and water dispersibility. In general, untreated cellulosic materials are in insoluble and not easily dispersible in water. As an example, solvents that can disperse cellulosic materials are DMSO and DMF [66], while certain molten salts and ionic liquids including 1-butyl-3-methylimidazolium chloride, 1-allyl-3-methylimidazolium chloride and 1-ethyl-3-methylimidazolium acetate, have been proven effective to dissolve cellulose. [67] The method can be used in combination with mechanical nanocellulose isolation methods, as it leads to efficient microfibril detachment, which can be considered a pretreatment step. Then, mechanical methods like homogenisation become less energy consuming upon producing the final nanofibrils [53]. Typically, TEMPO is used along with NaBr and NaOCl, which is why often the procedure is thought to be non-ecofriendly and costly.

Carboxymethylation is one of the most common modification methods, that is used to enable aqueous solubility of the material [68]. The resulting polymer is usually referred to as carboxymethyl cellulose in literature (CMC). The procedure is organised in two steps: alkalinization and etherisation. In the resulting structure, surface –OH groups are partially substituted by carboxymethyl groups ($-CH_2-COO^-$), and depending on the number of the functional groups that were replaced, CMC is characterised by different degree of substitution (DS). The DS in general, is one of the most important parameters that affects the CMC behaviour in terms of solubility, stability and interaction with other materials [30, 37, 69, 70].

Finally, esterification with acetic acid is a widely implemented nanocellulose functionalisation technique, where cellulose acetate can be synthesised. Cellulose acetate is a cellulosic derivative where the –OH groups are partially or completely replaced by acetyl (–COCH₃) groups. It is insoluble in water and is used in order to improve the compatibility towards hydrophobic materials [71]. It is used as a precursor in the electrospinning polymer solution for nanocellulose fibre acquirement, because unmodified cellulose is soluble in a limited number of solvents, that are not suitable candidates for electrospinning. As a result, cellulosic derivatives like cellulose acetate have been tested, and the prevalent solvent system yielding the most uniform fibres, is acetone/DMAc [72].

2.1.3 Integration strategies

Surface nanocellulose functional groups, enable the integration of nanocellulose with conductive materials, as nanocellulose is inherently non electron conductive. Among others, conducting polymers, metallic particles and carbon-based materials can be combined with nanocellulose to yield composites with combined properties that can be used in a wide variety of applications, including energy storage. In general, two main integration strategies can be followed, as seen in Figure 2.4 [15]. The first approach suggests the deposition of an active material coating as a thin layer on a nanocellulose substrate, using methods like sputtering, vapor deposition and others, vacuum filtration, doctor blade coating, spray gun and screen printing.

The second route involves mixing of the components, where covalent and non-covalent interactions allow for the fabrication of composites. For example, blending nanocellulose with active materials like graphite [73, 74], CNTs [75], graphene [76] can be facilitated via the production of homogeneous dispersions and subsequent solvent removal like vacuum filtration, drop casting and others. This method is preferred for carbon-based materials, including graphite. Another approach is the *in situ* polymerization, where conductive polymers like PANI [77] and PPy [78] can be integrated with nanocellulose. *In-situ* polymerization can be either chemical and initiate by the addition of an oxidant like FeCl₃, or electrochemical, by the application of potential. The latter, offers better control on experimental parameters like final polymer thickness, deposition speed and time [79, 80].

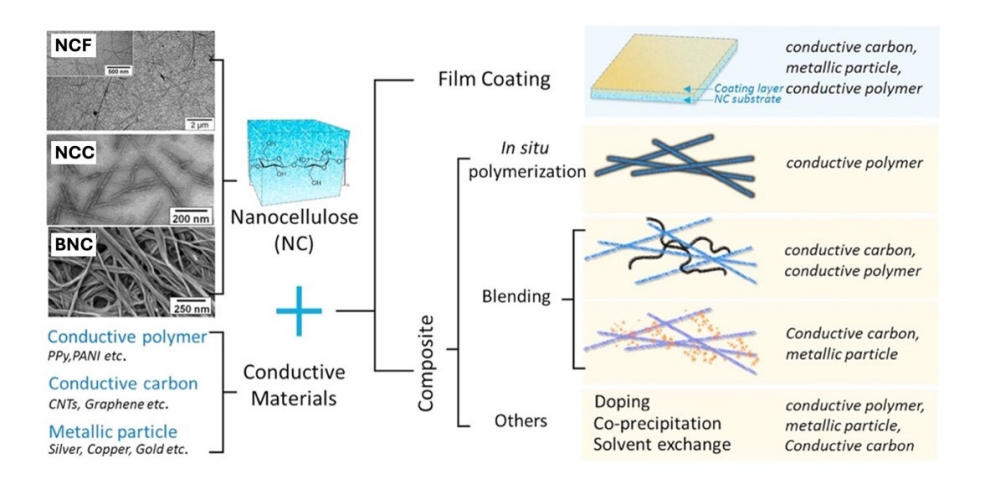


Figure 2.4 Illustration of nanocellulose integration strategies with active materials. Reproduced and adapted from [15] with permission from Elsevier. Image of NCF reproduced and adapted with permission from [81]. Copyright 2012, American Chemical Society. Image of NCC reproduced and adapted from [82] with permission from the Royal

Society of Chemistry. Image of BNC reproduced and adapted with permission from [83]. Copyright 2007, American Chemical Society.

2.1.4 Why is nanocellulose considered for energy storage applications?

Current demands within the field of energy storage, include tailoring of the battery architecture and shape to fit flexible electronics requirements, sustainability of battery components to tackle electronic waste pollution, while maintaining high performance. Nanocellulose properties like abundancy, sustainable character, thermal stability and mechanical flexibility, have rendered the material as an ideal candidate for state-of-the-art batteries. As a natural and abundant material that comes from biomass, nanocellulose is a biodegradable, recyclable, non-toxic, biocompatible and inexpensive material that can replace conventional fluoropolymer binders. The latter are widely used due to their stability against degradation in battery environments, however, their environmental impact, toxic processing with NMP and lack of flexibility have pushed research towards pursuing alternative solutions.

The material high aspect ratio and porosity allows for the fabrication of lightweight electrodes with high active material mass loadings. Also, the high porosity of the nanofibrous network, promotes improved electrode/electrolyte contact and electrolyte ion absorption. Drawing inspiration from nature where cellulose channels contribute to the transport of essential nutrients within plants [25, 84], it has been shown from previous studies that nanocellulose has exhibited ion transport and subsequent performance improvement characteristics [34, 85-88]. However, the exact molecular-level phenomena and actual nanocellulose contributions to mass transport are yet to be deciphered. This also explains why nanocellulose would be preferred over bulk cellulose in this case, as the larger surface area of nanofibrils allows for shorter ion diffusion pathways.

The inter- and intramolecular hydrogen bonds between molecular cellulose chains, give rise to mechanically stable and flexible electrodes, where stress upon deformation can be alleviated. Specifically, NCF have a Young's modulus of 138 GPa, and 2-3 GPa strength. Thus, free-standing, flexible battery electrodes can be fabricated, where current collectors are omitted. This helps reduce the content of inactive electrode compartments. Furthermore, the existence of surface functional groups enables the functionalisation and integration with a great variety of active materials, and incorporation in diversified battery chemistries. [27, 56]

2.2 State of the art in cellulose and nanocellulose-based flexible batteries

2.2.1 Considerations

Current demands for flexible batteries are affected by the rapid evolvement of flexible and wearable electronics. Battery architectures should be adaptable and able to adopt various shapes, by alleviating mechanical stress. As a result, the design of modern batteries should include key-aspects like mechanical flexibility, high energy density, advanced safety and long-term durability. One of the most important aspects, is to be also able to retain performance upon deformation. [89-91]

To elaborate further, mechanical flexibility is of paramount importance for such battery technologies, so that they can be configurable and adaptable. Different substrates like textiles [92, 93], nonwoven mats [94], modified nylon fabric [95] and carbon cloth [96] have been explored to render battery electrodes flexible. Energy density is another critical aspect for batteries which enables their practical applicability. Several strategies can be followed for improvement, including the reduction of the percentage of inactive battery components [97], and increase of active materials weight fraction. The latter can be realised by manufacturing thicker electrodes using porous materials, which would allow for 3D access of ions to the active material [65]. Safety and durability are also crucial, especially for close-skin electronics applications. In this case liquid electrolytes would pose a higher risk, as compared to solid-state or quasi-solid-state electrolytes, where the possibility of leakage is minimal [98, 99]. Furthermore, the use of alternative battery chemistries like Al- and Zn-based batteries , would perhaps be more beneficial compared to Li-ion batteries [100]. As a result, broadening of the battery market by exploring different battery technologies that can be tailored to the application of choice, would be valuable.

The competition between flexible batteries and conventional structures at the moment is high, and where flexible batteries currently lag, is the lack of flexibility concerning each one of the battery components [1]. Figure 2.5 illustrates a comparative plot of reported flexible systems, and the capacity and nominal discharge potential achieved, in comparison to the commercial counterparts.

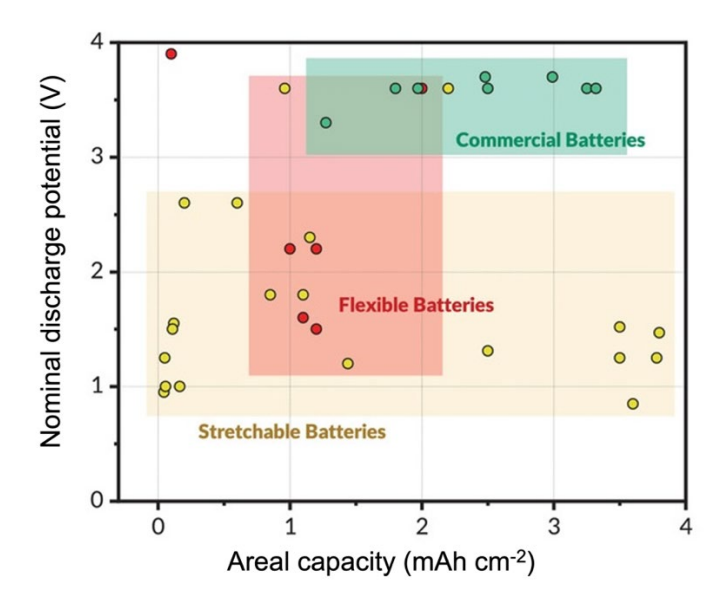


Figure 2.5 Comparative plot of nominal discharge potential *vs.* areal capacity for flexible and stretchable batteries reported in comparison to commercial batteries. Reproduced (adapted) with permission from [1]. Copyright 2020 WILEY-VCH Verlag GmbH & Co. KGaA, Weinheim.

From this perspective, battery components including electrodes, electrolytes, separators and casings should be engineered to be deformable. A good starting point would be the incorporation of inherently flexible materials, like nanocellulose. Within the context of sustainability, the incorporation of nanocellulose-based batteries for specific electronics applications where there is a high rate of disposal, for example glucose sensors, smart bandages and smart sensors for patient monitoring in hospitals, would be beneficial due to the recyclable and biodegradable character of the material [101, 102].

2.2.2 Nanocellulose in Lithium-ion batteries

2.2.2.1 Basic operation of a Lithium-ion cell

Rechargeable Li-ion batteries were first commercialized by Sony in the early 1990s, and the technology has since been dominating the area of portable and consumer electronic devices, due to the high energy density (>180 W h kg $^{-1}$) and cycling life, which attributes a longevity of 2–3 years [103]. A typical cell consists of a metal oxide (e.g. LiCoO $_2$) positive electrode on an Al current collector, a graphite negative electrode on a Cu current collector, an organic electrolyte which is usually based on a mixture of carbonate solvents like EC and DEC, and a polyolefin separator usually made of PP. The operation principle can be summarized by the intercalation of Li $^+$ into the graphite host lattice and creation of a graphite intermediate complex Li $_x$ C $_6$ upon charging, while upon discharging Li $^+$ undergo deintercalation from graphite. The structure of the battery and operation are illustrated in Figure 2.6.

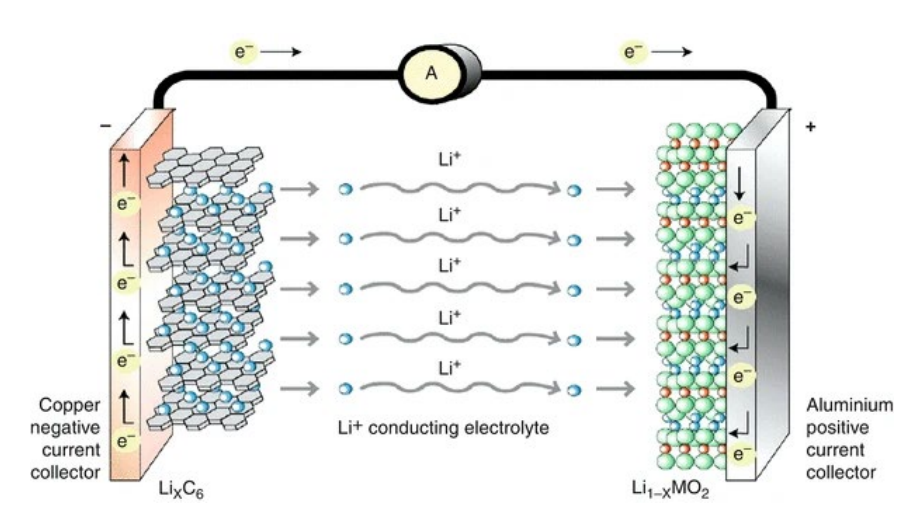


Figure 2.6 Schematic representation of the Li-ion battery operation principle. Li⁺ intercalation into graphite takes place upon charging, while the reverse process occurs when it is discharged. Reproduced with permission from [104]. Copyright 2012 Springer Science + Business Media, LLC.

The negative electrode half-cell reaction is described by Equation 2-1:

Charge (intercalation)
$$xLi^{+} + xe^{-} + 6C \implies Li_{x}C_{6}$$
 Discharge (deintercalation) (2-1)

For the fabrication of the graphite electrode, a polymeric polyvinylidene fluoride (PVDF) binder is used to coat the electrode slurry on the Cu current collector. PVDF is a rigid fluoropolymer that during fabrication is unavoidably processed with toxic and expensive solvents like NMP [105]. The graphite/PVDF electrode in organic carbonate electrolyte systems, often suffers from lagging kinetics [30] and is not suitable for integration in flexible batteries, as it cannot undergo mechanical deformation [106].

2.2.2.2 Graphite electrodes

Graphite remains the primary anode material for Li-ion batteries, due to properties like high electronic conductivity, low cost and long cycle life. It has a theoretical specific capacity of 372 mA h g⁻¹ [31], and is characterised by a layered structure, where sp² hybridized graphene layers are stacked and stabilised by relatively weak Van der Waals forces, and π – π interactions. This layered structure attributed the flake-like morphology of graphite particles, where two regions coexist: the basal and the edge planes.

In general, two graphite types with different morphology are encountered, natural and synthetic, which are both used in Li-ion batteries. Natural graphite can be found in nature, whereas synthetic graphite is a petroleum derivative that is lab-made and hence, is more expensive. However, it is more pure, thermally stable and, from a certain point of view, sustainable, as the

production is independent from natural graphite availability. However, more edge planes exist in natural graphite, which are general more reactive than the basal planes, and promote improved accessibility for Li⁺ to be intercalated.

Li⁺ intercalation and deintercalation redox reaction [107] can take place into the graphite host materials due to the existence of the weak Van der Waals forces, which allow for layer expansion and increase of the interlayer distances, which are originally evaluated at 3.35 Å. A staging mechanism has been revealed during this process (Figure 2.7), as intercalation of the guest ions does not proceed concurrently at every graphite layer. This happens as already-expanded interlayers from previous ion intercalation thermodynamically promote further intercalation of new ions on site, rather than intercalation to an empty layer. [11, 108].

As previously mentioned, conventional graphite electrodes are bound by PVDF polymer binders, making them rigid, non-environmentally friendly, and expensive. Previous studies have established the superior performance of electrodes based on cellulose and cellulose derivatives over their PVDF-based counterparts in battery electrodes [3, 33]. Unlike PVDF which is a major integrant of the electrode's dead mass, cellulose materials have demonstrated the ability to serve as a flexible scaffold, and as an electrode component that can enhance capacity retention, rate capability and cycling stability [32, 109]. Moreover, electrode fabrication is safe, straightforward, with no need to control environmental humidity levels as it proceeds with the use of water, which also contributes to faster drying steps compared to NMP [31].

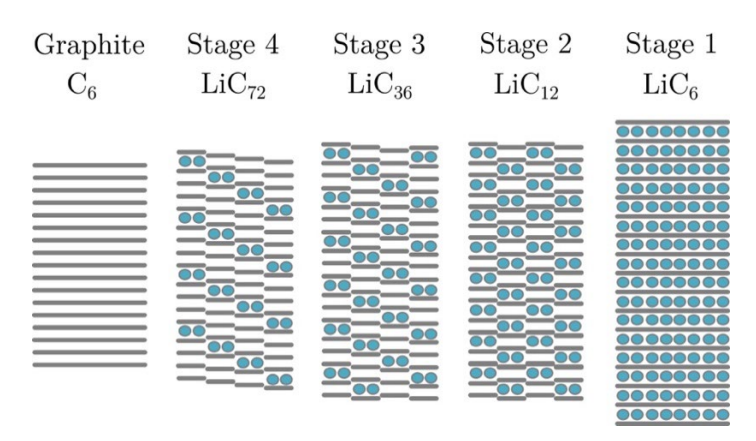


Figure 2.7 Li⁺ intercalation and deintercalation into graphite happens with a staging mechanism, where the redox reaction does not proceed simultaneously in every graphite layer. An already increased interlayer spacing that results from already-intercalated ions that cause layer expansion, favour further intercalation on site, instead of intercalation in unoccupied layer. Reproduced from [110]. Copyright 2020 The Authors. Available under a CC-BY 4.0 licence.

Nanocellulose has the ability to act as a dispersing agent and exfoliant for graphite in aqueous suspensions [14, 111, 112], as the hydrophobic nanocellulose backbone adsorbs onto the

hydrophobic graphite particle, and the charged hydrophilic surface help stabilise the structure in water [113]. For example, CMC is one of the most frequent graphite dispersants as it has excellent aqueous solubility, due to the partial substitution of surface –OH groups with –CH₂COO groups. Certain parameters as CMC molecular weight [68] and DS [70] have shown to affect the stability of the graphite/CMC slurries and subsequently, the electrode performance. Higher molecular weight CMC promotes more effective adsorption onto the graphite surface and thus better contact between the materials, leading to improved performance characteristics. Furthermore, it has been underlined that lower DS of CMC can contribute to dispersion stability, and longer battery life cycle, due to enhanced hydrophobicity interactions and stronger particle interaction [70, 114]. Apart from surfactant properties, when a maximum CMC content is reached, the non-adsorbed CMC behaves as a thickening or gelling medium yielding in the slurries [28]. Moreover, the surface functional groups of nanocellulose offer electrolyte wettability and retention of organic solvents [105]. This can contribute to more efficient Li* transport [86, 115], as it has been shown that -OH groups can complex with Li* [26].

Electrode thickness and porosity also affects ion transport properties and subsequently, performance. Thicker electrodes with higher graphite mass loadings would theoretically improve the energy density of the cell, however, the longer length for Li⁺ transport and increase in tortuosity, can hinder access to graphite [116]. The relationship between porosity and electrochemical performance is also complex, as it requires fine tuning. Both excessive as well as few pores can lead to insufficient performance [117]. For instance, extremely high porosity of a 70% value was shown to limit the electrochemical performance of screen-printed graphite/NCF-CMC electrodes as the contact area between materials is significantly reduced [118].

Calendering is a standard strategy that is employed to increase electrode density, and has shown to reduce porosity from 70% to 34%, achieving an enhancement in specific capacity, from 93 to 315 mAh g⁻¹. Instead of calendering, kneading has been also used for graphite/CMC electrode densification, improving the contact between particles and uniformity in pore distribution [119]. As a result, electrode kinetics were improved. Within the same context for kinetics enhancement, Li-substituted CMC and NCF have been used in graphite thick electrodes, as they was proven to offer additional Li⁺ conduction pathways [29, 37, 120]. For example, Li-CMC/graphite electrode, exhibited a 14% increased capacity compared to Na-CMC/graphite, which is possibly owed to the increase of freely moving Li⁺ across Li-CMC, and enhanced interfacial conduction [121, 122]. As a result, ion conductivity is a key design factor that should be considered for the improvement of graphite-based electrodes.

NCF chemical properties can be tailored by surface functionalising of –OH groups, and specific compatibility with other battery components can be achieved. Surface modified NCF with TEMPO-periodate was used to fabricate graphite electrodes which were tested against CMC/SBR-graphite electrodes. In terms of electrochemical performance, a 10% increased specific capacity was noted for the TEMPO-modified NCF fibres at faster charge rates, as compared to the second. Françon *et al.* attributed this to better chemical affinity between the battery components, as well as to the presence of an enduring NCF network that can constrict graphite volume expansion during charge/discharge. Mechanical lap shear tests indeed confirmed that TEMPO-modified NCF electrodes showed higher durability both dry and wetted by the battery electrolyte. The electrodes however, remained deposited in a Cu current collector that would potentially limit their application in cases where a degree of deformation is needed [123].

Current collectors can be eliminated to attribute higher electrode flexibility and decease the electrode dead mass. For example, Si and graphite were mixed and supported by a CMC binder without the use of metal current collectors [124]. Acetylene back (AB) conductive additive was incorporated in the slurry which was finally freeze-dried to yield a 3D conductive sponge structure. The thin AB layers work as a current collector. Higher specific capacities than normal graphite electrodes were recorded due to Si presence (theoretical specific capacity 4200 mAhg⁻¹ [125]).

Jabbour et al., have carried-out extensive work on flexible (nano)cellulose/graphite electrodes. They were one of the first groups to explore the fabrication of free-standing micro fibrillated cellulose/graphite electrodes via an aqueous processing route where the electrode slurry was cast in a Teflon mould, and the electrodes collected presented comparable performance in Liion cells as their traditional PVDF-based counterparts. The electrode morphology is shown in Figure 2.8. [38]. Later on, they adopted a papermaking fabrication approach, where they implemented highly refined cellulose fibres (FB) to prepare of composite FB/graphite and FB/LiFePO₄/carbon black free-standing, paper electrodes [126]. All paper-based cells made by filtration were also reported by the same group where Li-ion cells were composed of a paper graphite anode and cathode, and common paper hand-sheets were used as separators. Filtration is a straightforward and rapid route that could be potentially up scaled. The recorded specific capacity of 350 mAh g⁻¹ and cycling performance were comparable with PVDF-bound graphite anodes [127]. Finally, they used the same filtration approach to manufacture graphite/carbon fibre (CF) paper electrodes, which present excellent mechanical properties [128].

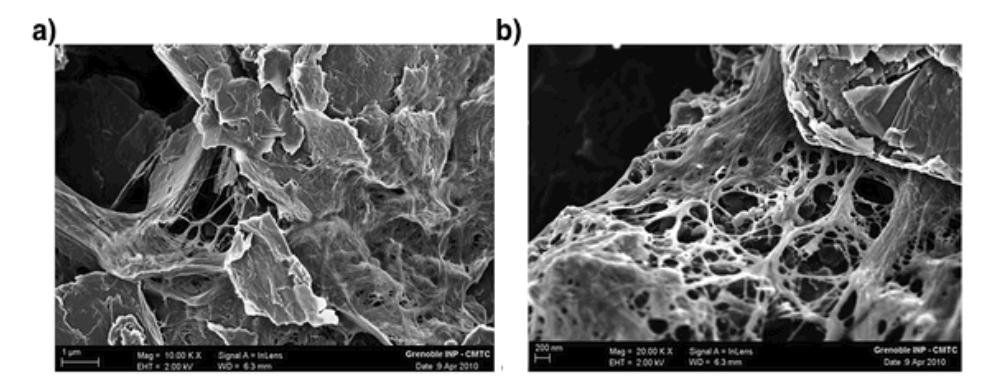


Figure 2.8 SEM images of the MFC/graphite anodes at a) lower, b) higher magnification. An entangled, porous structure is seen, where MFC fibres are placed around graphite particles. Reproduced (adapted) from [38] with permission from the Royal Society of Chemistry.

A fabrication method for all-paper-based Li-ion cells that is cost-effective and with a low environmental impact, was proposed by Zolin *et al.* [129] and refers to spray coating. An MFC/Graphite/carbon black (CB) electrode aqueous slurry was spray coated onto a wet paper substrate, and the resulting current collector-free electrodes were characterised by very good mechanical flexibility. This approach could be up-scaled to allow the manufacturing of large-surface electrodes.

Another full-paper Li-ion cell was described by Jeong et al. [16] using graphite and carbon-coated LiFePO₄ as anode and cathode electrode materials, respectively. However, instead of water processing of cellulose fibres, an ionic liquid EMIMAc solvent was used to prepare the slurries. After coating, the ionic liquid is removed by phase inversion, using water. Pure cellulose fibres are highly insoluble in most conventional solvents, but ionic liquids seem to be a class of solvents that can successfully dissolve cellulose [130].

An important milestone in this field was accomplished by Leijonmarck *et al.* [44], who proposed a full paper battery that has however a unified architecture. NCF was used as an electrode binder for both the anode (NCF, graphite, carbon black) and the cathode (NCF, LiFePO₄, carbon black), and as a separator (NCF, SiO₂). NCF-based separators in general, demonstrate superior characteristics compared to the traditional polyolefin ones, in terms of electrolyte permeability, and porosity tuning [131]. The electrode and separator dispersions were filtered successively, acquiring a cake-like result, and the as-received battery was approximatively 250 µm thick (Figure 2.9). The cell exhibited good reversibility and cycling stability, however a capacity decay was noted which was probably owed to water side reactions, and subsequent lithium loss.

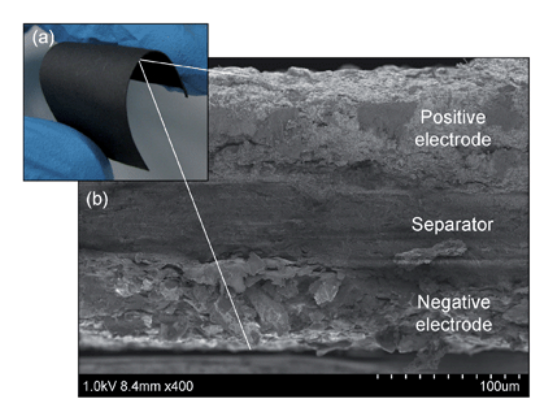


Figure 2.9 a) Single-paper battery configuration composed of an NCF/graphite/carbon black negative electrode, an NCF/LiFePO₄ positive electrode, and an NCF/SiO₂ separator, demonstrating cell flexibility, b) SEM image of the unitized battery where three clear layers representing the components are distinguished. Reproduced from [44] with permission from the Royal Society of Chemistry.

Such unitised structures, promote improved interfacial contact among battery components, shortened charge transport distances, and better overall flexibility of the battery. A summary of work conducted on graphite and cellulose/nanocellulose battery electrodes, is listed in Table 2-2.

Table 2-2 Graphite electrode composites with different cellulose and derivative types, correlated to the electrode fabrication method, cellulose content, and specific discharge capacity at a given charge/discharge rate.

Electrode composition	Fabrication method	Cellulose content (wt.%)	Specific capacity (mAh g ⁻¹)	Charge/ Discharge rate	Ref.
Graphite/CMC	Coat on Cu foil	2	360	C/10	[132]
Graphite/CMC-MFC	Screen printing	3	315	C/10	[118]
Graphite/Li-CMC/SBR	Coat on Cu foil	1	317	C/20	[121]
Graphite/TEMPO-periodate NCF	Coat on Cu foil	5	315	1C	[123]
Graphite-nano-Si/AB/CMC	ball milling & freeze-dry	5	940	1C	[124]
Graphite/MFC	Cast in Teflon mould	10	300	C/10	[38]
Graphite/CMC+FB	Filtration	11	350	C/10	[127]
Graphite/CF/CMC+FB	Filtration	20	225	0.08C	[128]
Graphite/CB/MFC+CMC	Spray coating	8.7	350	C/10	[129]
Graphite/Cellulose fibres	Coat on Cu foil	2	370	C/10	[16]
Graphite/CB/NCF (in unitized cell)	Filtration	10	146 (wrt. LiFePO ₄₎	C/10	[44]

2.3 Aluminium-graphite rechargeable batteries

Despite the popularity of Li-ion batteries during the last two decades, concerns have been raised on the future availability of crucial battery materials including Li and Co. Discussions on the safety of the cells with regard to thermal runway, flammability, and toxicity, have brought these issues at the forefront. Considering those points, the battery research field has broadened the investigation on other chemistries, including Na, Zn, Li-S, K, Al among others (Figure 2.10). Certain cases would be a better fit than Li-ion batteries in specific applications, like wearables for instance, where safety and non-toxicity are crucial. From these chemistries, Al rechargeable batteries specifically offer many advantages like Al abundancy and low-cost. Al is the third most supple element within the planet's crust at 8.23% [133] and the most abundant among metals. It has properties like good recyclability, and competitive theoretical specific capacity of 2980 mAh g⁻¹ [134] against 3860 mAh g⁻¹ for Li [135]. The volumetric capacity for Al (8040 mAh cm⁻³) is four times greater than Li [108]. Furthermore, Al is not air-sensitive and flammable. As a result, processing and manufacturing can be carried out in ambient conditions.

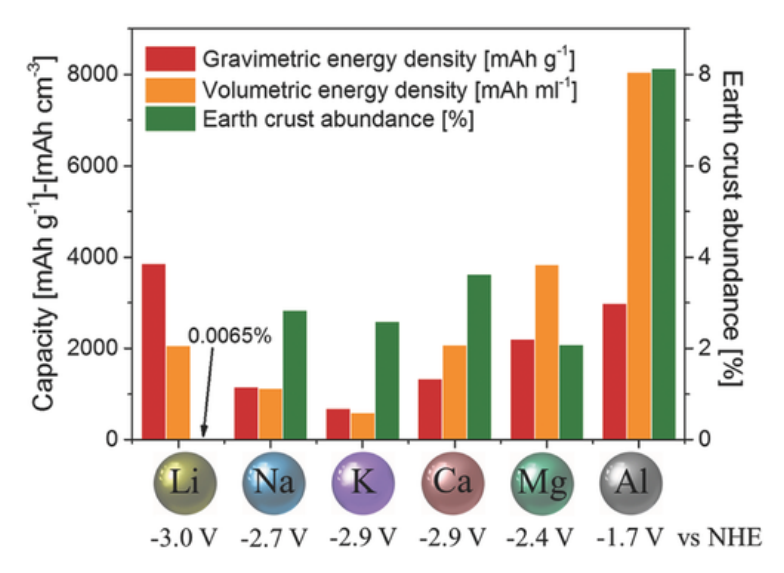


Figure 2.10 Bar chart showing the abundance and theoretical gravimetric and volumetric capacities, for different elements that have been investigated in battery chemistries.

Al metal exhibits a 8.23% abundancy in the Earth's crust, which is the highest compared to rest of the metals. Reproduced with permission from [39]. Copyright 2016 WILEY-VCH Verlag GmbH & Co. KGaA, Weinheim.

2.3.1 Operation mechanism

A typical Al rechargeable battery is based on an Al metal anode, where Al undergoes reversible electrodeposition upon charge and discharge [136]. The cathode can be based on various materials that accommodate charge storage of Al-based ionic species via various mechanisms, like intercalation, insertion and conversion. Among these, materials like conductive polymers

[137], Mo₆S₈ [138], quinones [139], vanadium oxides [140], sulphides [141], chalcogenides and others [142] have been investigated. Graphite and derivatives have been also explored as cathode materials, due to the low-cost, high conductivity and layered structure that can host ions upon chagrining and discharging [42, 143].

Contrary to Li-ion batteries where the graphite electrode is used as the anode, here the graphite electrode is used as the cathode. This happens as graphite is redox amphoteric and can form both donor- and acceptor-type intermediate compounds. In the first case where graphite acts as a donor, it can host species like alkali metal cations as Li^+ for example, whereas acceptor-type compounds are formed with halogen-based, e.g. PF_6^- , $AlCl_4^-$ and oxide intercalant species. Donor-type compounds are best fit for anode electrodes, while acceptor-type ones are best suited for cathode electrodes. Structurally, graphite intercalation occurs in stages as well, where filling an already occupied interlayer is prioritised over filling an empty one. [107, 108, 144]

One of the widely investigated and successful systems is the Al-graphite battery in non-aqueous ionic liquid electrolytes, like 1-ethyl-3-methylimidazolium chloride aluminium chloride (EMImCl-AlCl₃), which was introduced by Lin *et al.* [41] The charge storage mechanism of this system is based on the intercalation and de-intercalation of AlCl₄⁻ anions into the graphite cathode and the simultaneous reversible electrodeposition and dissolution of aluminium metal on the anode upon charge and discharge. During these processes, Al₂Cl₇⁻ and AlCl₄⁻ coming from the electrolyte, both participate in the electrochemical reactions (Figure 2.11). The reactions that describe the system operation, are shown below. [145]

Anode:
$$4Al_2Cl_7^- + 3e^- \rightleftharpoons Al + 7AlCl_4^- \tag{2-2}$$
 discharge

charge

Cathode:
$$C_n + AlCl_4^- \rightleftharpoons C_n[AlCl_4] + e^-$$
 (2-3) discharge

charge

Overall:
$$3C_n + 4Al_2Cl_7^- \rightleftharpoons 3C_n[AlCl_4] + Al + 4AlCl_4^-$$
 discharge (2-4)

The Al $^{3+}$ /Al electroplating redox reaction occurs at -0.7 V vs. SHE (0 V vs. Al $^{3+}$ /Al) [146], while in such systems, graphite is shown to oxidise at 1.5 - 2.1 V (vs. Al $^{3+}$ /Al) [143]. Structurally, most studies have shown than AlCl $_4$ adopts a tetrahedral geometry [147] upon

intercalation/deintercalation, although there are few reports suggest planar quadrangle [148] configuration. Graphene layer expansion occurs in order to accommodate the large size of the chloroaluminate anion (5.28 Å compared to 0.72 Å for Li⁺) [39].

Capacity values reported for this system range from 60–150 mAh g⁻¹[149, 150], which are in general lower than systems where Al³⁺ is intercalated, instead of AlCl₄⁻. Al³⁺ can only occur in aqueous electrolytes. Despite the higher capacity values, aqueous-based systems, suffer from issues like the formation of an oxide layer on the Al electrode surface, which lower significantly the efficiency of the cell [108]. Also, Al³⁺ is characterised by high charge density, and thus potent interactions are developed both with the graphite host leading to ion trapping and higher overpotentials, as well as with other cell species, where the overall ion diffusion is then slowed down [134]. These parameters, including water side reactions [40], have significantly limited the practical application of aqueous based Al systems.

Ionic liquids on the other hand, have high conductivity, almost comparable to aqueous electrolytes, are non-flammable, non-volatile and have wide electrochemical stability windows [39, 151].



Figure 2.11 Operation mechanism of the Al-graphite battery. During discharge, AlCl₄ anions deintercalate from the graphite host at the cathode, while at the same time AlCl₄ react with Al at the anode yielding Al₂Cl₇ (Al dissolution). The reverse process occurs upon charging, where Al is electrodeposited at the anode and AlCl₄ anions undergo intercalation into the graphite cathode. Reproduced with permission from [41]. Copyright 2015, Springer Nature Limited.

By definition, ionic liquids are organic salt compounds with an R $^+$ X $^-$ formula where R $^+$ = organic cation and X $^-$ = halide anion. The compounds are in liquid state at T < 100 $^{\circ}$ C. The most widely implemented ionic liquids are however the ones made up of an organic salt of an alkyl imidazolium chloride, like 1-ethyl-3-methylimidazolium chloride, EMIm $^+$ Cl $^-$ (Figure 2.12) and 1-butyl-3-methylimadazolium chloride, BMIm $^+$ Cl $^-$, paired with aluminium chloride AlCl $_3$. These are preferred for Al electrodeposition with high coulombic efficiency. [152, 153]

Figure 2.12 Molecular structure of EMImCl used to synthesise chloroaluminate ionic liquids.

For an EMImCl-AlCl₃ ionic liquid, only when the composition is Lewis acidic can the electrodeposition of Al metal take place, as in neutral and basic compositions the ionic liquid electrolyte decomposes before electrodeposition can takes place. There have been cases of Al can be deposited from neutral, but with low coulombic efficiency. Lewis acidity is achieved where the molar ratio r of AlCl₃ to EMImCl, is 1 < r < 2. In Lewis acidic media, both AlCl₄ and Al₂Cl₇ are present. Basic ionic liquids where r < 1, AlCl₄ and Cl anions coexist. Finally in the Lewis neutral case where r = 1, mainly contain AlCl₄, however due to autosolvolysis, some lower amounts of Al₂Cl₇ and Cl still exist. The Lewis acidity definition of ionic liquids and the corresponding reactions are summarised in Table 2-3. [154]

Table 2-3 Summary of Lewis acidity, molar ratio r (AlCl₃:EMImCl), and corresponding reaction.

Category	Molar ratio, r	Reaction		
Lewis acidic	1 < r < 2	$pR^+Cl^- + qAlCl_3 \rightarrow (q-p)Al_2Cl_7^- + (2p-q)AlCl_4^-$		
Lewis basic	r<1	$pR^+Cl^- + qAlCl_3 \rightarrow pR^+ + qAlCl_4^- + (p-q)Cl^-$		
Neutral	r = 1	$R^+Cl^- + AlCl_3 \rightarrow R^+ + AlCl_4^-$		
		$2AlCl_4^- \rightleftharpoons Al_2Cl_7^- + Cl^-$		

^{*}p and q refer to molar amount of R^+ and $AlCl_3$.

It should be noted however, that ionic liquid electrolytes are moisture-sensitive and exothermically react to form hydrochloric acid [145]. Thus, care should be taken and work related to ionic liquids should be current out in controlled conditions like a glovebox. Aside from aqueous and ionic liquid electrolytes, other cases like organic solutions, inorganic molten salts, deep eutectic solvents, polymer, water-in-salt and MOF-based electrolytes have been investigated through the years [155, 156]. For example, it was shown that quasi-solid polymer electrolytes based on EMImCl-AlCl₃, PEO and fumed silica showed better electrochemical stability than the ionic liquid counterpart, when charging up and extended upper cut-off potential of 2.8 V in Al-graphite battery cells [150].

Graphite [143, 157-159] and its derivatives like graphitic foam [149, 160] and graphene [161, 162] in Al-batteries, have been studied and covered in literature. Apparently, the common denominator is the fast-charging capabilities that are linked to various parameters. First, to the absence of an SEI layer on the graphite electrode surface which would introduce important diffusion limitations [157]. Secondly, to the weak ion-solvent complexation in the ionic liquid electrolyte, enabling rapid solvation and desolvation of ionic species [144]. Thirdly, due to the larger size of AlCl₄ anions compared to Li⁺ cations, a larger by 163% interlayer expansion occurs to the graphite structure, which helps AlCl₄ diffuse much faster compared to Li⁺ [163]. Finally, fast solid-state diffusion of ions has been correlated with graphitic structure [157], where exfoliated graphite for example showed significantly lower diffusion limitations for AlCl₄ intercalation, and improved capacity retention at faster discharge rates as compared to non-exfoliated graphite, which could be explained due to lower tortuosity in the case of exfoliated graphite [164].

2.3.2 Challenges and remaining progress

Progress in Al-graphite batteries should be advanced towards flexible structures, to get incorporated in applications where mechanical deformation is essential. Little work has been carried out in the field, in terms of flexible electrode engineering. For example, carbon nanofibers were used to yield free-standing cathodes, that achieved a specific capacity of 126 mAh g⁻¹ at 1 A g⁻¹, and long term cycling stability for 20,000 cycles [101].

Nanocellulose as an inherently flexible polymer, could substantially improve graphite-based cathodes for Al-ion batteries. So far, the use of nanocellulose in this system is at a very primary stage. Specifically, Chen *et al.* [36], reported the manufacturing of graphite cathodes using a CMC binder instead of PVDF, with the first showing better structural stability over time. This also contributed to a high specific capacity of 120 mAh g⁻¹, close to graphite theoretical value. On

the other hand, cellulose biomass was used as a graphitisation precursor for the development of more sustainable graphite cathodes [165].

Al-graphite batteries are also capable of fast charging, which has been linked to rapid ion diffusion among others. It has been highlighted that the introduction of porosity [166] and tortuosity [164] parameters as well as their fine-tuning, plays a key role in enhancing this phenomenon. For that reason, materials like nanocellulose could not also contribute as flexible substrates, but also work as mass transport pathways. To our knowledge, nanocellulose has not been studied in terms of charge storage mechanisms within the Al-graphite battery, which is thus further discussed in Chapter 6.

2.4 Charge storage mechanisms in electrochemical systems

2.4.1 Categories

Fundamental understanding of charge storage mechanisms in electrochemical systems, would contribute to targeted engineering of electrodes and subsequently battery cells that can be tailored to the desired applications. In general, charge storage mechanisms can be primarily categorised based on the underlying cause and process that charge is stored. Also, the two mechanisms differ on the effect of ion mass transport on their rates. Electric capacitors which are an example of capacitive charge storage, store charge due to physical charge separation at the interface. This charge compensation happens for instance within a dielectric material which undergoes polarization. Hence, capacitive charge storage is based on the electrostatic accumulation of charges at the electrode interface, without the involvement of electron transfer reactions. Faradaic charge storage on the other hand, is based on the occurrence of a redox reaction and subsequent electron transfer across the electrode/electrolyte interface. A battery is fundamentally based on redox reactions and is as a result, faradaic-dominated. For the redox reaction to occur, ion mass transport to interface has to be facilitated, and can be faradaic diffusion-limited or faradaic non-diffusion-limited (pseudocapacitive). Mass transport can happen via diffusion, migration and convection. Diffusion is the spontaneous molecular movement of ions due to the existence of a concentration gradient ∇C , that happens with a rate r_{diff} . A ∇C can exist within the electrolyte near the electrode/electrolyte interface, within the electrolyte confined in a porous electrode, and in the solid structure of the electrode. Migration is owed to the movement of ions upon application of an external electric field $\nabla \varphi$. Convection is the result of ion movement due to forced movement of the solution, e.g. upon stirring. For simplification reasons, convection is negligible and omitted, since no electrolyte stirring exists in rechargeable Li-ion and Al-ion batteries. Migration transport is smaller in comparison to

diffusion, and can be neglected upon the addition of an excess supporting electrolyte that does not take part in the reactions at the electrode, or in the case of high-conductivity electrolytes where the electric field in the electrolyte bulk is small. [167-169]

The two types of faradaic charge storage can be distinguished by the relationship between the rate of diffusion r_{diff} and the rate of the redox reaction r_{rxn} . For this reason, the electrochemical Damköhler number (Da_{el}) has been introduced and defined as the ratio of r_{rxn} to r_{diff} . For a faradaic diffusion-limited system, the rate of diffusion is less than the electrochemical reaction rate, and $Da_{el} >> 1$. Contrary, for a faradaic non-diffusion-limited (pseudocapacitive) system, the rate of diffusion is less than the rate of the electrochemical reaction, and $Da_{el} << 1$. Essentially, a pseudocapacitive charge storage happens when mass transport of the electroactive component to the surface of the electrode, is faster than the rate of the electrochemical redox reaction. Many systems, however, practically work under mixed regimes ($Da_{el} \sim 1$) where both phenomena affect the total current density, j. The phenomena are illustrated and summarised in Figure 2.13. [169]

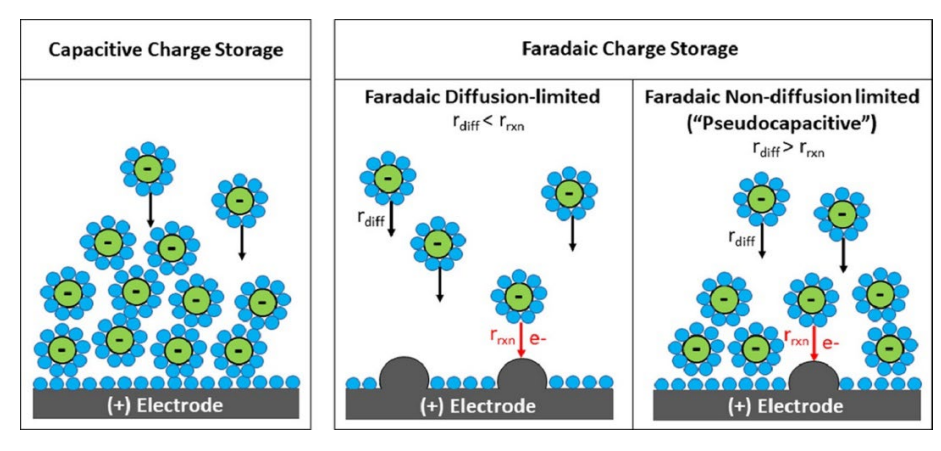


Figure 2.13 Illustration of capacitive, faradaic diffusion-limited and faradaic non-diffusion-limited (pseudocapacitive) charge storage mechanisms. The flower-like shapes indicate solvated ions. Reproduced with permission from [169]. Copyright 2022 Published by Elsevier Ltd.

An initial qualitative perspective on the nature of charge storage mechanisms occurring within an electrochemical system can be provided by the shape of cyclic voltammograms (CVs) and galvanostatic charge/discharge curves (GVCs). In the first case, typical CVs of capacitors exhibit a rectangular shape, where the absence of peaks declare the non-existence of redox reactions. Faradaic diffusion-limited current manifests by the appearance of redox peaks. Pseudocapacitive CVs usually exhibit an intermediate shape, with an almost rectangular shape where less intense redox peaks also appear. In GVCs, capacitive and certain pseudocapacitive charge storage characteristics exhibit triangular-shaped curves, while faradaic charge storage demonstrates characteristic plateaus that are linked to the potentials where redox reactions

occur. Mixed regimes can appear as sloping GVCs. In chloroaluminate graphite intercalation in Al-ion batteries for example, charge storage is proven to happen with significant pseudocapacitive characteristics. Li⁺ graphite intercalation on the other hand is dominated by a faradaic, diffusion-limited charge storage mechanism [170], however there are reports of pseudocapacitive intercalation of Li⁺ into graphite upon engineering of graphite to increase carbon defects [171].

2.4.2 Current deconvolution and quantifying

Aside from qualitative estimation, charge storage mechanisms can be quantified via various methods. One of these, is the "Dunn method", where the total current can be deconvoluted to the relative contributions of each charge storage mechanism. This can be achieved by acquiring CV or LSV curves at various scan rates v, usually ranging from 1–10 mV s⁻¹. The total current is the sum of both faradaic diffusion-limited and (pseudo)capacitive non-diffusion-limited proportions, as described by Equation (2-5):

$$I(v) = k_1 v + k_2 v^{0.5} (2-5)$$

This is based on the fact that faradaic diffusion-limited current scales with the square root of the scan rate, whereas the (pseudo)capacitive non-diffusion-limited current scales linearly with the scan rate. By plotting $i/v^{0.5}$ versus $v^{0.5}$, a curve is acquired and by applying a linear fit, the slope k_1 and intercept k_2 can be calculated, and consequently the relative current proportions at a specific potential. It should be noted that each current/potential point in the CV curve is characterised by a separate k_1 and k_2 values. As a result, by performing the analysis at several potential points will eventually yield the cumulative contributions to the total current. [139, 156, 172]

As the (pseudo)capacitive non-diffusion-limited current part needs to be further deconvoluted, as it encompasses both pseudocapacitive and true capacitive charge storage contributions, with the latter originating from the electrical double layer charging, characterised by a double-layer capacitance C_{DL} . Thus, for the calculation of C_{DL} which is constant in the system, a potential window ΔE^* is chosen on the CV of interest. Within that window no faradaic reactions should occur and as a result, the current would be proportional to the scan rate. For C_{DL} calculation, the double layer capacity ΔQ_{DL}^* at this potential window is calculated first, by integrating the current over time (Equation 2-6). [169]

$$C_{DL} = \frac{\Delta Q_{DL}^*}{\Delta E^*} = I \frac{\Delta t}{\Delta E^*}$$
 (2-6)

Chapter 2

Then, the double layer capacity ΔQ_{DL} over the whole scan (anodic, cathodic, or total) can be determined by Equation (2-7):

$$\Delta Q_{DL} = C_{DL} \Delta E \tag{2-7}$$

Finally, the pseudocapacitive charge can be estimated by Equation (2-8):

$$Q_{capacitive} = Q_{pseudo} + Q_{DL} (2-8)$$

Chapter 3 Experimental Methods

This Chapter contains adapted material from E. Founta et al., *ChemElectroChem* (2025), DOI 10.1002/celc.202500096. Available under a CC BY 4.0 licence.

3.1 Electrode fabrication

3.1.1 Preparation of nanocellulose/graphite electrodes (NCF/G)

Nanocellulose fibres that are partially carboxymethylated (Nanografi) were dispersed in deionised water at a content of 2 wt.%, by immersion in an ultrasonic bath (RS PRO, 200W). Nanocellulose surface has both hydroxyl and carboxyl groups, with a carboxyl content of 2.5 mmol g⁻¹, as determined from the vendor. Graphite powder (Sigma Aldrich, powder, <20 µm, synthetic) was then slowly incorporated in the dispersion by using a high shear mixer (Silverson, L4RT) at 4000 rpm for 1h. The graphite loading was maintained at 3.52 mg cm⁻² while the nanocellulose (NCF) content varied from 40 to 50, 60, 67 and 70 wt.%, yielding five electrode compositions. The NCF content percentages correspond to electrode compositions with graphite-to-nanocellulose weight ratio of 1.5:1, 1:1, 1:1.5, 1:2 and 1:3, respectively. The asobtained mixture was then heated at 80°C and underwent stirring at 1200 rpm for 1 h using a hotplate stirrer (Stuart, UC152), until a thick slurry was formed. The slurry was then casted into a 8.5 mm diameter polystyrene petri dish mould (Figure 3.1) and placed within a drying chamber (Binder, ED115) at 50 °C for 3 days, so that water could be slowly removed. The dried flexible films were then peeled off the petri dish surface with the assistance of a razor, and freestanding flexible electrodes were acquired (Figure 3.1).

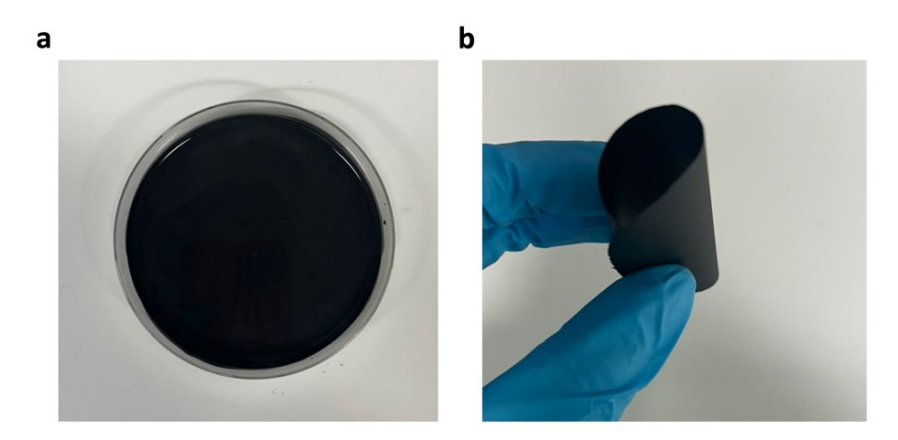


Figure 3.1a) Electrode slurry composed of graphite and nanocellulose fibres, casted into a 8.5 mm diameter polystyrene petri dish mould to dry, b) acquirement of the dried, free-standing and flexible electrode.

3.1.2 Preparation of electrospun cellulose nanofiber/graphite electrodes

3.1.2.1 Nanocellulose electrospinning

Electrospinning of polymer solutions is a valuable technique for the acquirement of free-standing nanofibrous materials, where properties like composition, porosity and thickness can be controlled during the cellulose nanofibrous mat fabrication. The physical intertwining of the polymeric chains promotes the development of nanometre-scale fibres; as a result, the obtained structures are characterised by high surface to volume ratio which is desirable in energy storage applications. Here, electrospinning was performed using a solution of 15 wt.% cellulose acetate (Acros organics, average MW 100,000) in a 2:1 w/w ratio solution of acetone (ThermoFisher Scientific, 99+%) and N,N-Dimethylacetamide (VWR Chemicals), loaded in a plastic syringe (HSW, 10 mL). A needle was attached to the syringe tip, while a syringe pump (NE-300, New Era Pump Systems Inc., USA) and a grounded plate collector (30 × 20 cm) were employed, with a tip-to-collector distance of 15 cm. A potential of 22.5 kV (FC Series, Glassmann High Voltage Inc., USA) was used at a flow rate of 0.5 mL h⁻¹. After their collection, the fibrous mats were deacetylated in a 0.05 M NaOH solution in ethanol for 48 h to regenerate into nanocellulose. Finally, the fibrous mat was rinsed with deionized water until neutral pH was achieved, and then dried at 40 °C overnight.

3.1.2.2 Fabrication of electrospun cellulose nanofiber/graphite electrodes (EL-NCF/G)

An aqueous electrode ink was prepared by mixing graphite and nanocellulose fibres using the process described above. Nanocellulose fibres act as a dispersing agent, enabling the efficient stabilisation of graphite in water. This facilitates the preparation of a homogeneous ink, that can further interact and be incorporated into the electrospun cellulose nanofiber matrix. A small 1.5 \times 1.5 cm rectangular electrospun cellulose nanofiber mat was immersed in the graphite ink and was left to soak for three days at room temperature, until the ink was completely absorbed. The graphite loading was kept at 3.52 mg cm $^{-2}$. The total cellulosic content (nanocellulose fibres and electrospun cellulose nanofiber mat) varied from 50, 60 and 67 wt.%, yielding three electrode compositions. The mat was then placed in a drying chamber (Binder, ED115) at 50 $^{\circ}$ C for three days to slowly remove water, and free-standing electrodes were collected.

3.2 Structural characterisation techniques

3.2.1 Scanning electron microscopy

Electrode microstructure was studied with scanning electron microscopy (SEM) by using a Helios Nanolab 600 dual-beam system, equipped with both an electron, and a Ga⁺ focused ion beam

(Thermo Fisher scientific, USA). The electrode morphology for the nanocellulose/graphite and the electrospun cellulose nanofiber/graphite compositions was first studied with SEM imaging at 5 kV accelerating voltage and under high vacuum, before cycling. In SEM tomography, the focused ion beam was used to remove a thin electrode surface layer and study the morphology of the inner layer. The Ga⁺ beam was placed at a 52° angle perpendicular to the electrode surface and an 85 pA current was applied to remove a thin layer from the electrode surface. At the same time, SEM imaging was performed at the selected surface area, revealing a cross-section of the electrode. The setup can be seen in Figure 3.2 below.

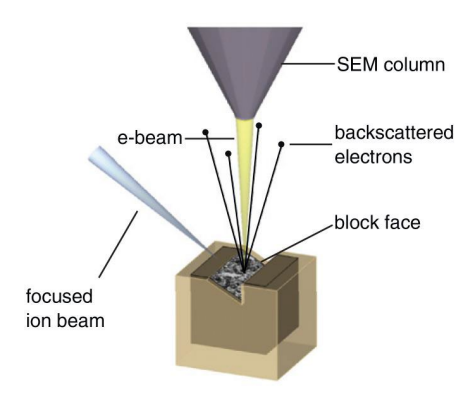


Figure 3.2 Focused ion beam coupled with scanning electron microscopy setup. Reproduced (adapted) with permission from [173]. Copyright 2011 Elsevier Ltd. Published by Elsevier Ltd. All rights reserved.

3.2.2 Atomic force microscopy

An atomic force microscope (Dimension ICON, Bruker Co., USA) located inside a glove box (MBraun, Inertgas-Systeme GmbH, Germany) under argon atmosphere (H_2O <1 ppm, O_2 <1 ppm), was used to perform electrode topography. The measurements were carried out in tapping mode, at a scan rate of 0.5 Hz and with a silicon nitride ScanAssyst-Air probe (Bruker, spring constant 0.4 N/m, resonance frequency 70 kHz, tip radius 2 nm). Post-processing of the images was done using the software Gwyddion.

3.2.3 Solid-state nuclear magnetic resonance spectroscopy

Solid state ⁷Li and ¹H NMR spectroscopy measurements at 14.1 T were performed using an Agilent DD2 600 MHz spectrometer (Agilent Scientific Instruments, USA) equipped with a 3.2 mm, narrow-bore, triple-resonance, T3-style probe and 3.2 mm zirconia rotors. Cross polarization experiments between ⁷Li and ¹H nuclei were also performed. The spin rate was 8.8 kHz. Data were fit in DMFit using Lorenztian line shapes [174] and the fitting parameters can be found in Appendix A2. The quantitative, single-pulse spectra for each sample were fit first to establish the signal positions and intensities, and linewidths were then allowed to vary to fit the

corresponding cross-polarisation spectra which should contain, at most, the same number of resonances and with the same positions. CV was performed at two separate electrochemical cells containing a 60 wt.% NCF/G working electrode, a glassy carbon counter electrode and an Ag/AgCl reference electrode in 0.1 M LiCl/ethanol electrolyte. Scanning was performed in both cases at a potential window of -0.2 to 0.8 V vs. Ag|AgCl and at 0.8 mV s⁻¹ for 5 cycles. For the NMR structural characterisation, the two 60 wt.% NCF/G electrodes were harvested, after pausing the measurement at key potentials of interest. In the first electrochemical cell, scanning was paused before the Li⁺ intercalation reaction, which corresponds to the cathodic peak, while in the second cell, the experiment was paused after Li⁺ intercalation into graphite. After disassembling the electrochemical cells and removing the 60 wt.% NCF/G electrodes from each cell body, residual electrolyte was blotted dry with a wipe and the electrodes were further rinsed with ethanol to remove any remaining Li* traces from the surface. The NMR spectra for single-pulse experiments for both before and after intercalation electrode states were acquired at 8000 scans with 12 s pulse delay. Cross polarisation measurements for the sample before intercalation were carried out at 130000 scans and pulse delay of 0.66 s, with a contact time of 1ms. Finally, cross polarisation measurements for the sample after intercalation were carried out at 12000 scans and pulse delay of 3 s, with a contact time of 1 ms.

3.3 Preparation of electrochemical cells

3.3.1 Three-electrode cell for assessment in Li-ion environment

The as-prepared electrodes were cut into 6 mm diameter circular disks. Three-electrode cells were assembled in a 3/8" perfluoroalkoxy alkane (PFA) Swagelok union tee, using a nanocellulose/graphite working electrode, an Ag|AgCl (sat. NaCl) reference electrode (IJ Cambria), and two 7 mm diameter glassy carbon rods (Alfa Aesar, 99.9% purity) as current collectors and counter electrode, respectively. The reference electrode was sandwiched between two 8 mm diameter glass fiber separators (GF/D, Whatman). The distance between the working and counter electrode was 3.5 mm. The cell was filled with 600 μ L electrolyte, composed of 0.1M LiCl (Alfa Aesar, anhydrous, 99% min.) in ethanol (VWR Chemicals, absolute \geq 99.8%). Ethanol is chosen as a solvent that does not in general cause NCF volume expansion and electrode film disintegration [74].

PTFE tape was used to wrap around the glassy carbon rods and provide a tight fit. The electrolyte background with two glassy carbon rods as working and counter electrode, respectively, against the Ag|AgCl reference electrode. A schematic diagram of the Swagelok cell assembly is shown in Figure 3.3.

Chapter 3

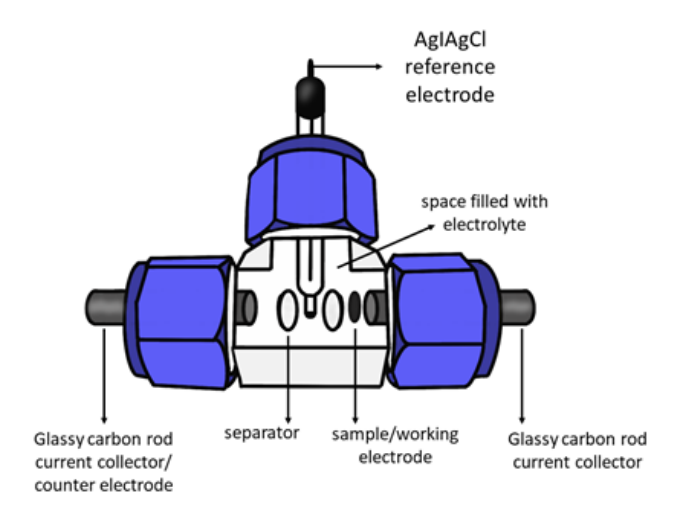


Figure 3.3 Schematic of the three-electrode 3/8" PFA Swagelok electrochemical cell (half-cell), composed of a nanocellulose/graphite working electrode ($A = 0.28 \text{ cm}^2$), two glassy carbon rods ($A = 0.38 \text{ cm}^2$) as counter electrode and current collectors respectively and an Ag|AgCl (sat. NaCl) reference electrode. The cell space was filled with 0.1M LiCl/ethanol electrolyte, and the working and counter electrodes are separated by two GF/D separators ($A = 0.38 \text{ cm}^2$), at a 3.5 mm distance.

3.3.2 Aluminium-graphite two-electrode cells

NCF/G and Al foil (Alfa Aesar, 0.1 mm thick, 99.99% purity) electrodes were cut into 6 mm diameter circular discs. Two-electrode cells were assembled in a 1/4" polytetrafluoroethylene (PTFE) Swagelok tube fitting part, using NCF/G as the positive electrode, and Al foil (Alfa Aesar, 0.3 mm thickness) as the negative electrode. A 7 mm diameter circular GF/D (Whatman) separator was used to isolate the two electrodes. The cell was filled with ~200 μ L of the Lewis acidic (r = 1.5) ionic liquid EMImCl-AlCl₃ electrolyte (Sigma Aldrich). Two molybdenum rods (6 mm diameter; Alfa Aesar, 99.95% purity) were used as the current collectors, and were squeezed to press the whole structure closely. PTFE tape was used to wrap around the molybdenum rods and provide a tight fit. A schematic diagram of the Swagelok cell assembly is shown in Figure 3.4. The OCP of the cells upon assembling was ~ 1.6 V.

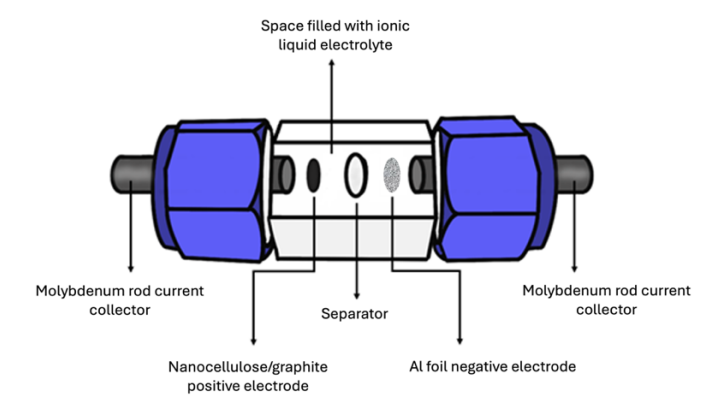


Figure 3.4 Schematic of the two-electrode 1/4" PTFE Swagelok electrochemical cell (full cell), composed of a nanocellulose/graphite positive electrode ($A = 0.28 \, \mathrm{cm^2}$), an Al negative electrode ($A = 0.28 \, \mathrm{cm^2}$) and two molybdenum rods ($A = 0.28 \, \mathrm{cm^2}$) as collectors. The cell space was filled with Lewis acidic (r = 1.5) EMImClAlCl₃ ionic liquid electrolyte and the electrodes are separated by a GF/D ($A = 0.38 \, \mathrm{cm^2}$) separator.

3.4 Electrochemical characterisation techniques

All half-cell electrochemical measurements were performed using a CHI-760E bipotentiostat (CH Instruments, USA) at ambient temperature. All full-cell electrochemical measurements were performed in an inert argon atmosphere (H_2O <1 ppm, O_2 <1 ppm) with a BioLogic SP-150 potentiostat (BioLogic, France) at ambient temperature, unless specified otherwise.

3.4.1 Cyclic voltammetry

Cyclic voltammetry (CV) is an electrochemical technique used to investigate redox processes within an electrochemical system. The electrolyte background was recorded at 0.6 mV s⁻¹ using the three-electrode setup described above, but without the presence of the NCF/G sample. Instead, a glassy carbon rod was used as the working electrode. Variable-rate CV was employed in three-electrode cells with NCF/G or EL-NCF/G working electrode, a glassy carbon counter electrode, an Ag|AgCl (sat. NaCl) reference electrode, in 0.1 M LiCl/EtOH electrolyte to determine the charge storage contributions and the diffusion coefficients, by scanning within a potential window ranging between of –0.2 V and 0.8 V vs. Ag|AgCl, as defined by the electrochemical stability window of the electrolyte. The scan rate was varied from 0.2 mV s⁻¹ to 0.8 mV s⁻¹ to study the redox reactions present in the system, based on previous literature reports concerning ion intercalation reactions in graphite [164].

Variable-rate CV was performed in two-electrode Al-graphite/NCF cells using an NCF/G positive, and Al foil negative electrodes, in Lewis acidic (r = 1.5) chloroaluminate EMImCl-AlCl₃ ionic liquid electrolyte, by scanning within a potential window from 0.5 V to 2.4 V, and the scan rate was varied from 0.4 mV s⁻¹ to 1.0 mV s⁻¹. Charge storage mechanisms were further elucidated by using the methods described thoroughly in Section 2.4. The corresponding faradaic diffusion-limited, faradaic non-diffusion-limited (pseudocapacitive) and capacitive current contributions were calculated by using an open-source MATLAB script [169].

3.4.2 Electrochemical impedance spectroscopy

Electrochemical impedance spectroscopy measurements (EIS) were performed in three-electrode cells to calculate the electrolyte resistance and charge transfer resistance of NCF/G and EL-NCF/G electrodes within 0.1 M LiCl/ethanol electrolyte. The impedance spectra were recorded at the open circuit potential, with a perturbation amplitude of 5 mV and at a frequency range from 500 kHz to 10 mHz. The cells were assessed after the electrodes underwent 20 CV cycles at 1 mV s⁻¹. The data are presented as Nyquist and Bode plots and were further fitted using the Zfit EC-LAB software tool to determine the equivalent circuits.

3.4.3 Galvanostatic cycling

In galvanostatic cycling, a constant current is applied to the nanocellulose/graphite two-electrode cell. To charge the cell, a positive current is used until the upper cut-off potential at 2.4 V is reached; reversely, a negative current is used in order to discharge the cell to the defined 0.5 V lower potential limit. Al–graphite batteries with Lewis acidic (r = 1.5) EMImCl-AlCl₃ ionic liquid electrolyte, demonstrate electrochemical stability of the electrolyte and exhibit charge storage reactions between 0.5 V and 2.4 V. The cells were cycled at charge rates from 5 mA g⁻¹ to 100 mA g⁻¹.

3.5 Flexibility tests

3.5.1 Electrochemical impedance spectroscopy under flexion of electrode

Potentiostatic EIS was performed at OCP by using a BioLogic VSP (BioLogic, France) from 500 kHz to 40 mHz and with a 10 mV amplitude, on a 4.2 cm \times 1.25 cm, 0.06 mm thick NCF/G electrode with a 1 cm \times 1.25 cm contact area, at the non-bent state. Aluminium foil (Alfa Aesar, 0.3 mm thickness) was used at the electrode edges to protect from damage upon clipping the potentiostat cables, and to make electrical contact. The electrode was then bent consecutively at 140°, 180° and >180° angle, while the impedance spectra were recorded at the same time.

The data are presented as Nyquist plots and were further processed to calculate the ohmic resistance and electrode conductivity using the EC-LAB software fitting tool.

The electrode conductivity σ is calculated based on Equation (3-1):

$$\sigma = \frac{l}{R_O A} \tag{3-1}$$

where l is the electrode thickness (0.06 mm), A is the electrode contact area (1.3 cm²), and the ohmic resistance R_{Ω} is calculated from the intercept of the impedance curve with the real axis.

3.5.2 Electrochemical impedance spectroscopy under flexion of full aluminiumgraphite pouch cell

In order to demonstrate the bendability and conductivity retention of assembled full Algraphite/NCF cells, a pouch cell consisting of a rectangular 4×3 cm 60 wt.% NCF/G positive electrode, a rectangular 4×3 cm Al foil (Alfa Aesar, 0.3 mm thickness) negative electrode, and a rectangular 6.5×4.5 cm a GF/D separator (Whatman) was assembled. Two molybdenum foil (Alfa Aesar, 0.1 mm thick, 99.95% metal basis) current collectors were places at the back of each electrode. Current collectors were cut in a flag-like shape, slightly larger than the electrodes, to be able to clip them to the potentiostat cables outside of the pouch. A polypropylene bag and a vacuum sealing tool were used to enclose the cell configuration, partially at first. Then as the pouch was half-open, the separator was soaked with ~500 μ L of Lewis acidic (r=1.5) EMImCl-AlCl $_3$ electrolyte (Sigma Aldrich). The pouch cell was then fully sealed. The cell assembly process and electrochemical measurements were performed under argon atmosphere.

Potentiostatic EIS was performed at OCP by using a BioLogic SP-150 potentiostat (BioLogic, France) from 500 kHz to 10 mHz and with a 10 mV amplitude. EIS spectrum was initially recorded at the pouch cell non-bent state (Figure 3.5a). Afterwards, the pouch cell was bent by immobilising it on a 3 mm wide Falcon tube, and at a bending angle of 114°, and the impedance spectra were recorded at the same time (Figure 3.5b). The data are presented as Nyquist plots.

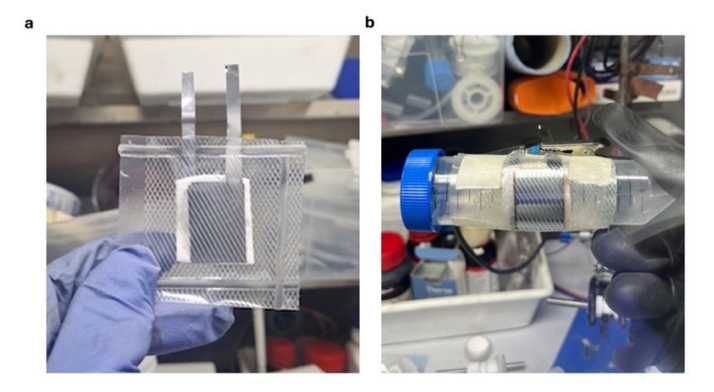


Figure 3.5 Fabrication of flexible pouch aluminium-graphite cells based on nanocellulose/graphite and aluminium electrodes, and Lewis acidic (r = 1.5) EMImCl-AlCl₃ electrolyte, in order to test conductivity retention.

3.6 Preparation of covalently bonded electrode/electrolyte interface

Sol-gel is a method used for the formation of thin films. Chemical sol-gel deposition involves the hydrolysis and condensation of a sol precursor, which can be an alkoxysilane for example, for a gel layer to be formed. The gel is then dried, and a solid film is produced. This process can be conducted via techniques like spin-coating, spraying and coating. Although it is an established, straightforward technique, uniform coatings are tough to acquire. On the contrary, electrochemical sol-gel deposition is a niche technique that offers control over experimental parameters like applied potential, deposition time, concentration of precursor and thus, uniform coatings with controllable thickness can be obtained. Certain restrictions apply however, as electrochemical sol-gel deposition can be carried out on conductive substrates only. The overarching goal is to create a flexible, covalently-attached electrode-electrolyte interface. Covalently-attached electrode/electrolyte interfaces can withstand mechanical deformation and not detach under flexion, as covalent bonds are much stronger than the weak Van der Waals forces that withhold the electrode/electrolyte interface in conventional systems. Also, there is no risk for electrolyte leakage.

From a mechanistic point of view for alkoxysilanes (R = ethyl group for TEOS), first the alkoxyl groups react with water to form silanols, according to the hydrolysis reaction seen in Equation (3-2):

$$\equiv Si - OR + H_2O \rightarrow \equiv Si - OH + ROH \tag{3-2}$$

Then silanols adsorb onto the substrate surface and condensation of silanols takes place via cross-linking, as seen in Equations (3-3) and (3-4):

$$\equiv Si - OH + \equiv Si - OH \rightarrow \equiv Si - O - Si \equiv +H_2O \tag{3-3}$$

$$\equiv Si - OH + \equiv Si - OR \rightarrow \equiv Si - O - Si \equiv + ROH \tag{3-4}$$

Water electrolysis helps generate hydroxyl groups, which increase pH only in close proximity to the working electrode surface leaving the bulk solution unaffected, which in turn triggers the sol-gel reaction (Figure 3.6). It should be noted that a condensation reaction might also take place between silanols and surface hydroxyl groups of the substrate, according to Equation (3-5). In this case, nanocellulose is rich in surface hydroxyl groups.

$$\equiv Si - OH + surface - OH \rightarrow \equiv Si - O - surface \equiv + H_2O$$
 (3-5)

A mixture of ethanol and water is used as a solvent. Ethanol helps with precursor dissolution and water is intrinsically essential for the process. A salt is also used to help facilitate the condensation reaction. Here, electrochemical sol-gel deposition is used to bind the ionic liquid electrolyte onto the nanocellulose/graphite electrode surface, which acts as a conductive substrate. It is a two-step process including: 1) the hydrolysis of an ethanol/water solution and the formation of a silane-gel layer on the electrode surface and 2) binding the ionic liquid electrolyte on the silane-gel surface. As this comprises a complicated process, we aim to the realization of step 1 at this stage. A deposition solution is used in a three-electrode cell containing the nanocellulose/graphite electrode, to electrochemically deposit the silane-gel layer. [175-177]

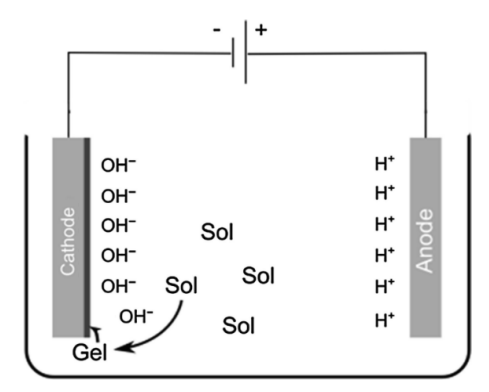


Figure 3.6 Schematic illustration of electrochemical sol-gel deposition. A sol precursor based on alkoxysilanes undergoes hydrolysis yielding silanol groups. The silanol groups then adsorb on the electrode surface and a condensation reaction takes place via cross-linking. The sol-gel process is triggered by water electrolysis which generates OH⁻ and changes the pH only in close proximity to the electrode, leaving the rest of the bulk solution unaltered. Reproduced from with permission from [176]. Copyright 2015 Wiley-VCH Verlag GmbH & Co. KGaA.

3.6.1 Preparation of deposition solution

The deposition solution consists of 30 mL of a 70% ethanol and 30% deionised water mixture where the hydrolysis reaction is based on, 4.19 mL tetraethyl orthosilicate (TEOS) which is the silane source, 0.5 g potassium chloride (KCl) as a salt to increase ion conductivity, and 70 mL hydrochloric acid (HCl) as the reaction is pH sensitive and the environment needs to be slightly acidic.

3.6.2 Cell assembly and electrochemical sol-gel deposition

The three-electrode cell was assembled in a $\frac{1}{4}$ " PTFE Swagelok tube fitting, using a circular 4 mm nanocellulose/graphite as a working electrode, an Ag|AgCl reference electrode (DEK research) and glassy carbon rods (SPI Supplies, \emptyset 5 mm) as a counter electrode and current collectors at the same time. A 5 mm GF/D (Whatman) separator was used to isolate the electrodes, and the cell was filled with the deposition solution. A BioLgic VSP was used for the silane-gel layer deposition. Chronoamperometry was implemented, applying square-wave potential from -1.2 V vs. Ag|AgCl at the working electrode for 10 min and 20 min, respectively. The cell was then disassembled, and the composite was washed with ethanol, and subsequently dried to remove trace water.

3.6.3 Structural characterisation

3.6.3.1 Scanning electron microscopy coupled with energy dispersive x-ray spectroscopy

To study the morphology and elemental composition of the surface of the silane-gel-electrode composite, SEM paired with energy dispersive X-ray spectroscopy (EDX) was employed. Imaging was done in a JEOL JCM-7000 Neoscope under high vacuum. EDX was performed at specific electrode areas, as well as the whole electrode surface to have an estimation of the silane-gel layer distribution.

3.6.3.2 Fourier transform infrared spectroscopy

The covalent bonds between the silane gel and the electrode were studied with Fourier-transform infrared spectroscopy (FT-IR) (Perkin Elmer). First, the background was recorded and then removed from the sample measurements. The acquirement was done using a 70% force, and 36 scans. Post-processing for baseline correction was conducted with OriginLab.

Chapter 4 Study of the nanocellulose/graphite electrode system

This Chapter contains adapted material from E. Founta et al., *ChemElectroChem* (2025), DOI 10.1002/celc.202500096. Available under a CC BY 4.0 licence.

4.1 Structural characterisation

In this section, the surface morphology and microstructure of nanocellulose/graphite electrodes is investigated by SEM. A Ga⁺ focused ion beam (FIB) is then used in parallel with SEM imaging, to perform a cross section of the electrode and examine the innermost layers. AFM was used to perform topography on the electrode and visualise the nanocellulose fibre structure in the nanoscale. Finally, electrode flexibility was assessed by performing EIS under different bending angles.

4.1.1 Electrode microstructure investigation with scanning electron microscopy paired with focused ion beam

Five electrode composition with increasing nanocellulose fibre (NCF) content (40, 50, 60, 67 and 70 wt.%) were fabricated and their surface is mapped by using SEM to correlate electrode morphology with electrochemical analysis results. The morphology of the electrodes is highly dependent of the nanocellulose content, which directly affects homogeneity, porosity and particle interconnectivity.

SEM images in Figure 4.1 reveal structural differences, showing that at 40 wt.% NCF content (Figure 4.1a), and graphite particles are loosely bound by a non-dense NCF network. By increasing the NCF amount to 50 wt.% (Figure 4.1b) some voids in the electrode structure still exist. When a 60 wt.% NCF content is reached (Figure 4.1c), the NCF film structure seems more uniform and composed of a continuous polymer network with embedded graphite particles. The cross-sectional view of the electrode is shown in Figure 4.1f, where the graphite and NCF are hardly distinguishable due to the continuous network character of NCF that covers the graphite particles. As the wt.% NCF is further increased to 67 wt.% (Figure 4.1d), it is apparent that the compact formation is retained. However, when a maximum of 70% NCF is reached (Figure 4.1e), only an excess cellulosic part is only noticeable, which leads to graphite particle wider separation with reduced electrical connection among them. Increasing NCF amount contributed to the formation of smoother and more integral structures, where particle

interconnectivity is promoted. Excessively high amount of the polymer though, disrupt the graphite network.

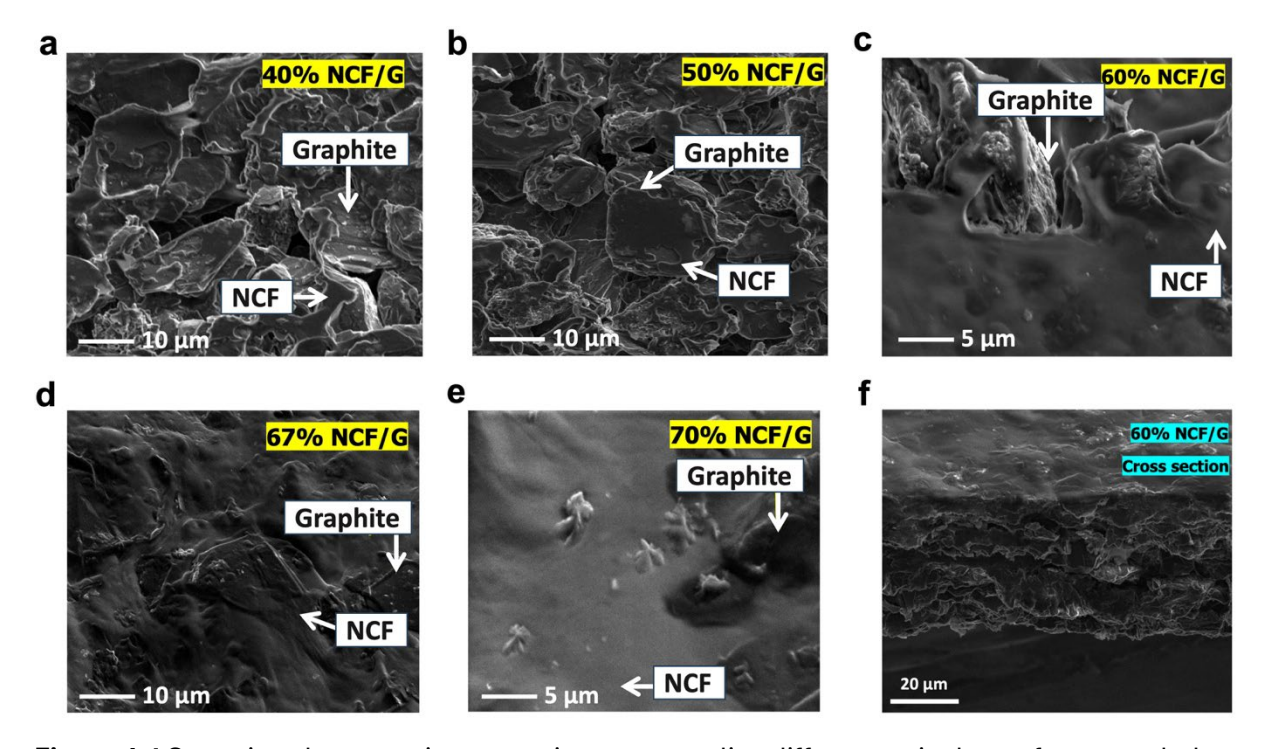


Figure 4.1 Scanning electron microscopy images revealing differences in the surface morphology of the electrodes containing a) 40 wt.% NCF/G, b) 50 wt.% NCF/G, c) 60 wt.% NCF/G, d) 67 wt.% NCF/G, e) 70 wt.% NCF/G. Graphite particles and the NCF network are marked by a white label. f) Vertical cross section of 60 wt.% NCF/G electrode showing a compact structure and good graphite-NCF particle interconnectivity.

To further delve into the inner-morphology and see a horizontal cross-sectional view of the electrode (**Figure 4.2**), FIB was performed on the 60 wt.% NCF/G composition. A few nanometre-thin surface layer was removed near the bottom left region of Figure 4.1c, revealing a porous inmost structure. In cellulosic structures, pores promote electrolyte absorption and subsequent distribution of the ions within the electrode. The outer electrode layer as shown in the left-half section of Figure 4.2a, appears to be more compact which could be possibly owed to the surface casting fabrication process and the existence of surface tension with regard to the electrode slurry. In Figure 4.2a the border indicating the FIB-treated versus the non-treated area, is demonstrated, while Figure 4.2b shows a zoomed part of the FIB-treated area, indicating the distribution of pores with sizes ranging from ~ 10–70 nm. These values are typical for nanocellulose materials.

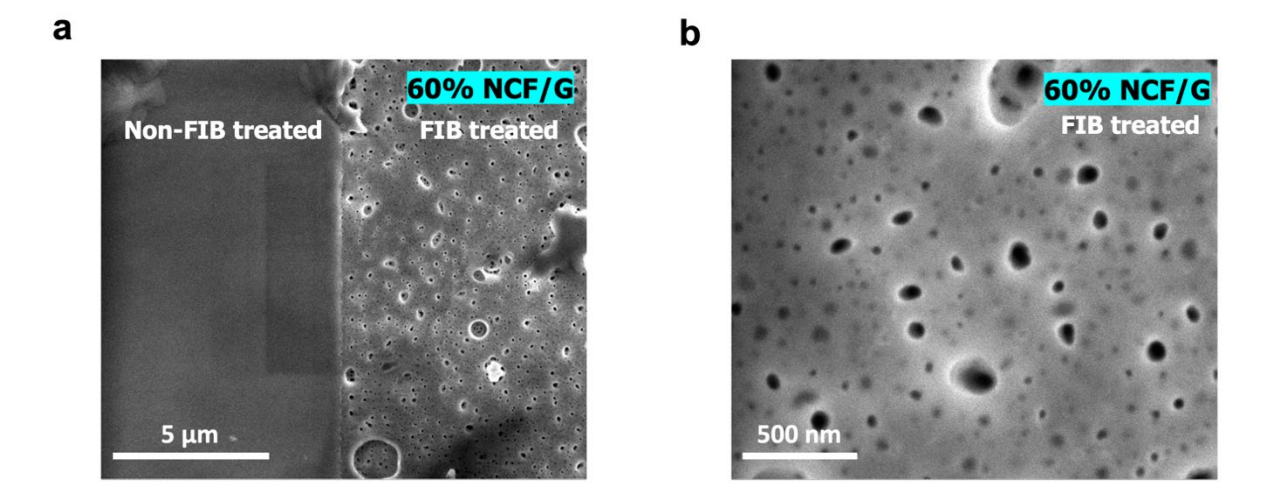


Figure 4.2 Scanning electron microscopy images after Ga⁺ focused ion beam treatment of the surface, revealing a horizontal cross-section and inner morphology of the 60 wt.% NCF/G electrode, showing a) the difference between the non-treated, smooth electrode area versus the FIB-treated area where a porous structure is apparent, b) zoomed region in the FIB-treated area showing porous distribution ranging from ~12–70 nm.

4.1.2 Atomic force microscopy

The interface between graphite particles and the porous NCF fibre network is probed via AFM for a 60 wt.% NCF/G electrode, and it is evident that fibres are organised into larger bundles that form a continuous network around the graphite grains (Figure 4.3a) and have a needle-like shape (Figure 4.3b) of an average 100 nm size. The green marked area indicates the zoomed region where AFM was performed to reveal the NCF network structure shown in Figure 4.3b. Figure 4.3c shows the three-dimensional image of the electrode surface. Here, NCF that that has both hydroxyl and carboxymethyl surface functional groups has been chosen for its facile aqueous processing ability during fabrication, and for its superior affinity towards graphite, as the hydrophobic NCF backbone is successfully adsorbed onto the graphite surface.

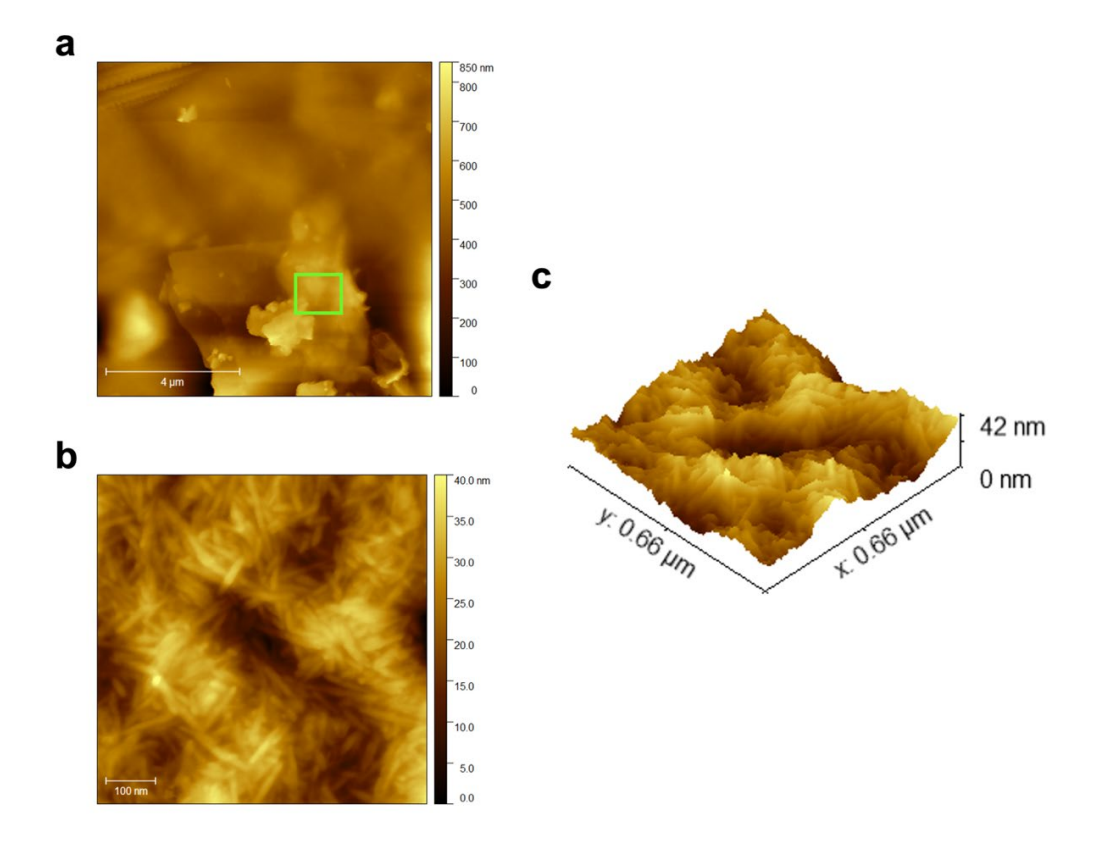


Figure 4.3 Atomic force microscopy images of a) graphite grain covered with the continuous NCF network where the green marked rectangular area represents the zoomed region depicted in b) showing NCF individual fibres that are organised into larger bundles. c)

Three-dimensional image of the electrode surface.

4.2 Evaluation of mechanical flexibility

Electrode bending capability is a parameter that should be considered when battery electrodes are aimed towards their incorporation into flexible electronic devices. In Figure 4.4a-d the flexibility of the 60 wt.% NCF/G electrode when wrapped around a 2.5 cm diameter vial (Figure 4.4b), a 1.1 cm diameter vial (Figure 4.4c) and even twisted around a small 0.7 cm diameter glass pipette (Figure 4.4d), without fracturing, is demonstrated. Thus, the electrode can undergo mechanical deformation both with regard to bending (Figure 4.4a-c) as well as twisting (Figure 4.4d)

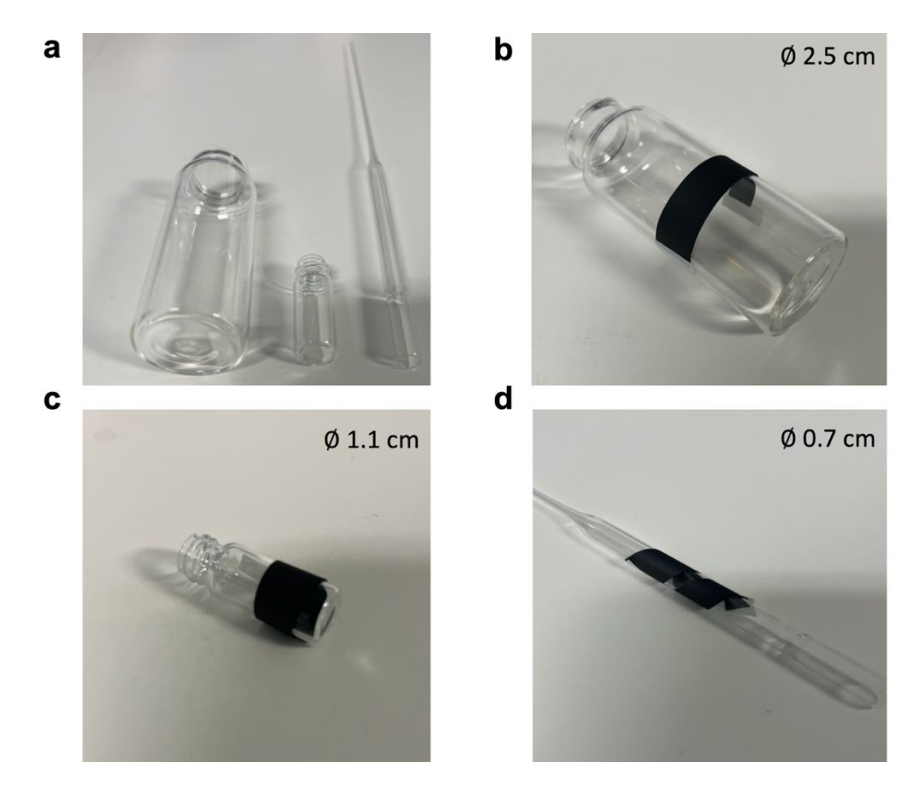


Figure 4.4 Demonstrated flexibility of the 60 wt.% NCF/G electrodes under mechanical deformation, specifically wrapped around a a) 2.5 cm diameter vial, b) a 1.1 cm diameter vial, c) twisted around a 0.7 cm diameter glass pipette without fracturing.

In order to quantify the electrode flexibility however, EIS was performed at the 60 wt.% NCF/G electrode while being initially at the non-bent state, and then at progressively larger bending angles (140° , 180° , $>180^{\circ}$) (Figure 4.5a), as described in Section 3.5.1. The acquired Nyquist plots are shown in Figure 4.5b. A complete lack of the mid-frequency semicircle is apparent as the electrode has not been immersed in a liquid electrolyte environment, hence no interface has been formed. Electrode conductivity σ is calculated from Equation (3-1).

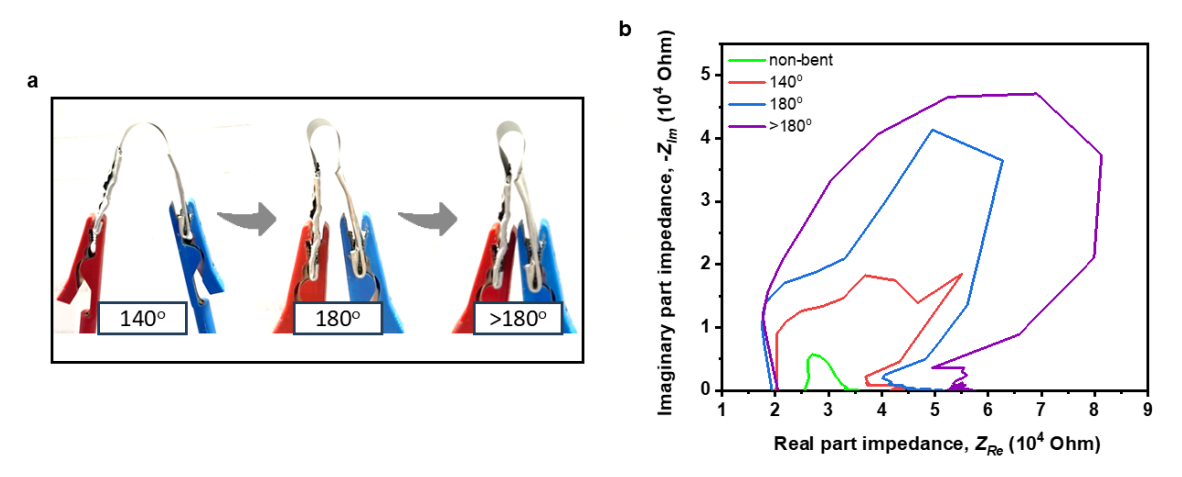


Figure 4.5 a) 60 wt.% NCF/G electrode bent at progressively increasing angles (140°, 180°, > 180°). b) Electrochemical impedance spectra represented as Nyquist plot of the imaginary $(-Z_{Im})$ vs. real (Z_{Re}) part of impedance corresponding to the 60 wt.% NCF/G electrode non-bent state and to 140°, 180°, and >180° bending angles. The x-intercept

 (R_{Ω}) at the same frequency (~ 1.5 Hz) for all electrode bending states is used to calculate the electrode conductivity σ .

From Table 4-1, it can be seen that the electrode conductivity σ undergoes a minor decrease upon transitioning from the non-bent (13.6 × 10⁻⁸ S cm⁻¹) to the 140° bent state (11 × 10⁻⁸ S cm⁻¹). This 19% decrease in electrode conductivity σ is acceptable, given the steep transition from the non-bent state, to a 140° bending angle. Then a further decline of 18% is evident at 180° (9.01 × 10⁻⁸ S cm⁻¹) and additional 3% conductivity loss at the maximum >180° angle (8.7 × 10⁻⁸ S cm⁻¹). Typically, conductivity has been reported to be of higher value for cellulose-based/graphite electrodes,[38, 44] however in this case higher NCF amount is used, which is an inherent electron insulator, with no conductive additives like carbon black.

Table 4-1 Calculated Ohmic resistance and conductivity values corresponding to different electrode bending angles.

Bending angle / º	R_{Ω} / Ohm	σ / S cm ⁻¹	
0 (non-bent)	3.38×10^4	13.6×10^{-8}	
140	4.27×10^4	11 ×10 ⁻⁸	
180	5.12×10^{4}	9.01×10^{-8}	
>180	5.33×10^{4}	8.7×10^{-8}	

4.3 Fundamental understanding of charge storage mechanisms

In this section, the relationship between nanocellulose content, electrode morphology and charge storage mechanisms are examined by disentangling the total current in the relative faradaic diffusion-limited, pseudocapacitive and capacitive contributions. At the same time, solid-state NMR is implemented to study the interactions between the nanocellulose polymer chains and Li⁺ upon charging, to shed more light on the molecular-level phenomena.

4.3.1 Effect of nanocellulose content on the electrode charge storage contributions

Five NCF/G compositions containing an increasing amount of NCF (40, 50, 60, 67 and 70 wt.%) are tested in half-cells composed of each sample as the working electrode, a glassy carbon counter electrode, an Ag|AgCl reference electrode, in a 0.1M LiCl/ethanol electrolyte environment. NCF content is progressively increased to examine the effect on the respective current contributions, with an emphasis on pseudocapacitive characteristics, which are

associated with reduced diffusion limitations. The investigation is conducted by initially performing variable-rate CV.

Prior to the electrodes assessment in half-cells, the electrolyte background is recorded by performing CV at a scan rate of 0.6 mV s⁻¹ and using a glassy carbon rod as working electrode and Ag|AgCl as reference electrode. The electrolyte stability window was determined from -0.2 to 0.8 V vs. Ag|AgCl. As seen in Figure 4.6, the current is purely capacitive, and no redox reactions take place. Beyond the positive and negative electrochemical stability limits in the voltammogram, the slight current increase could be possibly owed to an onset of electrolyte decomposition reactions.

4.3.1.1 Electrolyte stability limits

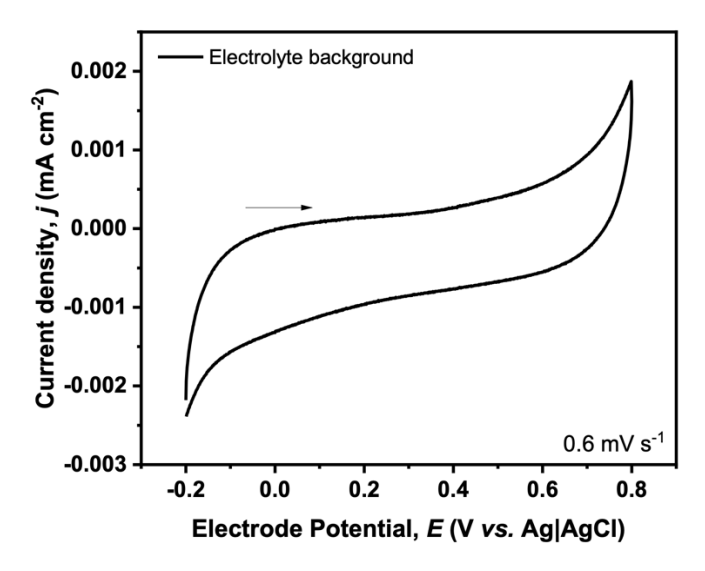


Figure 4.6 CV curve of the electrolyte (0.1M LiCl/EtOH) background performed in a three-electrode cell with glassy carbon working and counter electrodes ($A = 0.38 \text{ cm}^2$) vs.

Ag|AgCl, at a scan rate of 0.6 mV s⁻¹ and T = 25°C. The figure shows the 3rd cycle.

4.3.1.2 Nanocellulose/graphite electrode study using variable-rate CV

Variable-rate CV is then performed in NCF/G three-electrode cells, using scan rates that vary from 0.2 mV s⁻¹ to 0.8 mV s⁻¹ (Figure 4.7). For each scan rate, the 3rd CV cycle is shown in all cases, unless stated otherwise. The redox peaks observed at ~0.35 V vs. Ag|AgCl and 0.55 V vs. Ag|AgCl, correspond to Li⁺ intercalation and de-intercalation into graphite, as previously observed for graphite ion intercalation reactions [164, 178-180]. The specific intercalation/deintercalation reaction for the graphite half-cell is described by Equation (2-1). [181, 182]

Where upon charging (reduction), Li⁺ ions are inserted into the graphite layered structure yielding intermediate graphite-intercalated compounds (Li_xC_x), while upon discharging

(oxidation) Li-ions are de-inserted from the graphite host. It has been previously shown, that NCF combined with ultrasonic treatment contribute to the exfoliation of graphite during fabrication, increasing interlayer distances [183].

From the results in Figure 4.7, it is observed that by increasing n NCF content to 60 wt.% (Figure 4.7c), the highest current density recorded was 0.11 mA cm⁻² at 0.8 mV s⁻¹. Further increase to the NCF percentage leads to current density reduction, with the 70 wt.% composition (Figure 4.7e) yielding a purely capacitive current response. This is justified due to the polymer's lack of electron conductivity, and subsequent increase of resistance at high NCF concentrations. For the high 70 wt.% content, no redox reactions can take place as graphite particles are inaccessible due to the high NCF amount. Thus, no electron transport takes place across the graphite-electrolyte interface. Hence, the current is owed to capacitive phenomena only, and its magnitude is comparable to the recorded electrolyte background as seen in Figure 4.6, confirming that the bulk electrode does not contribute to the total current. Thus, the 67 wt.% NCF/G electrode composition (Figure 4.7d) is considered as the upper limit for electrode functionality, concerning the range of electrode compositions tested in this work.

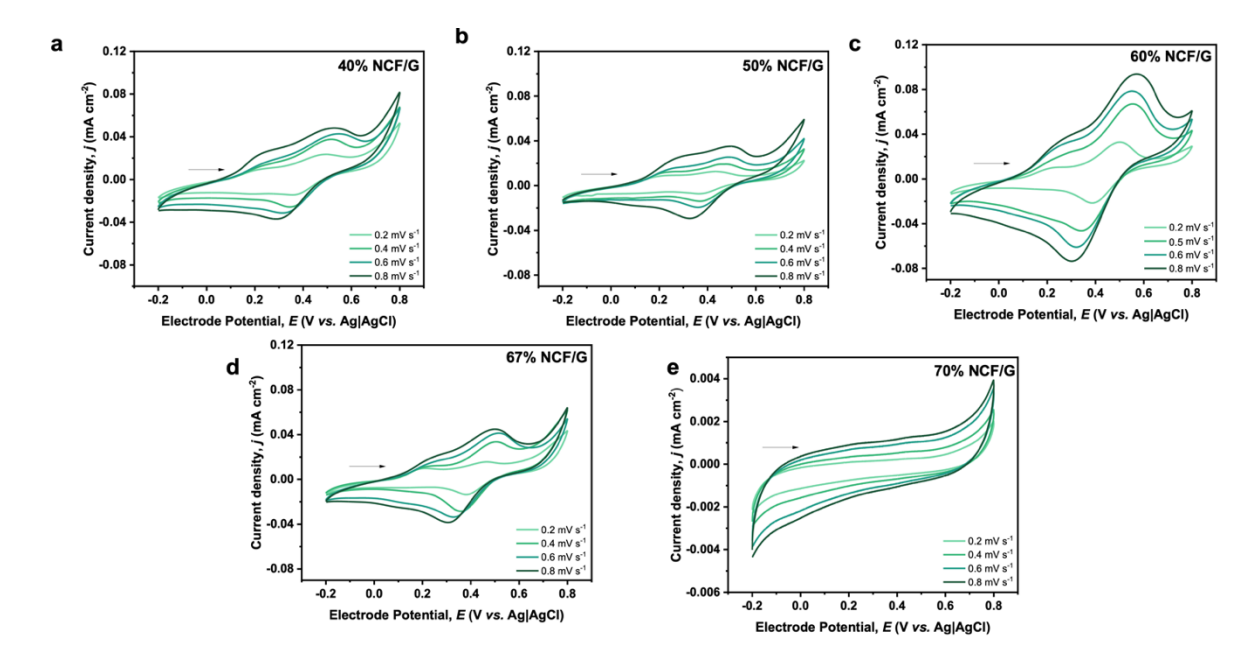


Figure 4.7 Variable-rate CV curves performed in a three-electrode cell vs. Ag|AgCl, with an NCF/G working electrode (A = 0.28 cm²), a glassy carbon counter electrode (A = 0.38 cm²), at scan rates varying from 0.8 mV s⁻¹ to 0.2 mV s⁻¹. CV curves are shown for NCF/G composite electrodes containing a) 40 wt.%, b) 50 wt.%, c) 60 wt.%, d) 67 wt.% and e) 70 wt.% NCF. Each scan rate is shown for the 3rd cycle.

4.3.1.2.1 Dunn analysis

Li⁺ intercalation into graphite is in general a faradaic diffusion-limited process in conventional graphite electrodes. In electrode systems, the relative current contributions of faradaic diffusion-limited and (pseudo)capacitive current can be quantified by using the "Dunn method" as described in Section 2.4.2, which is based on the relationship between the non-diffusion-limited current scaling linearly with the scan rate ($i \sim v$), and the faradaic diffusion-limited current scaling with the square-root of the scan rate ($i \sim v^{0.5}$). Pseudocapacitive and true capacitive current can be further disentangled, and all of the aforementioned current contributions add up to the total current i(v) recorded for a sample.

Here, an intermediate scan rate of 0.6 mV s⁻¹ was chosen for the current deconvolution for each one of the NCF/G samples (Figure 4.8a-d), and the analysis was performed by using an open-source MATLAB script to disentangle the relative current contributions at each measured point of the CV. The 70 wt.% NCF/G sample was not further analysed as the total current recorded was purely capacitive in nature and no redox reactions take place.

Increasing NCF content within the electrode from 40 wt.% to 50 wt.% and then up to 60 wt.% yields higher pseudocapacitive contributions, reaching a maximum of 43% pseudocapacitive current for the 60 wt.% NCF composition (Figure 4.8c). On the other hand, the faradaic diffusion-limited current appears to follow the opposite trend, decreasing in the presence of higher wt.% NCF in the electrode. As the diffusion limitations are getting lower with higher wt.% NCF, the Faradaic diffusion-limited component is transformed to pseudocapacitive, which is still Faradaic in nature, but not limited by diffusion. Pseudocapacitive current becomes lower after further increase of NCF from 60 wt.% to 67 wt.%. However, the pseudocapacitive current for 67 wt.% NCF, remains higher compared to pseudocapacitive current for 50 wt.% NCF. This observation still reinforces the increase of mass transport with cellulosic content. This link between nanocellulose and pseudocapacitive characteristics is revealed for the first time.

Pseudocapacitive behaviour within the electrode upon NCF content increase, is owed to the existence of more pathways available for ion diffusion occurring through the nanochannels reaching the bulk of the electrode. It is additionally attributed to the shorter diffusion distances to reach graphite, due the porous nature of NCF. As a result, the rate of diffusion becomes very fast compared to the rate of the electrochemical reaction, giving rise to this improved pseudocapacitive characteristics. Thus far, the 60 wt.% NCF/G electrode demonstrated the highest pseudocapacitive contributions and appears to be the optimum composition among the electrodes tested.

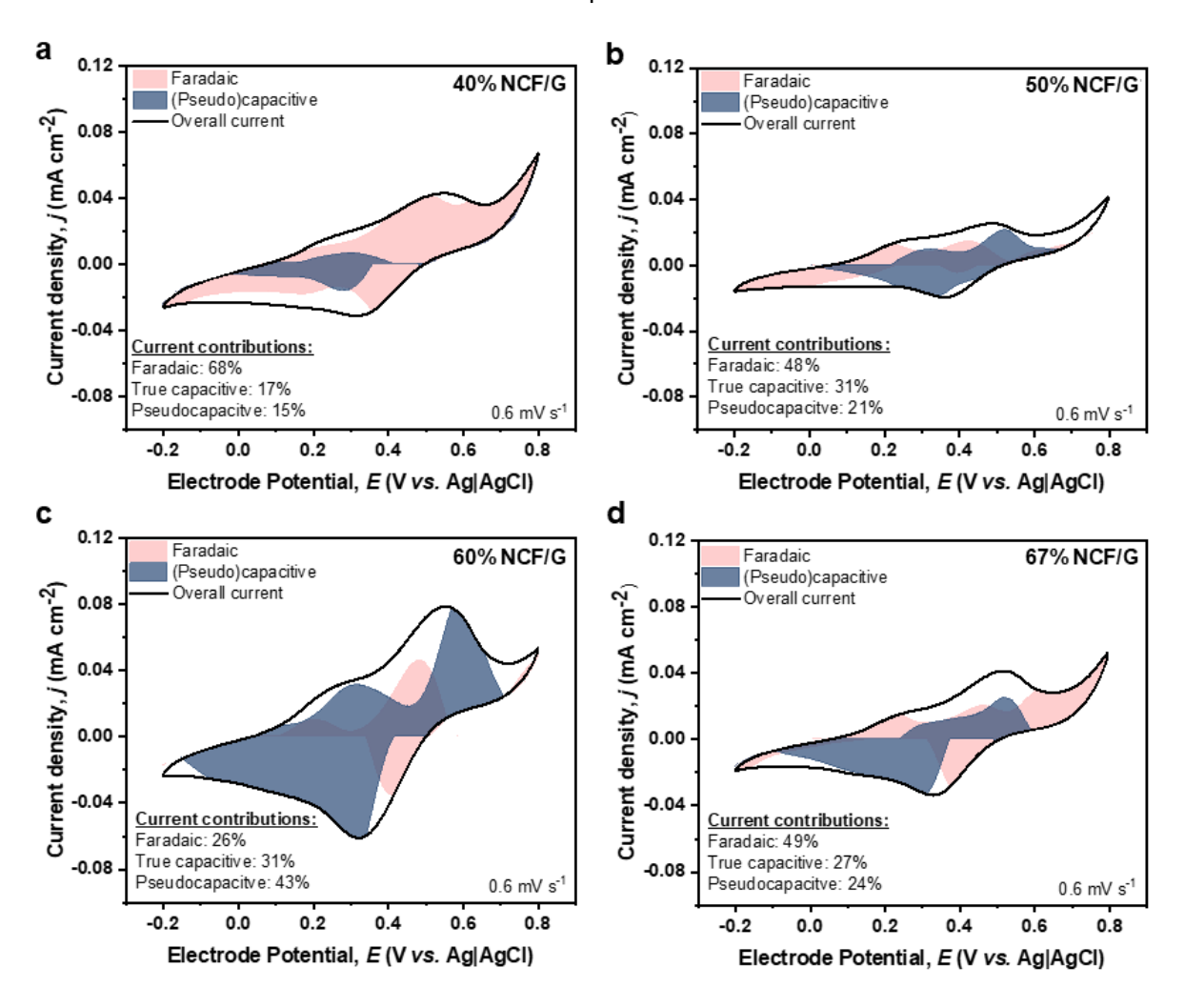


Figure 4.8 Deconvoluted cyclic voltammograms performed in a three-electrode cell *vs.* Ag|AgCl, with an NCF/G working electrode ($A = 0.28 \text{ cm}^2$) and glassy carbon counter electrode ($A = 0.38 \text{ cm}^2$) at 0.6 mV s⁻¹ scan rate, demonstrating the relative faradaic diffusion-limited (light red area), and (pseudo)capacitive current contributions (blue area) for a) 40 wt.%, b) 50 wt.%, c) 60 wt.% and d) 67 wt.% NCF in composite NCF/G electrodes. (Pseudo)capacitive current is further deconvoluted to true capacitive and pseudocapacitive contributions, the respective percentages of which are also indicated. For each wt.% NCF content, the 3rd cycle of the recorded voltammograms was used in this analysis.

4.3.2 Determination of diffusion coefficients

The variable-rate cyclic voltammograms for each graphite/NCF electrode composition, were also used to determine the diffusion coefficients of the Li⁺ ion during intercalation by using the Randles-Ševčík Equation (4-1) for T=25°C.

$$i_p = 2.69 \times 10^5 \, n^{\frac{3}{2}} AC \, \sqrt{Dv} \tag{4-1}$$

Where i_p is the peak current (A), n is the number of transferred electrons which here is taken as equal to 1, A is the electrode area (cm²), D is the diffusion coefficient (cm² s⁻¹), C is the bulk concentration (mol cm⁻³), and v is the scan rate in (mV s⁻¹). The peak current i_{pc} of the cathodic reaction is plotted against the square root of the scan rate v¹¹² yielding a linear curve (Figure 4.9a-d).

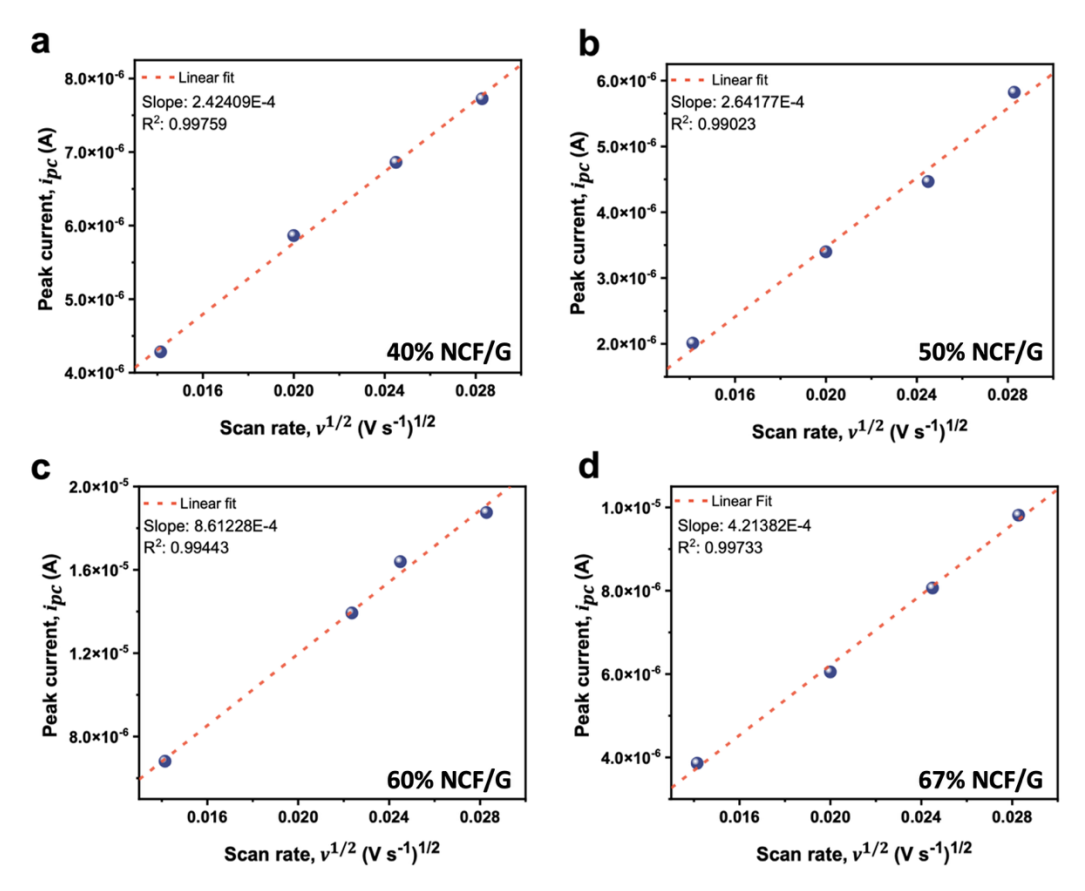


Figure 4.9 Cathodic peak current (i_{pc}) vs. scan rate $(v^{1/2})$ plots. Linear fitting applied for slope calculation and subsequently diffusion coefficient evaluation via the Randles-Ševčík equation. Analysis is performed for samples containing a) 40 wt.%, b) 50 wt.%, c) 60 wt.%, and d) 67 wt.% NCF in composite NCF/G electrodes.

By determining the slope and using the Randles-Ševčík equation, the diffusion coefficients can be calculated. It should be noted that this equation is restricted to faradaic diffusion-limited reactions for the calculation of the diffusion coefficient. Thus, the values that are acquired here represent the effective diffusion coefficient that does not distinguish between the underlying charge storage mechanisms. In this case, the diffusion coefficient values can only be compared qualitatively.

The determined values follow a similar trend as the pseudocapacitive contributions, increasing with increasing wt.% of NCF. The highest diffusion coefficient was evaluated again for the 60 wt.% NCF electrode at 1.22×10^{-8} cm² s⁻¹ which also exhibited the lowest diffusion limitations from the variable-rate CV analysis, and as a result, this explains the improved ion mobility

properties (Figure 4.10). The value is higher compared to the ones reported for conventional graphite electrodes previously in literature. This composition presents the optimum NCF to graphite ratio as well as the most adequate NCF channel network, structurally (Figure 4.1c). These led to improved pseudocapacitance (Figure 4.8c), reduced mass transport restraints and highest diffusion coefficient.

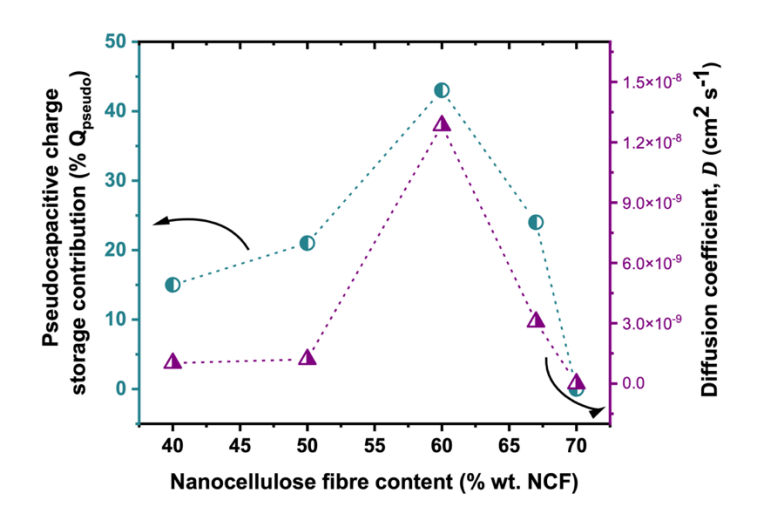


Figure 4.10 Diffusion coefficients and relative proportion of pseudocapacitive current contributions as function of wt.% NCF in NCF/G composite electrodes.

4.3.2.1 Correlation to electrode morphology

As described in Section 4.1.1, structural differences between the variable NCF content electrodes are apparent. From the electrochemical analysis, it was shown that the 60 wt.% NCF electrode yielded the highest pseudocapacitive current contributions and diffusion coefficient. Structurally, the electrode is composed of a uniform NCF network enfolded around graphite particles (Figure 4.1c), which seems to concur to the improved ion transport properties. As the NCF content is further increased to 67 wt.% the compact structure is preserved (Figure 4.1d), and the ion diffusion coefficient appears as the second-highest value. On the contrary, the 40 wt.% (Figure 4.1a) and 50 wt.% (Figure 4.1b) NCF/G compositions are characterised by a loosely bound graphite-NCF network, and thus exhibiting more hindered mass transport both among NCF fibres, as well between NCF and graphite. It is highlighted that in the compositions where the highest pseudocapacitive characteristics were attributed, i.e. the 60 wt.% (Figure 4.1c) and 67 wt.% (Figure 4.1d), NCF/G, NCF appears as a continuous film, promoting efficient mass transport.

4.3.3 Evaluation of electrode charge transfer resistance

4.3.3.1 Nyquist and Bode plots

To determine the charge transfer resistance R_{ct} of the variable NCF/G electrode compositions, EIS was performed at the open circuit potential after 20 CV cycles at 0.8 mV s⁻¹. The results are shown as comparative Nyquist plots in Figure 4.11. The focus was put on the study of the high and mid-frequency region (500 kHz–15 kHz) of the Nyquist plots. That is because the high-frequency region is dominated by ohmic resistance, while the mid-frequency region is representative of R_{ct} . It is evident that all electrode compositions exhibit a characteristic semicircle, indicative of the electrolyte-electrode interface, the diameter of which is equal to R_{ct} . R_{ct} decreases with increasing wt.% of NCF content, owed to more facile ion transport. The trend liaises with results from the CV and diffusion coefficient analysis, whereby increasing the NCF content from 40 wt.%, to 50 wt.% and reaching 60 wt.%, pseudocapacitive contributions and the diffusion coefficient both increase, while R_{ct} is decreased revealing less-hindered ion transport. Onwards at 67 wt.% NCF, pseudocapacitive contributions and diffusion coefficient values decrease while R_{ct} increases.

From the Nyquist plots, the ohmic resistance R_{Ω} referring to the electrolyte plus the cell connections resistance, can be also deducted, by evaluating the x-intercept at the high frequency region (500 kHz – 15 kHz). R_{Ω} is equal to 12 Ohm and sustains this value for all electrode compositions. The results that summarise the R_{ct} values linked to NCF content are presented in Table 4-2.

Table 4-2 Charge transfer resistance value as calculated from the Nyquist plot in Figure 4.11, in correlation with wt.% NCF content, within composite graphite/NCF electrodes.

wt.% NCF	R _{ct} /Ohm
40	589
50	492
60	248
67	390

The EIS results with regard to an electrochemical system, can be fit and simulated to an equivalent electrical circuit, made up of resistors, capacitors and inductors. Here, the spectra were fit with an equivalent circuit made up of a resistor (R1) which corresponds to the bulk electrolyte resistances, a parallel circuit of (R2/Q2) characteristic of the charge transfer

resistance and a (R3 + W3/Q3) element which models mass transport at the porous electrochemical interface.

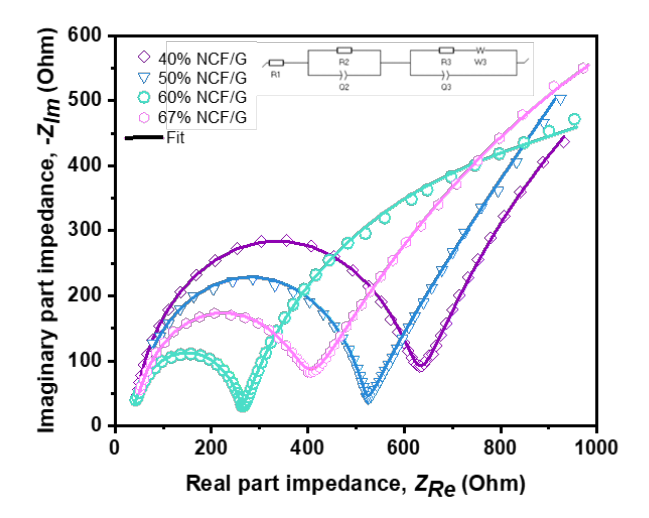


Figure 4.11 Electrochemical impedance spectra shown as Nyquist plot of the imaginary $(-Z_{Im})$ vs. real (Z_{Re}) part of impedance. The high-frequency region (500 kHz to 40 Hz) of the spectra is depicted, for variable-NCF content electrodes. The electrodes were assessed in half-cells with glassy carbon counter electrode ($A = 0.38 \text{ cm}^2$) vs. Ag|AgCl. Equivalent circuit representing the NCF/G electrode system (inset).

In Figure 4.12, the comparative Bode plots show how the phase angle and the absolute value of the impedance logarithm trend in relation to frequency. Phase angle is representative of mass transfer processes. The 60 wt.% NCF/G electrode exhibits overall the lowest impedance Z over the whole frequency region (Figure 4.12b), confirming facilitated mass transport. This correlates with the observed increased pseudocapacitance for the 60 wt.% NCF/G electrode structure (Figure 4.8c).

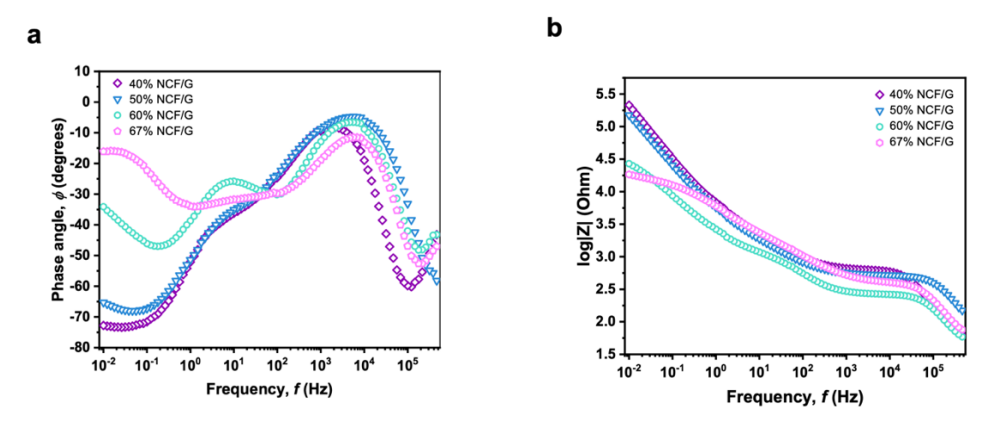


Figure 4.12 Comparative Bode plots for the variable-NCF content NCF/G electrodes (A = 0.28 cm²), assessed in half-cells with a glassy carbon counter electrode (A = 0.38 cm²) vs. Ag|AgCl, showing a) the phase angle as a function of frequency, b) log|Z| as a function of frequency.

4.3.4 Molecular-level understanding of nanocellulose-ion interactions

4.3.4.1 Solid state NMR

CV was performed in two separate half-cells containing a 60 wt.% NCF working electrode in each case, and scanning was stopped before and after the cathodic peak appearance (~ 0.35 V vs. Ag|AgCl), which correspond to before- and after- Li⁺ intercalation states, respectively. The two harvested electrodes were then rinsed with ethanol and blotted dry to remove trace amounts of surface Li⁺.

Solid-state NMR is implemented to study the interactions between NCF polymer chains and Li⁺ upon charging, to shed more light on the molecular-level phenomena. Figure 4.13 shows solid-sate ¹H single-pulse spectra acquired for the two 60 wt.% NCF/G electrodes shortly before (top) and after (bottom) intercalation. In this electrode, NCF is the main source of protons. Before intercalation, the main ¹H signal is found at 3.9 ppm, a shift in the expected range for the carbomethoxy protons in NCF. However, after intercalation the bulk signal is shifted to 9.8 ppm and is significantly broadened, while spinning sidebands also appear; note that a small amount of signal remains around 4.0 ppm, likely due to unreacted material. Spinning sidebands exist when spinning is slower than the chemical shift anisotropy, and here this could be indicative of partial symmetry loss. Signal broadening and shifting could be also attributed to stronger paramagnetic effects related to delocalised electrons in graphite.

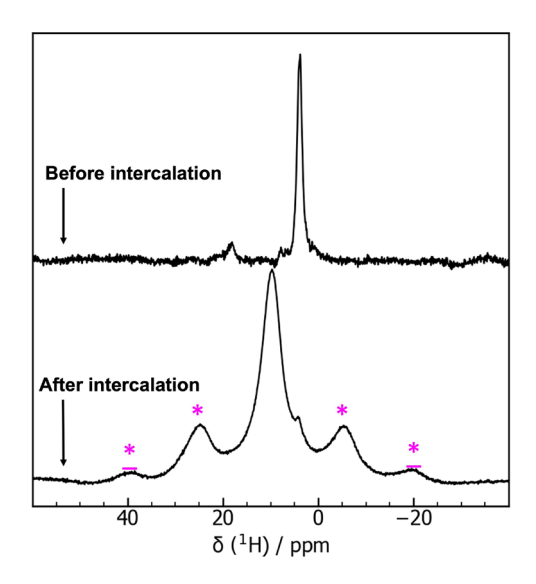


Figure 4.13 Solid state ¹H spectra before (top) and after (bottom) intercalation within a 60 wt.% NCF/G electrode.

Cross-polarisation (CP) experiments, correlating ⁷Li and ¹H nuclei on electrodes just before and just after intercalation at 0.35V during CV, were also acquired (Figure 4.14). Two ⁷Li signals exist both before and after intercalation as seen from the fitted data (brown- and green-coloured areas), indicating a wide distribution of environments for ⁷Li. Before intercalation, the ⁷Li brown

signal (more negative) is strongly coupled to ¹H compared to the ⁷Li green signal (more positive), as determined by their relative integrals in the CP. This means that ⁷Li of the brown signal are statistically closer in space to the ¹H than ⁷Li of the green signal. After intercalation, the green-indicated positive signal becomes larger as compared to the brown negative signal, indicating a stronger interaction with ¹H. This interplay in ⁷Li signals is probably linked to graphite and NCF interactions in terms of different domains, ratios etc. within the electrode. This would justify the distribution of signals, as ⁷Li is expected to interact differently. Before intercalation, ⁷Li resonances are observed at 9.4 ppm and –32.2 ppm. After intercalation, deconvolution of the ⁷Li CP experiment revealed two signals at 7.1 and –24.5 ppm. The resonance around 7.1 ppm (green signal) likely corresponds to the same environment at 9.4 ppm in the pre-intercalation sample due to unreacted material. The new resonance at –24.5 ppm (brown signal) is strongly shifted and broad in nature, indicating a distribution of ⁷Li environments and a paramagnetic interaction, as observed in the ¹H NMR results. This new signal is therefore expected to be a direct result of the intercalation event.

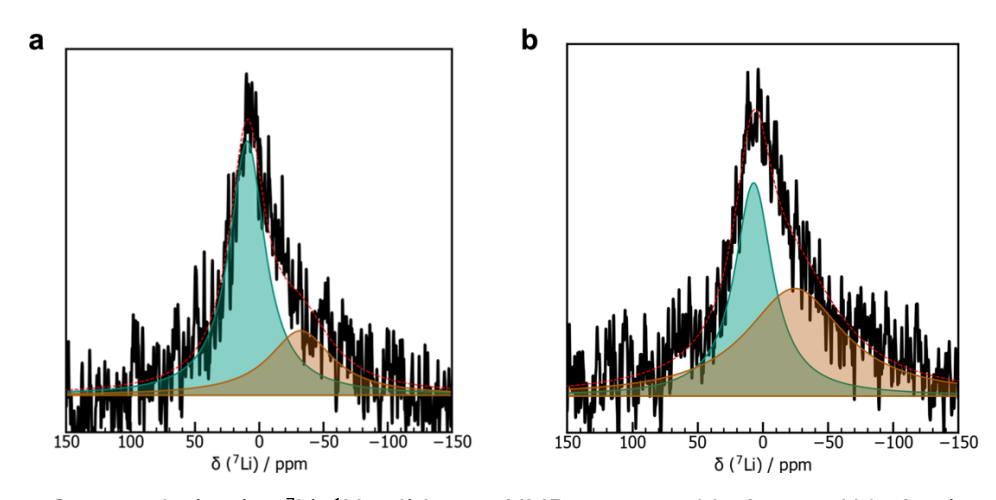


Figure 4.14 Cross polarisation ⁷Li–¹H solid state NMR spectra, a) before and b) after intercalation within a 60 wt.% graphite/NCF electrode. The brown and teal signals represent the fitted data as relative signal integrals.

In quantitative experiments (Figure 4.15), the two ⁷Li signals integrate to 86.9% and 13.1% of the total signal for the resonances at 9.4 ppm and –32.2 ppm, respectively in the material before intercalation. After intercalation, the signal at 7.1 ppm contains 71.2% of the total, and the signal at –24.5 ppm contains 28.8% of the total, indicating that the lower-frequency signal is increasing in intensity immediately following the reaction at 0.35 V, as is expected for a site associated with charge storage. The existence of ⁷Li signal in the CP experiment is proof that ⁷Li interacts with ¹H species (that mainly stem from NCF), as CP measurements necessitate dipolar coupling between the two species, which occurs as a result of a relatively immobile ⁷Li species within sub-nanometre proximities of ¹H species. This confirms that NCF molecular chains form nanochannels between them, through which Li⁺ ion transport is accommodated

from the electrolyte to the bulk of graphite, where then intercalation takes place. This can be facilitated through interactions between the positively-charged Li⁺ and the negatively-charged surface –OH⁻ and –CH₂COO⁻NCF molecular chain surface groups which are exposed within the nanochannels. The change in the signal shape transitioning from before- to the afterintercalation state, is linked to the contribution of the actual Li⁺ intercalation signal.

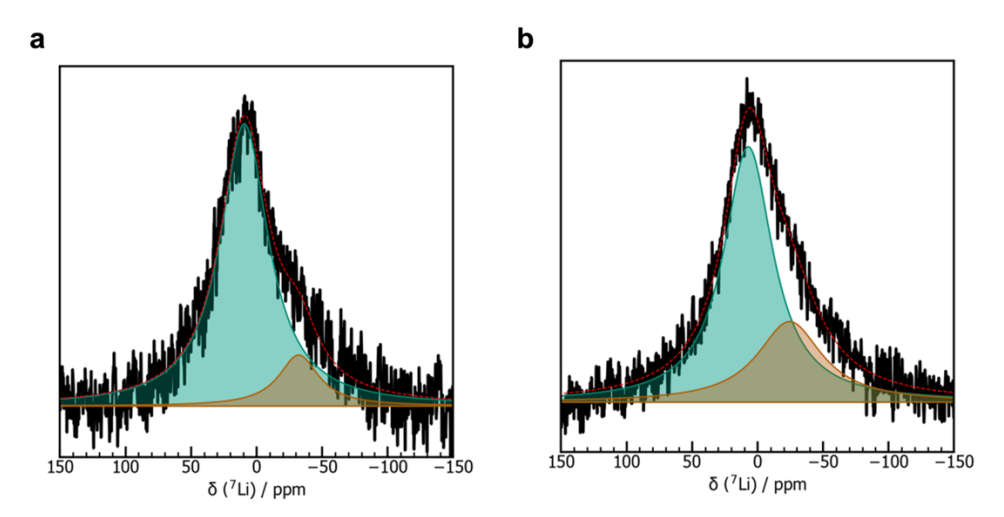


Figure 4.15 Single pulse solid state ⁷Li NMR spectra, a) before and b) after intercalation for a 60 wt.% NCF/G electrode. The brown and teal signals represent the fitted data, as relative signal integrals.

Efficient Li⁺ intercalation and deintercalation has been proven to occur within the 60 wt.% NCF/G sample from previous solid state ⁷Li NMR measurements, where a two-electrode cell was used (Appendix A).

4.4 Chapter summary

In this chapter, the microstructure of five NCF/G electrode compositions containing increased amount of NCF was examined with SEM. A loosely bound graphite-NCF network was revealed for the compositions containing 40 and 50 wt.% NCF/G, while a smother, more uniform morphology was apparent for the compositions containing higher amount of NCF, i.e. 60 and 67 wt.%. On the other hand, where excessive 70 wt.% NCF amount was used, graphite particles seem to be disconnected and completely separated by NCF. This would lead to electron conductivity decrease. Further analysing the structure of the 60 wt.% NCF/G electrode in the nanoscale, the acquired AFM images reveal an NCF structure of organised smaller fibrils, that manifest as a continuous network in the SEM images, which is then in contact with the graphite particle surface. The NCF/G electrode flexibility was demonstrated by performing EIS under three different bending angles and assessing the electrode conductivity σ in each case. A bending angle of 180° was achieved, with an acceptable conductivity loss from 13.6 × 10-8 S cm⁻¹ at the non-bent state, to 9.01 × 10-8 S cm⁻¹ for a 180° fully bent state.

Additionally, the five electrode compositions with variable NCF content were assessed in Li⁺ environment half-cells. Variable-rate CV experiments showed the highest current density was achieved by the 60 wt.% NCF/G composition at 0.11 mA cm⁻². Notably, this is a composition where no conductive additives are incorporated, and high NCF materials are chosen in order to understand the fundamental role of the material. The 70 wt.% NCF/G sample demonstrated exclusively capacitive behaviour with a current density comparable to the electrolyte background, showing that no reaction can be facilitated due to the high amount of the electrically insulating nanocellulose. The results for the remaining four compositions, 40 wt.%, 50 wt.%, 60 wt.%, 67 wt.% NCF/G, were used in a subsequent Dunn analysis where the total current was deconvoluted in the respective faradaic diffusion-limited, capacitive and pseudocapacitive contributions. The aim was to correlate NCF amount with the pseudocapacitive proportion, as it is indicative for facilitated mass transport. It was demonstrated that NCF enhances ion mass transport in graphite electrodes, showing a clear trend of improved pseudocapacitive characteristics with increasing NCF content, peaking at 60 wt.% NCF/G with 43% charge contribution, and then at 67 wt.% NCF/G with 24% charge contribution. Diffusion coefficients were then evaluated and used as a qualitative tool using the Randles-Ševčík equation. The values appear to follow the same trend as pseudocapacitive percentages in correlation to NCF content, with the maximum evaluated for the 60 wt.% NCF/G at 1.22×10^{-8} cm² s⁻¹. Structural data liaise with the electrochemical performance characteristics presented in this chapter, as the electrodes exhibiting a morphology based on a compact NCF network smoothly integrated with graphite particles, showed the best diffusion coefficients (60 wt.% and 67 wt.% NCF/G) and thus the most efficient mass transport, compared to the structures where NCF network was not densely packed around graphite (40 wt.% and 50 wt.% NCF/G).

EIS data align with the variable-rate CV analysis and diffusion coefficient data. A reduction in charge transfer resistance with increasing NCF content is showcased. The lowest value at 250 Ohm, was shown for 60 wt.% NCF/G. Charge transfer resistance is indicative of the resistance of ions transport phenomena at the electrode/electrolyte interface.

Solid state 7 Li and 1 H NMR experiments were performed to understand the speciation of the environment surrounding 7 Li before and after intercalation, within the graphite-NCF network. 1 H signal broadening and shifting after intercalation is indicative of the Li $^{+}$ charge storage process, due to the increase in paramagnetic effects from graphite unpaired electrons. Distribution of environments for 7 Li was revealed from cross polarisation 7 Li ${}^{-1}$ H spectra. 7 Li nuclei are located at a < 1 nm distance from the NCF 1 H, which aligns with electrochemical data demonstrating ion transport properties of NCF, from the electrolyte to graphite. Li ${}^{+}$ intercalation is shown by changes to 7 Li signal shape and intensity.

Chapter 5 Correlation of nanocellulose architecture to ion mass transport

This Chapter contains adapted material from E. Founta et al., *ChemElectroChem* (2025), DOI 10.1002/celc.202500096. Available under a CC BY 4.0 licence.

This Chapter investigates the effect of nanocellulose structure modification on the electrode morphology, ion diffusion coefficients and charge storage mechanisms, by disentangling the total current into the relative faradaic diffusion-limited, capacitive and pseudocapacitive current contributions. Electrospun cellulose nanofibers (EL-NCF) were used, replacing of nanocellulose fibres (NCF) within the nanocellulose/graphite electrodes. Moreover, EIS was used to calculate the R_{ct} of the EL-NCF/G electrodes. The results are correlated to the NCF electrode characteristics as detailed in Chapter 4.

5.1 The electrospun nanocellulose/graphite electrode

Electrospinning is a straightforward approach implemented for the fabrication of cellulose nanofibers, characterised by exceptionally high aspect ratios, robust interconnectivity and high porosity, due to the arbitrary distribution of the nanofibers. The method provides control on the nanocellulose fibre structure as described in Section 2.1.1.1.1. As a result, the key structural differences between NCF-based and EL-NCF based electrodes, are a continuous film structure for NCF vs. a network made of discreet, high surface area nanofibers. In the case of EL-NCF, increased porosity also exists. Thus, different particle interactions between EL-NCF and graphite compared to NCF and graphite, are expected. The electrode illustration is depicted in Figure 5.1 below. Electron transfer takes place in the interlayers of the graphite particles and mass transport happens through the EL-NCF channels. It is anticipated that ion mass transport would be affected due to the nanocellulose architectural alteration, as properties like particle aspect ratio, fibre length and porosity are important factors that affect electrolyte absorption and further ion mass transport to the redox active material.

Here, three electrode compositions with increasing EL-NCF content (50 wt.%, 60 wt.% and 67 wt.%) are manufactured and examined. These three specific compositions were chosen as at this nanocellulose content, the highest pseudocapacitive characteristics were observed, as deduced in Chapter 4.

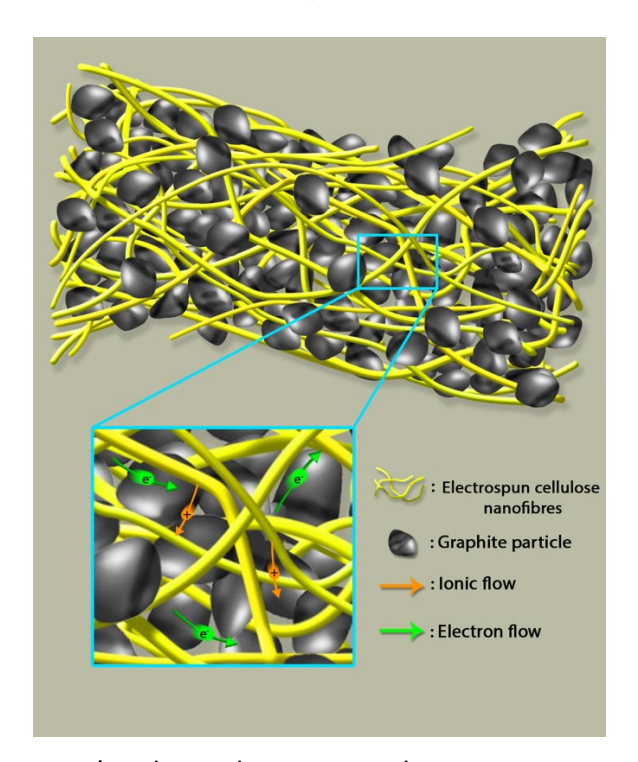


Figure 5.1 EL-NCF/G composite electrode structure. Ion mass transport happens through the electrospun fibrous network, while electron transfer occurs in the interlayers of the graphite particles. The highly porous structure absorbs Li⁺ from the organic electrolyte, transferring them to the redox active material (graphite) where ion intercalation takes place.

5.1.1 Electrode morphology

SEM analysis was performed to examine the surface structure of the 60 wt.% EL-NCF/G electrode. Structural differences are clearly distinguishable compared to the NCF-based electrodes (Figure 4.1c). Here, EL-NCF individual fibres and higher void space among these are discernible (Figure 5.2), contrary to the continuous NCF film-like network revealed in Section 4.1.1.

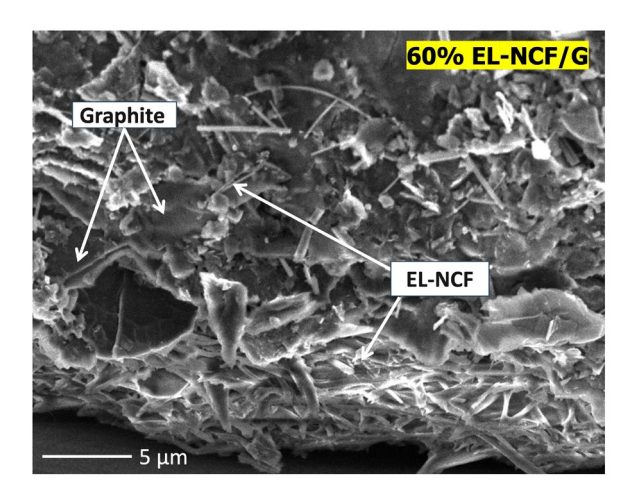


Figure 5.2 Scanning electron microscopy images revealing the surface morphology of the 60 wt.% EL-NCF/G electrode, where distinguished, high aspect-ratio electrospun cellulose nanofibrils are entangled and interconnected with graphite particles.

5.2 Investigation of charge storage mechanisms

Variable-rate CV was performed in three-electrodes cells with a Li $^+$ -containing organic electrolyte to study the influence of cellulose structure in the composite electrode. The same potential window of -0.2 to 0.8 V vs. Ag|AgCl was chosen, and the three electrode compositions that were examined are for a 50 wt.% (Figure 5.3a), 60 wt.% (Figure 5.3b) and 67 wt.% (Figure 5.3c) EL-NCF content in EL-NCF/G electrodes, and at scan rates varying from 0.8 mV s $^{-1}$ -0.2 mV s $^{-1}$. Each scan rate is shown for the 3^{rd} CV cycle.

Seemingly, only the compositions containing 50 wt.% and 60 wt.% EL-NCF denote the presence of redox peaks with the 60 wt.% EL-NCF/G achieving the highest current density of \sim 0.10 mA cm⁻², while the 67 wt.% EL-NCF/G shows a purely capacitive current. This indicates the absence of Li $^+$ intercalation. Similarly to the previous NCF/graphite electrode system, Li $^+$ intercalation reaction into graphite corresponds to the cathodic redox peaks shown at \sim 0.35 V vs. Ag|AgCl, whereas Li $^+$ deintercalation is attributed to the anodic \sim 0.5 V vs. Ag|AgCl peaks. Compared to the NCF-containing counterparts where the 70 wt.% NCF/G electrode was considered the upper content for electrode functionality, here the high nanocellulose content where the electrode is functional, is shifted to a lower content of 67 wt.% EL-NCF/G. Possibly, the EL-NCF fibres create more resistance at lower concentration, due to their different size, shape and structural interactions with graphite particles.

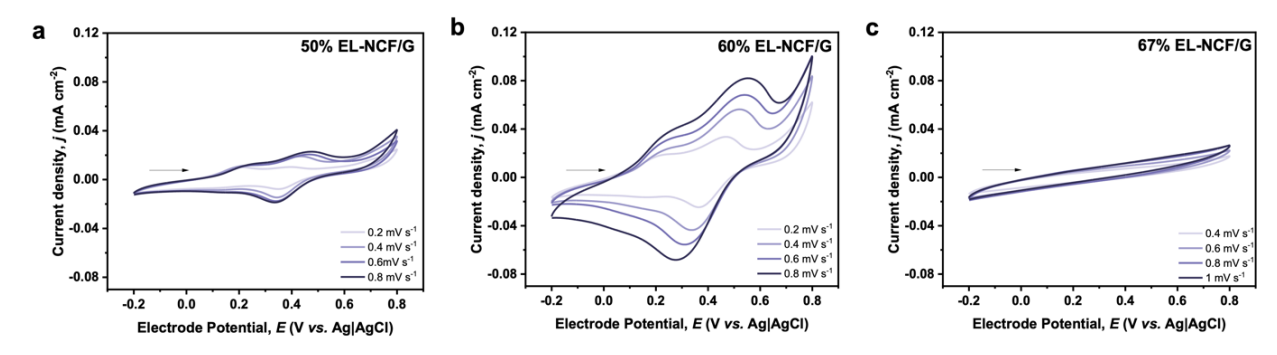


Figure 5.3 Variable-rate CV curves from experiments performed in a three-electrode cell assembled with glassy carbon counter electrode ($A = 0.38 \, \mathrm{cm^2}$) vs. Ag|AgCl reference, at scan rates varying from 0.8 mV s⁻¹ to 0.2 mV s⁻¹, for electrodes containing a) 50 wt.%, b) 60 wt.% and c) 67 wt.% EL-NCF in composite EL-NCF/G electrodes. Each scan rate is shown for the 3rd cycle.

By performing the Dunn analysis, the current is deconvoluted to the relative charge storage contributions at a 0.6 mV s⁻¹ (Figure 5.4). The analysis is performed for the 50 wt.% and 60 wt.% EL-NCF/G electrodes, and no further treatment was performed for the 67 wt.% EL-NCF/G composition, due to the absence of redox peaks. Notably, a similar trend related to pseudocapacitive traits as a function of NCF content is observed in the case of EL-NCF, showing increased pseudocapacitive current and decreased diffusion limitations upon increasing the EL-NCF content from 50 wt.% to 60 wt.% EL-NCF. For the 50 wt.% EL-NCF/G electrode (Figure 5.4a) higher faradaic diffusion-limited contributions of 74% were noticed, but relatively lower pseudocapacitance at 10% compared to the 50 wt.% NCF counterpart.

Upon changing NCF to EL-NCF within the electrode, for a 60 wt.% EL-NCF content (Figure 5.4b) the Faradaic current undergoes a considerable increase from 26% to 57%, pseudocapacitive characteristics are slightly curtailed from 43% to 37%, while most importantly, true capacitive current contributions drop from 31% to 6%. The high capacitive current is now transformed into faradaic diffusion-limited current due to the EL-NCF higher surface area, providing more facile access of Li⁺ ions to the fibres and to the graphite particles compared to the continuous, compact structure of the NCF-containing counterpart. In particular, true capacitive current for the 60 wt.% EL-NCF/G electrode is minimised (2% at 0.2 mV s⁻¹) compared to 60 wt.% NCF/G (28% at 0.2 mV s⁻¹).

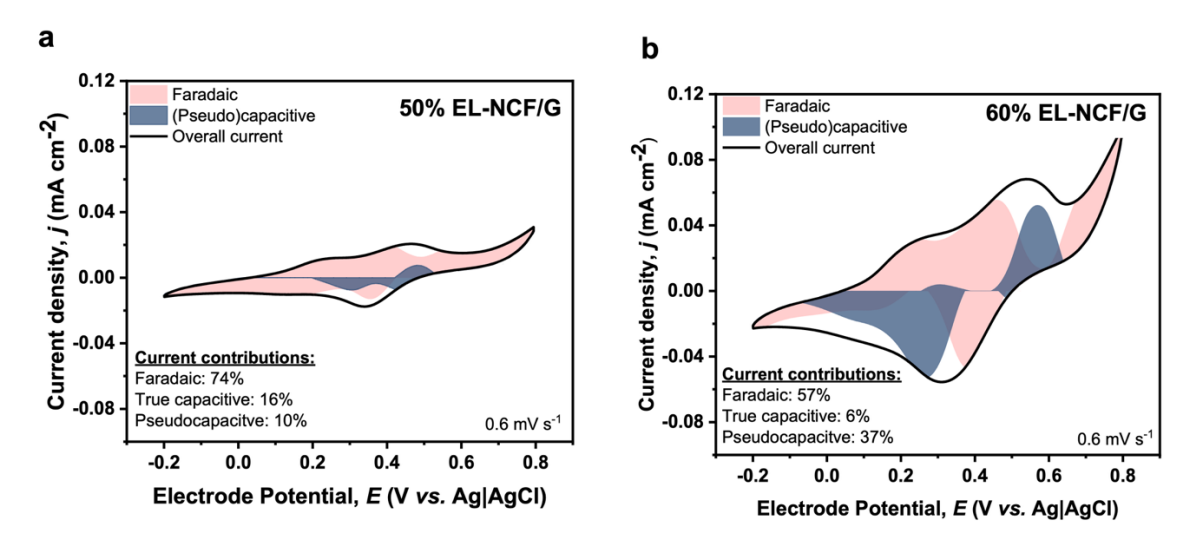


Figure 5.4 Deconvoluted cyclic voltammograms at 0.6 mV s⁻¹ demonstrating the relative faradaic, true capacitive and pseudocapacitive current contributions for a) 50 wt.% and b) 60 wt.% EL-NCF in composite EL-NCF/G electrodes. Each scan rate is shown for the 3rd cycle.

A comparison of the relative current contributions for the two electrodes (60 wt.% NCF/G versus 60 wt.% EL-NCF/G) at each scan rate is provided in Figure 5.5. It is pointed out, that the pseudocapacitive current for the 60 wt.% EL-NCF/G electrode (Figure 5.5b) becomes higher than the pseudocapacitive current of the 60 wt.% NCF/G electrode (Figure 5.5a) at the slowest (0.2 mV s⁻¹) scan rate. True capacitive current is minimised for the EL-NCF/G electrode.

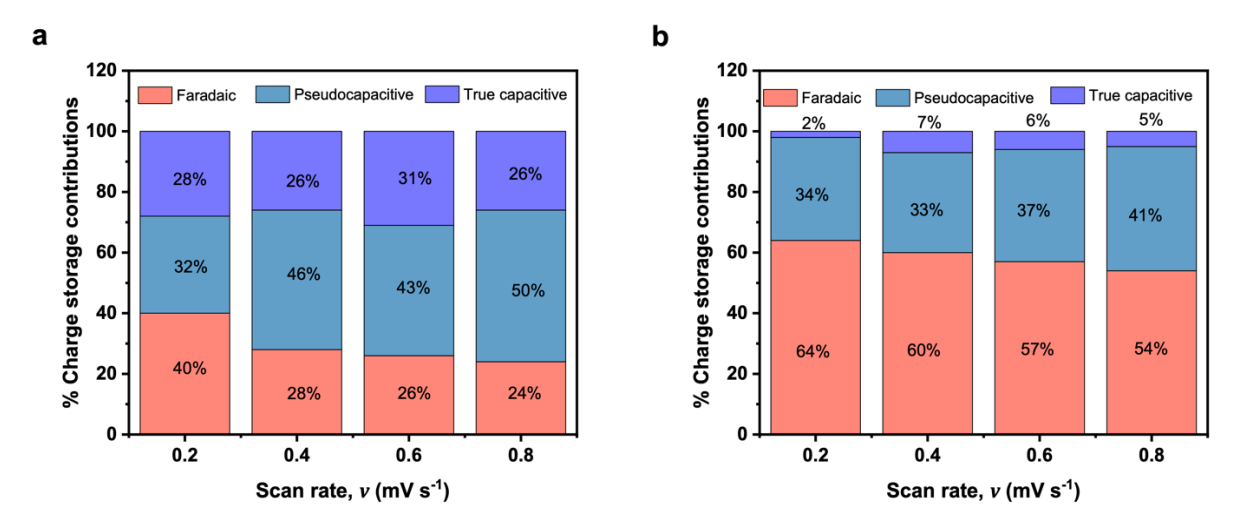


Figure 5.5 Bar charts showing the relative current distributions at each scan rate for the a) 60 wt.% NCF/G and b) 60 wt.% EL-NCF/G electrode compositions.

5.3 Evaluation of diffusion coefficients

Diffusion coefficients were evaluated for the two 50 wt.% and 60 wt.% EL-NCF/G electrode compositions using the Randles-Ševčík equation at T=25°C. The peak current i_{pc} of the cathodic reaction was plotted against the square root of the scan rate $v^{1/2}$, as described in Section 4.3.2

and seen here in Figure 5.6. The values show the effective diffusion coefficient that does not distinguish between the underlying charge storage mechanisms and are used as a qualitative tool.

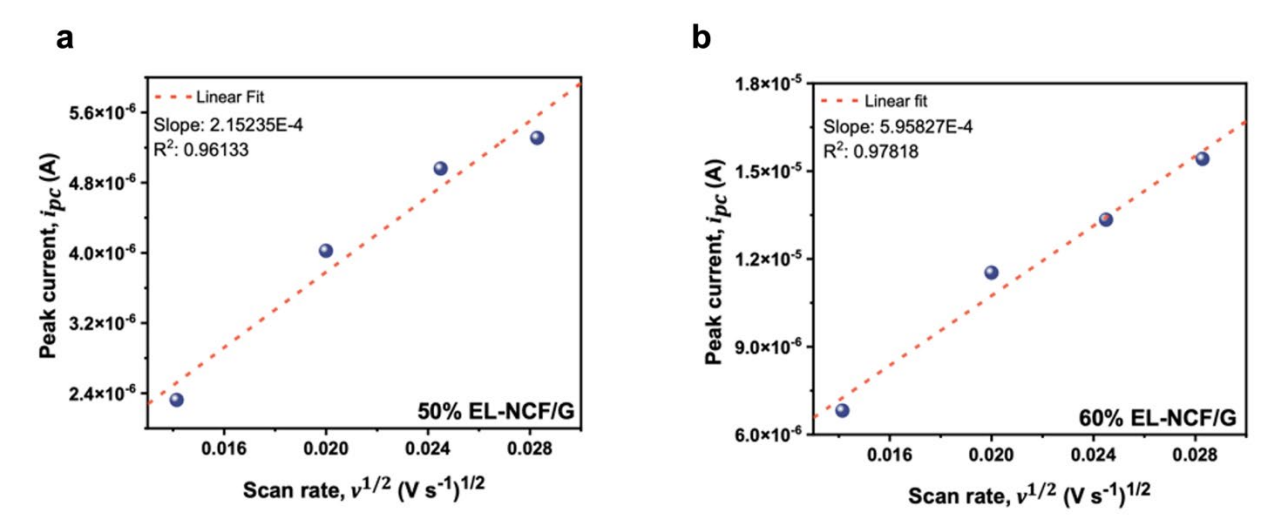


Figure 5.6 Cathodic peak current (i_{pc}) vs. scan rate ($v^{1/2}$) plots. Linear fitting was applied for slope calculation and subsequently diffusion coefficient evaluation via the Randles-Ševčík equation. Analysis is performed for samples containing a) 50 wt.% and b) 60 wt.% ELNCF in composite EL-NCF/G electrodes.

The calculated diffusion coefficient values appear to be lower than their non-modified nanocellulose NCF counterparts (Figure 5.7) and were specifically evaluated at $6 \times 10^{-10} \, \text{cm}^2 \, \text{s}^{-1}$ for 50 wt.% EL-NCF/G, and $5.88 \times 10^{-9} \, \text{cm}^2 \, \text{s}^{-1}$ for the 60 wt.% EL-NCF/G compositions. The highest diffusion coefficient was evaluated for the 60 wt.% EL-NCF/G, which also exhibited the lowest diffusion limitations from the variable-rate CV analysis (Figure 5.4b) supporting the improved ion mobility properties. The value remains lower however than the diffusion coefficient determined for 60 wt.% NCF/G, at $1.22 \times 10^{-8} \, \text{cm}^2 \, \text{s}^{-1}$, which is also consistent with the decreased pseudocapacitive characteristics of the 60 wt.% EL-NCF/G (Figure 5.4b).

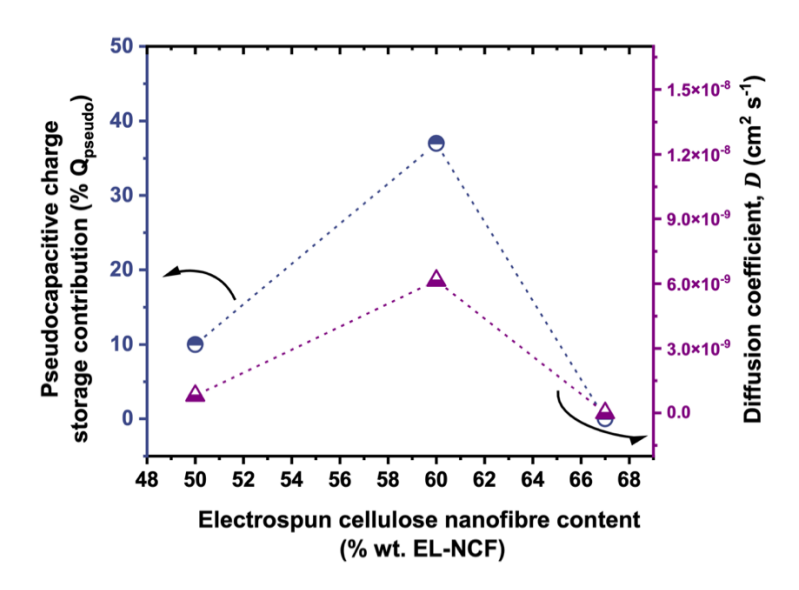


Figure 5.7 Diffusion coefficients and relative proportion of pseudocapacitive contributions $(\%Q_{pseudo})$ as a function of electrospun cellulose nanofiber content (wt.% EL-NCF) for EL-NCF/G composite electrodes.

5.4 Evaluation of charge transfer resistance

5.4.1 Nyquist and Bode plots

In order to evaluate the R_{ct} value of the, overall best-performing, 60 wt.% EL-NCF/G electrode composition, EIS of the already assembled half-cell was performed at the open circuit potential after 20 CV cycles at 0.8 mV s⁻¹. The data are presented as Nyquist plots in Figure 5.8. The plot is comparing the two electrodes 60 wt.% EL-NCF/G and 60 wt.% NCF/G that have the same cellulosic content, but different architecture, as indicated by structural characterisation for 60 wt.% NCF/G (Figure 4.1c) and 60 wt.% EL-NCF/G (Figure 5.2). We focus on a frequency region of 500 kHz–15 Hz of the Nyquist plots, whereby the diameter of the semicircle the R_{ct} value is calculated.

EIS Nyquist spectra at the high frequency region for the two compositions, demonstrate a smaller R_{ct} of 107 Ohm for the 60 wt.% EL-NCF/G compared to the R_{ct} of 248 Ohm of the 60% wt.% NCF/G structure, meaning that charge transport is less hindered within the EL-NCF. This difference could be possibly owed to improved contact with graphite, or to different structure of graphite particles in the electrospun matrix in terms of c-spacing, tortuosity and porosity [164]. Overall, though, both NCF and EL-NCF-based electrodes show an increase in pseudocapacitive current with increasing content in the graphite composite electrode. The ohmic resistance R_{Ω} , is also evaluated at 13 Ohms. The data are additionally fit with the same equivalent circuit mentioned for the 60 wt.% NCF/G electrode, described by a resistor (R1), a parallel circuit of (R2/Q2), and a (R3 + W3/Q3) element, and is shown in Figure 4.11.

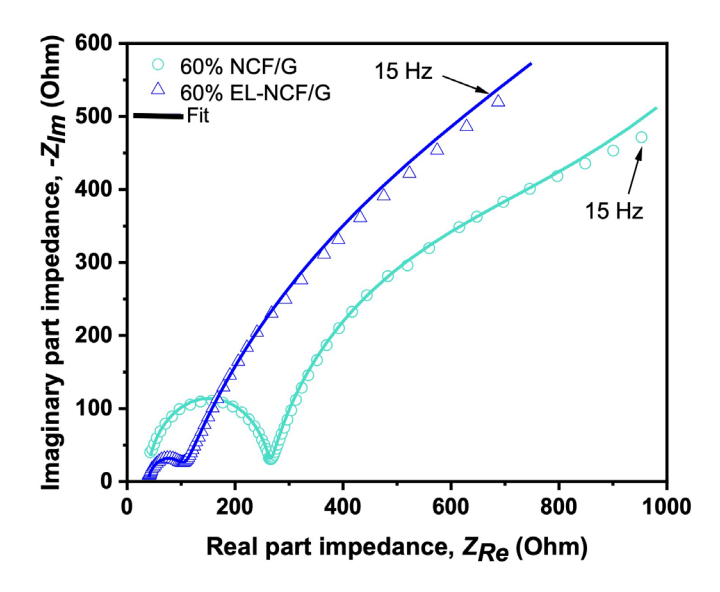


Figure 5.8 Electrochemical impedance spectra shown as Nyquist plot of the imaginary $(-Z_{Im})$ vs. real (Z_{Re}) part of impedance. The frequency region of 500 kHz to 15 Hz is shown, for 60 wt.% NCF/G and 60 wt.% EL-NCF/G electrodes.

The corresponding, comparative Bode plots are shown in Figure 5.9, demonstrating how the phase angle and the absolute value of the impedance logarithm trend in relation to frequency. The 60 wt.% EL-NCF/G content electrode exhibits lower impedance Z in high frequency region, but comparable in the mid and lower frequency region (Figure 5.9a). The phase angle is more deviated from the 45° diffusion-limited behaviour in the case of 60 wt.% NCF/G at the lower frequency region, which agrees with the highest pseudocapacitive characteristics (Figure 5.9b).

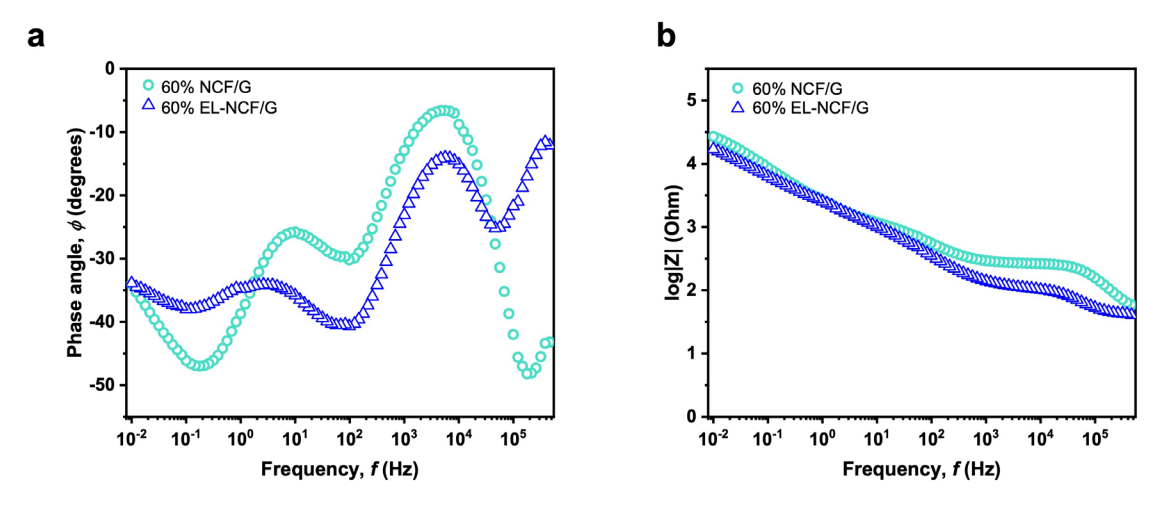


Figure 5.9 Comparative Bode plots for the 60 wt.% EL-NCF/G and 60 wt.% NCF/G electrodes assessed in half-cells with glassy carbon counter electrode ($A = 0.38 \text{ cm}^2$) vs. Ag|AgCl, showing a) phase angle as a function of frequency, b) $\log |Z|$ as a function of frequency.

5.5 Chapter overview

In this chapter, the effect of nanocellulose architecture modification on the charge storage mechanisms of nanocellulose/graphite electrodes, was highlighted. Three electrode compositions with variable electrospun cellulose nanofiber (EL-NCF) content ranging from 50 wt.% to 67 wt.% EL-NCF content, were chosen and assessed in Li⁺ environment half-cells. Variable-rate CV experiments showed the highest current density of 0.10 mA cm⁻² and at 0.8 mV s⁻¹ was achieved consistently by the 60 wt.% EL-NCF/G composition. At the same time, the 67 wt.% EL-NCF/G sample demonstrated exclusively capacitive behaviour with a current density comparable to the electrolyte background. This showed that no intercalation reaction can be facilitated in the 67% EL-NCF/G electrode, contrary to the 67 wt.% NCF/G electrode. This can be explained due to the important structural differences between the two electrodes, including porosity, and random EL-NCF fibre distribution, as seen from SEM imaging. From a further Dunn analysis, the total current was deconvoluted into the respective faradaic diffusion-limited, capacitive and pseudocapacitive contributions. EL-NCF still contributes to improved pseudocapacitive characteristics with increasing cellulosic content from 50 wt.% to 60 wt.%, peaking at 60 wt.% EL-NCF content with 37% charge contribution. The contribution is slightly lower than the 60 wt.% NCF/G counterparts, however, the capacitive current underwent a massive drop from 31% to 6%. The faradaic diffusion-limited current increased from 26% to 57%. These phenomena are possibly owed to the higher EL-NCF surface area and improved contact with graphite, yielding higher faradaic diffusion-limited and lower capacitive current proportions. The random distribution of the EL-NCF fibres though, might pose discrepancies to ion diffusion compared to the NCF-based counterpart, leading to slightly lower pseudocapacitive current. Nevertheless, pseudocapacitive contributions are still considered high within the EL-NCF composition.

Diffusion coefficient values for the cathodic reaction were also determined as a qualitative tool by using the Randles-Ševčík equation and appear to follow the same trend as pseudocapacitive percentages in correlation to EL-NCF content with the maximum being 5.88×10^{-9} cm² s⁻¹ for 60 wt.% EL-NCF content. It remains lower than the 60 wt.% EL-NCF counterpart at 11.22×10^{-8} cm² s⁻¹, consistent with the lower pseudocapacitive characteristics.

EIS data liaise with aforementioned trend, showing a reduction in charge transfer resistance equal to 120 Ohm upon electrode architecture alteration.

Chapter 6 Nanocellulose in the Aluminium-graphite battery

This chapter investigates flexible graphite/NCF electrodes in beyond Li-ion chemistry, specifically the Al-graphite chemistry with chloroaluminate ionic liquid electrolyte. Current deconvolution using variable-rate CV is used as a tool to shed light on the correlation of NCF content and pseudocapacitive characteristics during charge storage. Full cells are also assessed by using galvanostatic cycling. The flexibility of NCF/G electrodes in full cells is investigated by implementing EIS on an assembled pouch cell. Finally, the NCF/G electrodes are employed as a substrate for the electrochemical sol-gel deposition of an organosilane layer, for the fabrication of covalently bonded electrode-electrolyte interface.

6.1 Examination of the role of nanocellulose in the charge transport and intercalation of chloroaluminate ions into graphite

6.1.1 Current deconvolution

Three NCF/G compositions containing an increasing amount of NCF (50, 60 and 67 wt.%) are implemented as the positive electrode and examined in full cells with an Al-foil negative electrode, within and Lewis acidic chloroaluminate ionic liquid electrolyte, EMImCl-AlCl₃ (r = 1.5). NCF percentage in the graphite electrode was increased in a similar way to Chapter 4 and Chapter 5.

Variable-rate cyclic voltammetry was performed using the as-assembled full cells, at a scan rate from 1 mV s⁻¹ to 0.4 mV s⁻¹. Slow scan rates were employed as graphite ion intercalation is considered a slow process. For each scan rate, the 7th CV cycle is shown, unless stated otherwise. The cells are scanned at a potential window from 0.5 V to 2.4 V which is the electrochemical stability window of EMImCl-AlCl₃ in Al-graphite cells, as verified from previous studies. The upper potential limit is bound by oxidation of the chloroaluminate anion, while beyond the lower cathodic limit, the EMIm⁺ cation is reduced to EMIm• radicals. Furthermore, while electrolyte degradation usually happens beyond 2.45 V based on previous studies for Algraphite batteries using ionic liquid electrolytes, parasitic side reactions might even happen at lower potentials, involving both electrolyte decomposition as well as graphite chlorination reactions. This phenomenon is owed to presence of defects within the graphite layers, and at the edge sites; these sites act as catalytic centres that foster reactions like graphite chlorination, leading to the formation of C-Cl bonds on those graphite domains. [42, 150]

Upon charging the aluminium-graphite battery, AlCl₄ anions from the ionic liquid electrolyte undergo intercalation into graphite, as described by the Equation (2-3).

The resulting CVs shown in in **Figure 6.1**, demonstrate anodic peaks observed from 1.8 V to 2.4 V which are allocated to chloroaluminate ion intercalation. The reverse scan shows cathodic peaks onset from 2.2 V to 1.6 V which are attributed to the reverse, chloroaluminate ion deintercalation from graphite. Multiple peaks are observed in both cases, characteristic of the staging ion intercalation mechanism into the graphite interlayers.

The highest current density with a value of 2.4 mA cm⁻² at 1 mV s⁻¹ is exhibited for the 50 wt.% NCF/G electrode (Figure 6.1a). Further increase to the NCF content up to 60 wt.% (Figure 6.1b) leads to slightly lower current density at 1.5 mA cm⁻², comparative to the current density of the 67 wt.% composition (Figure 6.1c). This is owed to the increase of resistance at higher NCF percentages.

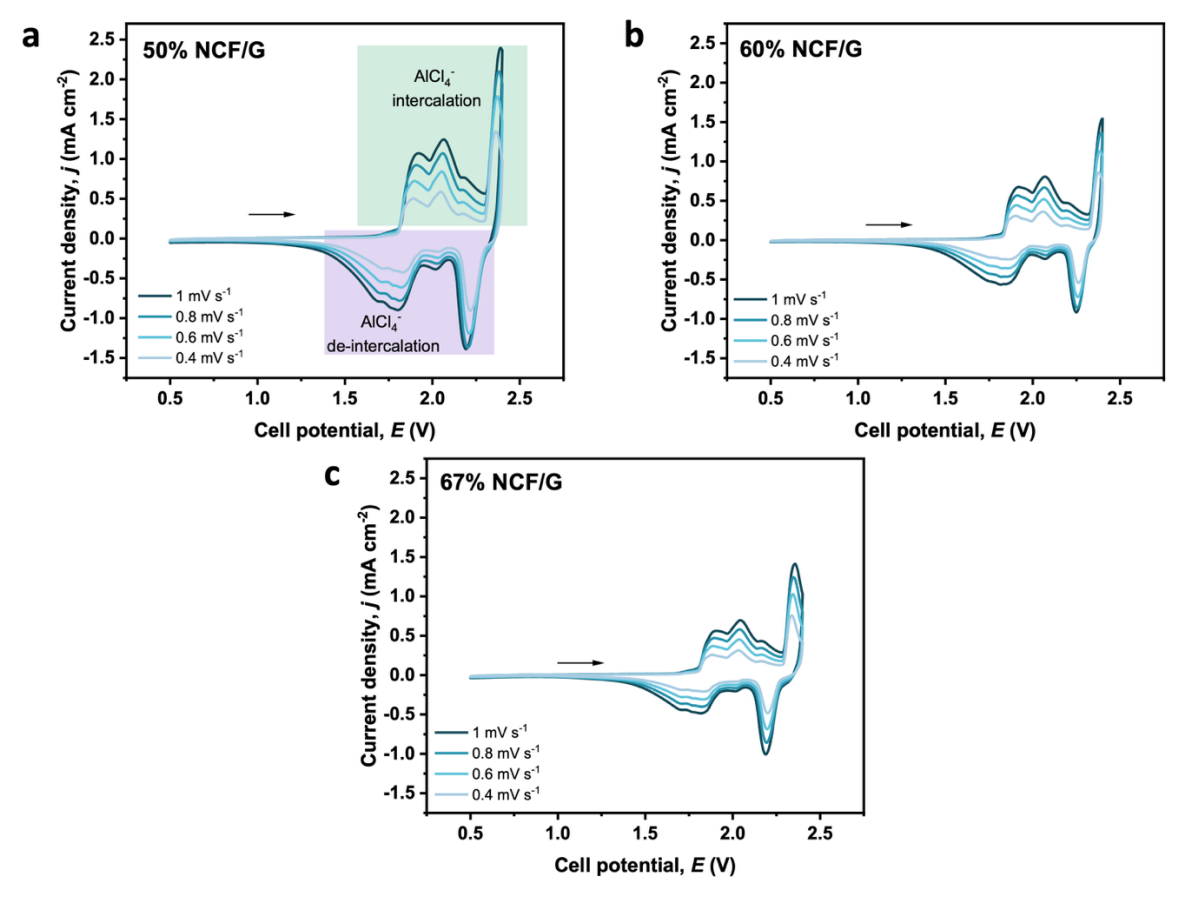


Figure 6.1 Variable-rate CV curves performed in a two-electrode cell, with an NCF/G positive electrode ($A = 0.28 \text{ cm}^2$), and an Al metal negative electrode ($A = 0.28 \text{ cm}^2$), at scan rates varying from 1 mV s⁻¹ to 0.4 mV s⁻¹. CV curves are shown for NCF/G electrodes containing a) 50, b) 60, and c) 67 and e) 70 wt.% NCF. Each scan rate is shown for the 7th cycle.

Generally, AlCl₄ intercalation into graphite is considered a faradaic charge storage process, that exhibits both diffusion-limited and non-diffusion-limited (pseudocapacitive) behaviour.[164] Therefore, adding nanocellulose would theoretically further reinforce the pseudocapacitive characteristics and promote lower diffusion limitations within the bulk of the NCF/G electrode. The relative current proportions of faradaic, capacitive and pseudocapacitive current are hence quantified using the "Dunn method" as described in Section 2.4.2. The resulting deconvoluted CVs (Figure 6.2) are shown at an intermediate scan rate of 0.8 mV s⁻¹.

In agreement with the studies performed in Chapter 4 and Chapter 5, it is obvious that by increasing NCF content from 50 wt.% to 60 wt.%, the pseudocapacitive current proportion increases accordingly by almost 10%. Further addition of NCF yielding a 67 wt.% composition, leads to another slight increase of pseudocapacitance from 70% to 72%. The faradaic diffusion-limited current on the other hand, seems to follow a reverse trend, manifesting a decrease in the presence of higher cellulose content. In the case of 50 wt.% and 60 wt.% electrodes, faradaic diffusion-limited charge proportion decreases from 37% to 24%. NCF addition lowers diffusion limitations, and the faradaic diffusion-limited current is converted to pseudocapacitive current contributions, which is still faradaic in nature, but non-diffusion limited. This addition also explains the minimal increase of capacitive current, as the NCF high surface area yields charge accumulation on its surface. As a result, the faradaic diffusion-limited current is redistributed and converted to pseudocapacitive and capacitive current when increasing NCF content from 50 wt.% to 60 wt.%.

To be more specific, in the case of 50 wt.% NCF/G (Figure 6.2a), AlCl₄⁻ intercalation at 1.8 V, and 2.2 V happens in a mixed pseudocapacitive and faradaic diffusion-limited regime, contrary to the 2.4 V peak where the mechanism is faradaic dominated. For the reverse reaction, anion deintercalation occurs in a mixed regime as well. At a 60 wt.% NCF content (Figure 6.2b), pseudocapacitive characteristics become more dominant in all cases, except for the 2.4 V–2.2 V redox pair. Interestingly, at a 67 wt.% NCF (Figure 6.2c), this redox pair now operates in a mixed regime, as pseudocapacitive contributions preside. In Figure 6.3, the overall trend correlating NCF content to pseudocapacitive charge storage contributions is depicted.

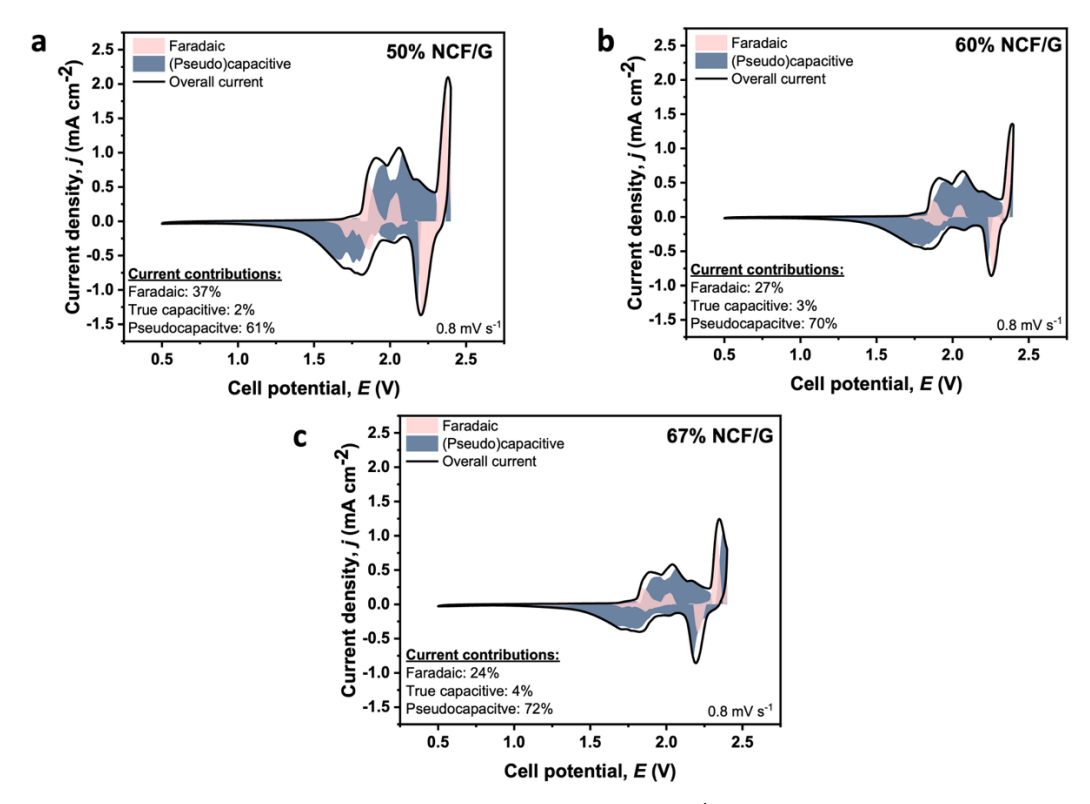


Figure 6.2 Deconvoluted cyclic voltammograms at 0.8 mV s⁻¹ demonstrating the relative faradaic diffusion-limited (light red area), and (pseudo)capacitive current contributions (blue area) for a) 50, b) 60 and c) 67 wt.% NCF in composite NCF/G electrodes. (Pseudo)capacitive current is deconvoluted to true capacitive and pseudocapacitive contributions, as described by the respective percentages. Each scan rate is shown for the 7th cycle.

Pseudocapacitive characteristics increase upon NCF content increase, due to the existence of more, and shorter pathways available for chloroaluminate diffusion through the nanochannels. As a result, the chloroaluminate anions are absorbed by NCF and are further transported to the bulk graphite active material, where intercalation takes place. This study proves the versatility of NCF as a material that improves ion mass transport properties in various battery chemistries.

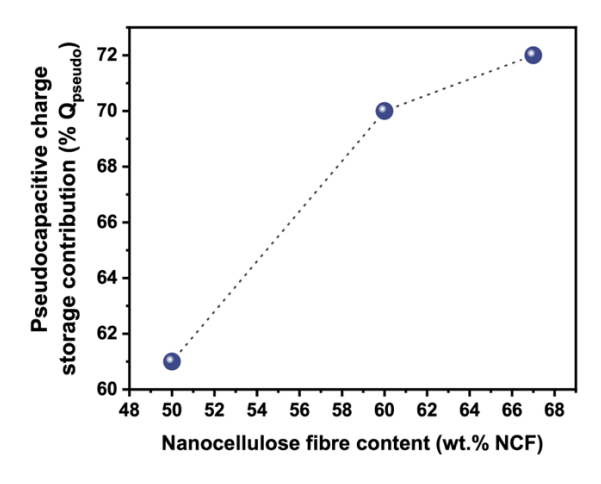


Figure 6.3 Relative proportion of pseudocapacitive charge storage contributions ($\%Q_{pseudo}$) as a function of NCF content (wt.% NCF) for NCF/G composite electrodes in Al-graphite cells.

6.1.2 Comparison of diffusion coefficients

The variable-rate CVs of the NCF/G electrodes that exhibited the highest pseudocapacitive contributions (60 wt.% and 67 wt.%) were further used to determine the diffusion coefficients of the AlCl₄-anion ion by using the Randles-Ševčík equation at 25°C and as described in Section 4.3.2. The values within the equation include the peak current i_p , the number of transferred electrons n which here is equal to 3, the electrode area A (0.28 cm²), the diffusion coefficient D, the scan rate v, and the bulk concentration C of $AlCl_4$ - for a Lewis acidity of r = 1.5. The latter is calculated at 0.0038 mol cm⁻³, based on previous studies and in correlation to the ionic liquid EMImCl-AlCl₃ (r = 1.5) composition. It should be noted that the Randles-Ševčík equation is used to calculate diffusion coefficient values for qualitative comparison purposes. Consequently, variations are expected to emerge if compared to already known literature values.

The diffusion coefficients were calculated for both 60 wt.% and 67 wt.% NCF/G compositions and for the 2.4 V/2.2 V redox pair where the peaks are marked as P3A and P1C, respectively. Despite being in a full cell, the redox pair is dominated by the intercalation and deintercalation reactions of $AlCl_4$ into graphite. Previous studies on the Al-graphite system have established that three-electrode and two-electrode cell CVs do not present major differences [164]. The results are shown in Figure 6.4.

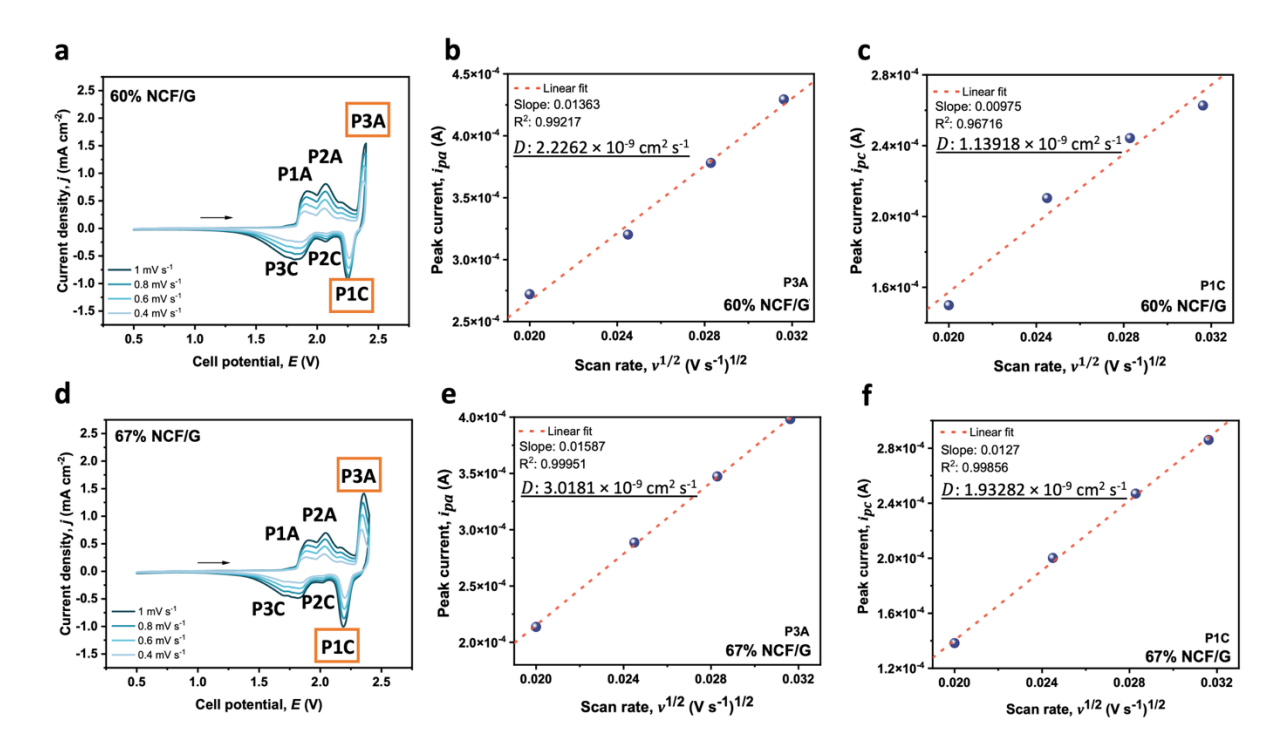


Figure 6.4 a) CV curve of 60 wt.% NCF/G showing the redox peak pair of the anodic P3A and cathodic P1C peaks of interest. b) Anodic peak P3A current (i_{pa}) vs. scan rate $(v^{1/2})$ plot. c) Cathodic peak P1C current (i_{pc}) vs. scan rate $(v^{1/2})$ plot. d) CV curve of 67 wt.% NCF showing the redox peak pair of the anodic P3A and cathodic P1C peaks of interest. e) Anodic peak P3A current (i_{pa}) vs. scan rate $(v^{1/2})$ plot. f) Cathodic peak P1C current (i_{pc}) vs. scan rate $(v^{1/2})$ plot. Linear fitting was applied for slope calculation and subsequently diffusion coefficient evaluation via the Randles-Ševčík equation.

The determined diffusion coefficient values follow a similar trend as the pseudocapacitive current contributions, increasing with increasing wt.% NCF. The highest diffusion coefficients were evaluated for the 67 wt.% NCF/G electrode at 3.18×10^{-9} cm² s⁻¹ for peak P3A (chloroaluminate anion intercalation) and 1.93×10^{-9} cm² s⁻¹ for peak P1C (chloroaluminate anion deintercalation). The electrode demonstrated the lowest diffusion limitations based on the Dunn analysis, which supports the excel ion mobility properties.

6.2 Galvanostatic charge-discharge of aluminiumgraphite/nanocellulose cells

To gain further insight into the galvanostatic charge-discharge profile of the 67 wt.% NCF/G electrode, which overall demonstrated the highest pseudocapacitive contributions, an aluminium-graphite/67 wt.% NCF cell containing EMImCl-AlCl₄ (r = 1.5) was assembled and studied. Galvanostatic cycling tests were performed at charge-discharge rates ranging from

5 mA g⁻¹ to 100 mA g⁻¹ and at an upper cut-off potential of 2.4 V. The resulting galvanostatic cycling curves for the 4th cycle are shown in Figure 6.5a while, Figure 6.5b correlates the specific capacities, with coulombic efficiencies and cycle number.

Chloroaluminate anion intercalation starts at 1.8 V, and the specific capacity of the cell peaks at 64 mAh g⁻¹ at 5 mA g⁻¹, which is lower than values reported in literature for synthetic graphite in similar systems. However, NCF content is much higher compared to literature, so this would justify the lower specific capacity. The graphite staging phenomenon is also apparent from the plateaus during charge and dicharge, which correspond to the different stages of the chloroaluminate intercalation and deintercalation into graphite, respectively. At lower discharge rates, plateaus are more prominent compared to the ones at higher charge rates where a steeper decrease is apparent, owed to the higher ohmic resistance. At faster rates, the timeframe for chloroaluminate anion intercalation and deintercalation is not sufficient, compared to slower rates. At very high rates, ions rather accumulate at the graphite surface instead of partcipating at the intercalation redox reaction in the electrode bulk. That is demonstrated as the lowest charge rates yielded the maximum specific capacity.

An initial decline in coulombic efficiency is observed though with regard to the first few cycles, which is foreseen because of graphite conditioning. During this phenomenon anion trapping takes place initially at the graphite intercalation sites, causing graphite structural reorientation and expansion. As a result, more intercalation sites are then created, and the Coulombic efficiency is increased. Faster charge rates also show higher coulombic efficiencies owed to the introduction of kinetic factors that help in the suppression of side reactions. Also, the enhanced pseudocapacitive characteristics promote capacity retention even at relatively higher charge rates.

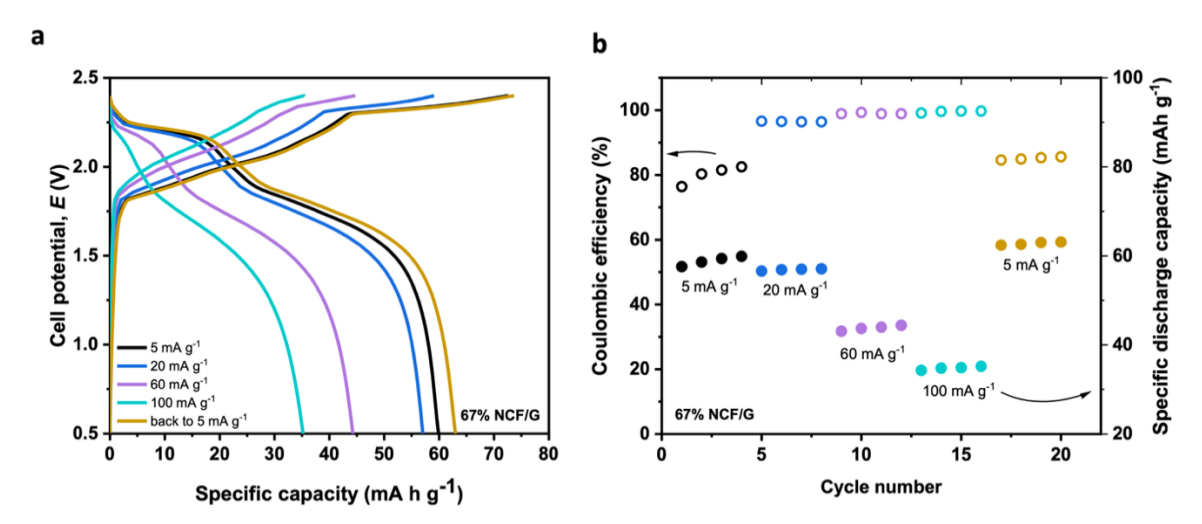


Figure 6.5 a) Galvanostatic charge-discharge curves of an Al-graphite/67 wt.% NCF cell with Lewis acidic EMImCl-AlCl₃ electrolyte cycled at 5 mA g⁻¹ to 100 mA g⁻¹ to cut-off

Chapter 6

potential of 2.45 V. b) Coulombic efficiencies and specific discharge capacities of the Al-graphite/67 wt.% NCF cell at various cycling rates.

Another aluminium-graphite/60 wt.% NCF cell was then manufactured, and the charge-discharge profile was compared to the profile of the aluminium-graphite/67 wt.% NCF cell in order to identify variations related to the differences in pseudocapacitive characteristics. As previously discussed, 67 wt.% NCF exhibited higher pseudocapacitive charge storage attributes compared to the 60 wt.% NCF electrode. The comparative charge-discharge curves at 60 mA g⁻¹ and 100 mA g⁻¹ are shown in Figure 6.6a,c, while the differential capacity plots are demonstrated in Figure 6.6b,d. In the latter, the peaks correspond to the apparent plateaus in the charge-discharge curves. In all cases, the results are shown for the 4th cycle.

Additionally, according to Equation (2-3) and based on the results from Figure 6.5a, the number of carbon atoms n (C_n) from graphite, participating in the chloroaluminate anion intercalation reaction can be calculated. The mean calculated value for the specific discharge capacity is $\approx 50 \text{ mAh g}^{-1}$. By using Faraday's law (Equation 6-1) as described below, the number of carbon atoms n is evaluated:

Measured capacity (average) =
$$\frac{number\ of\ charge\ carriers\ imes\ F}{MW imes 3600}$$
 (6-1)
$$57\ mA\ h\ g^{-1} = 0.057\ A\ h\ g^{-1} = \frac{96485\ A\ s\ mol^{-1}}{12\ g\ mol^{-1} imes n imes 3600\ s\ h^{-1}}$$

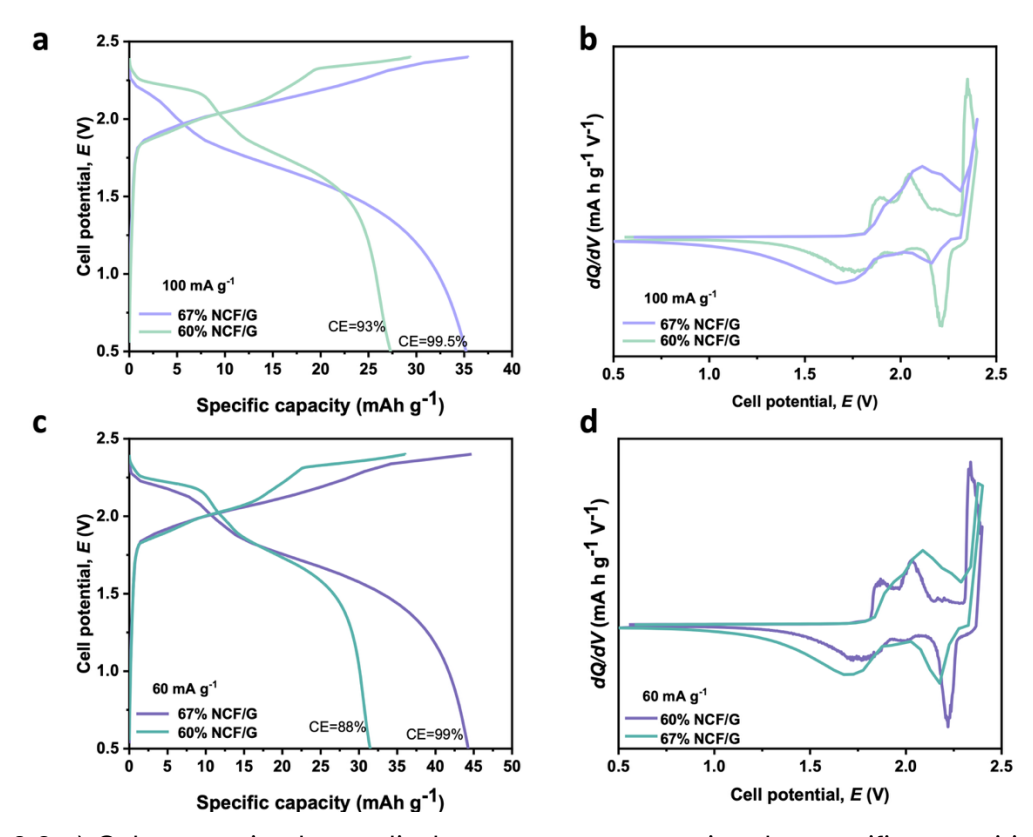


Figure 6.6 a) Galvanostatic charge-discharge curves comparing the specific capacities of Algraphite/NCF cells with 60 wt.% and 67 wt.% NCF in a Lewis acidic EMImCl-AlCl₃ electrolyte, cycled to a cut-off potential of 2.45 V at 100 mA g⁻¹, b) plots of differential capacity (dQ/dV) against cell potential at 100 mA g⁻¹. c) Galvanostatic charge-discharge curves comparing the specific capacities of Al-graphite/NCF cells of the same cell at 60 mA g⁻¹ and d) plots of differential capacity (dQ/dV) against cell potential at 60 mA g⁻¹.

The 67 wt.% NCF-based cell exhibited higher specific capacity at both charge rates, and specifically 44.9 mAh g⁻¹ at 60 mA g⁻¹ and with a coulombic efficiency of 99%, compared to a value of 32 mA h g⁻¹ and a an interestingly lower coulombic efficiency of 88% for the 60 wt.% NCF electrode. Nanocellulose acts as a sponge, thus absorption of higher amounts of ionic liquid electrolyte would lead to higher ion availability for charge storage, resulting in improved specific capacity. The results are also consistent with the variable-rate CV analysis and the calculated diffusion coefficients. The higher diffusion coefficient attributed to the 67 wt.% NCF compositions, leads to higher improved ion mobility and at the same time ion availability. Hence, at the same charge rate, there are differences in the ion availability which might lead to variations in the specific capacity.

The corresponding dQ/dV plots show broader and slightly shifted peaks for the 67 wt.% NCF electrode, which proves graphite structural differences between the two electrodes during intercalation and de-intercalation.

6.3 Flexible aluminium-graphite/nanocellulose pouch cell assessment

To demonstrate the flexible character of the NCF/G electrodes in full Al-battery cells, a bendable pouch cell based on 60 wt.% NCF/G positive electrode, Al foil negative electrode, a glass fibre separator and EMImCl-AlCl₄ ionic liquid electrolyte, was fabricated. The EIS spectrum was initially recorded for the pouch cell in the non-bent, flat state, at the OCP. The cell was then bent on a curved Falcon tube cylindrical surface at a 114° bending angle, and the EIS spectrum was recorded at the bent state, at OCP. The results are shown as comparative Nyquist (Figure 6.7) and Bode (Figure 6.8) plots.

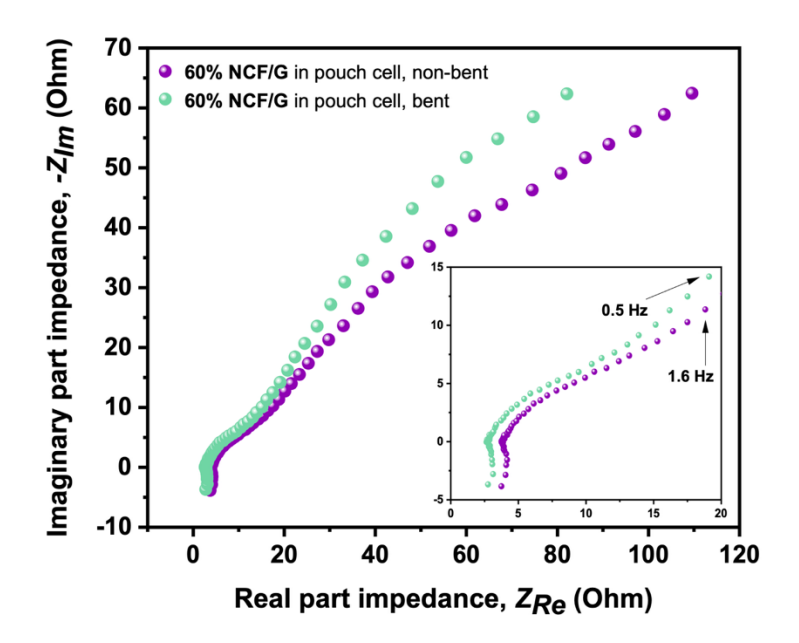


Figure 6.7 Electrochemical impedance spectra shown as Nyquist plot of the imaginary $(-Z_{Im})$ vs. real (Z_{Re}) part of impedance. The frequency region of 500 kHz–10 mHz is shown, for a flexible Al-graphite/NCF pouch cell composed of a positive 60 wt.% NCF/G electrode, a negative Al metal electrode, separated by a GF/D separator in a Lewis acidic chloroaluminate EMImCl-AlCl $_3$ ionic liquid. A flexible polypropylene pouch was implemented. Inset shows the impedance spectra at frequency region of 500 kHz–0.5 Hz.

The impedance spectrum shows a partial semicircle in the high-frequency region (500 kHz to 20 kHz), corresponding to the R_{ct} at the electrode-electrolyte interface. This is followed by a characteristic mass transport tail at the lower frequency region which is attributed to diffusion within the electrode. The R_{Ω} value which encompasses the internal resistance originating from all cell components can be calculated by the x-intercept at the high frequency region. The two values were calculated at the bent and non-bent state and the results are shown on Table 6-1 below.

Table 6-1 Charge transfer resistance and Ohmic resistance values at the non-vent and bent states of the flexible Al-graphite/NCF pouch cell.

Pouch cell state	R _{ct} /Ohm	$R_{\it \Omega}$ /Ohm
Non-bent	16.32	19.03
Bent	18.56	22.3

The flexibility of the pouch cell and the NCF/G electrode in the Al-battery is demonstrated, as the R_Ω undergoes only a slight increase of 16% upon transitioning from the non-bent to the bent state. The comparative Bode plots also show almost no variations for the total impedance between the two states, at the whole frequency region, (Figure 6.8b). This proves that the battery integrity can be sustained under induced stress.

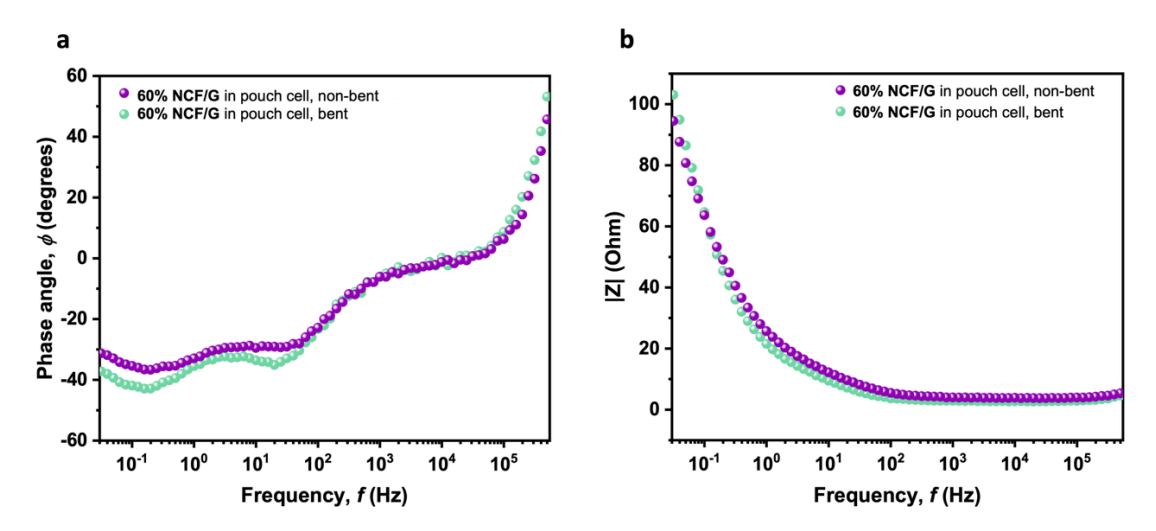


Figure 6.8 Comparative Bode plots showing a) the phase angle as a function of frequency, b) |Z| as a function of frequency, for a flexible Al-graphite/NCF pouch cell composed of a positive 60 wt.% NCF/G electrode, a negative Al metal electrode, separated by a GF/D separator in a Lewis acidic chloroaluminate EMImCl-AlCl $_3$ ionic liquid.

6.4 Electrochemical sol-gel deposition for the fabrication of covalently bonded electrode-electrolyte interfaces

Within the scope of battery flexibility, a covalently bonded electrode-electrolyte interface is synthesised. The electrode-electrolyte interface is one of the most important components that needs to be improved to achieve inherent flexibility of the battery. Upon mechanical deformation and bending, conventional interfaces tend to separate as they are hold together by

Van der Waals forces. Thus, resistances are introduced to the system due the rupture of the graphite layer. This discontinuity makes the flow of electrons more difficult. The aim is the creation of a unitized electrode/electrolyte interface that is covalently attached, which can be realised by the deposition of an intermediate sol-gel layer that will withhold the interface. Electrochemical sol-gel deposition on the contrary to chemical sol-gel deposition, is a technique that promoted the formation of homogeneous sol-gel layers with controllable thickness. Covalent bonds are stronger than van der Waals forces, so covalently-bound interfaces would not detach under flexion.

Electrodes containing 60 wt.% NCF/G are used as electrodes for the electrochemical sol-gel deposition from a TEOS-containing solution as described in Section 3.6. This is the first step of a two-step process, depositing the silanol-based gel layer. Then, the ionic liquid electrolyte is attached, at a second stage. Here, the first step only is attempted and investigated, as the process is intrinsically complex. Electrochemical sol-gel deposition on the 60 wt.% NCF/G electrode is initially performed by using chronoamperometry at –1.2 V vs. Ag|AgCl, for 10 min and 20 min (Figure 6.9).

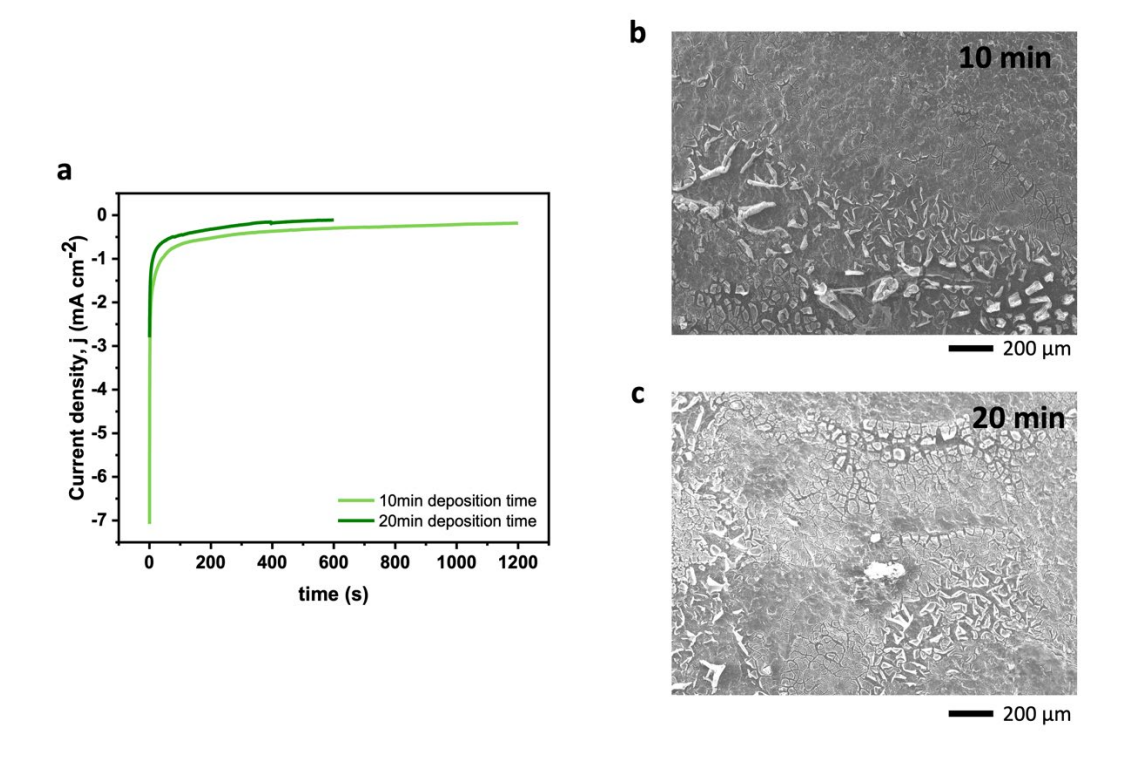


Figure 6.9 a) Chronoamperometry graph for electrochemical sol-gel deposition from a water/ethanol/TEOS/KCl/HCl solution, in a three-electrode cell using a 60 wt.% NCF/G working electrode ($A = 0.13 \text{ cm}^{-2}$), glassy carbon counter electrode ($A = 0.2 \text{ cm}^{-2}$), vs. Ag|AgCl and for a deposition time of b) 10 min and c) 20 min.

Deposition times were varied to explore the homogeneity of the sol-gel layer. From the SEM images in Figure 6.9b, morphological differences are clear, with the 20 min electrodeposited layer appearing thicker.

SEM integrated with EDX experiments were conducted on the pristine, the 10 min electrodeposited, and the 20 min electrodeposited 60 wt.% NCF/graphite electrodes. Figure 6.10 shows the results for the 60 wt.% NCF/G pristine electrode, which is mainly composed of carbon and oxygen rich areas.

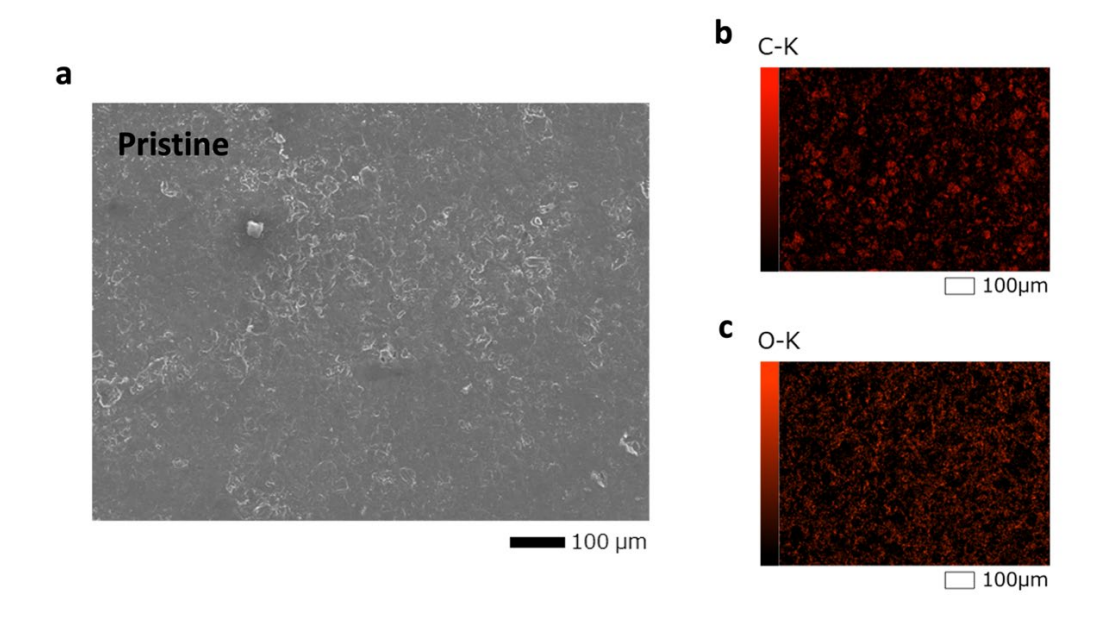


Figure 6.10 a) SEM image of the pristine 60 wt.% NCF/G. EDX images showing the distribution of b) carbon and c) oxygen atoms on the electrode surface.

Figure 6.11 shows the 60 wt.% NCF/G electrode that underwent 10 min deposition time, and it is observed that carbon-rich areas are now less as the NCF/G structure is covered by the sol-gel layer. Silicon and oxygen containing regions are also apparent, showing the patchy distribution of the sol-gel layer on the electrode surface.

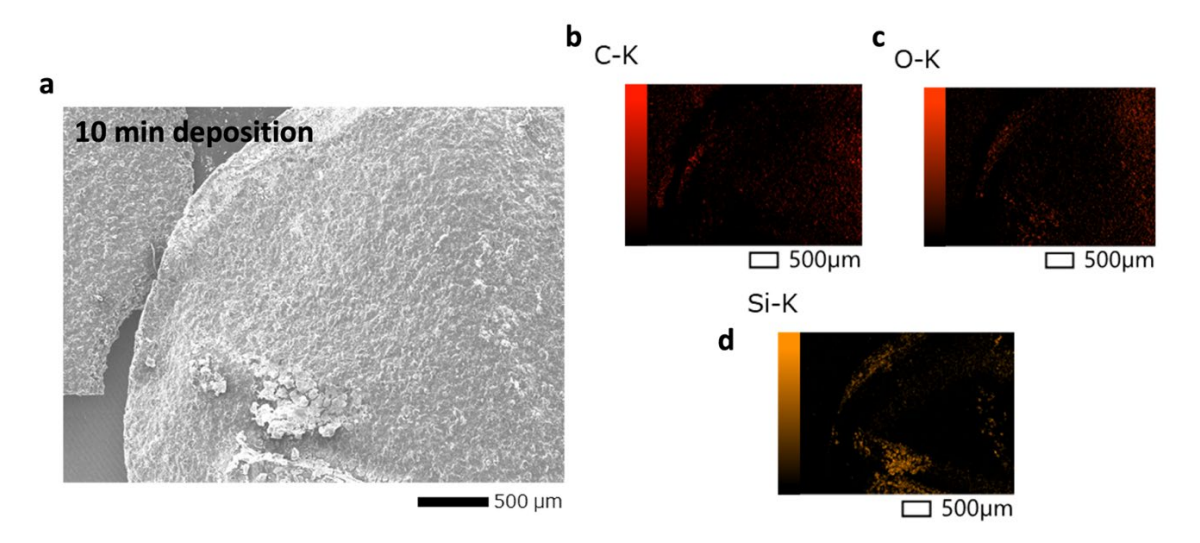


Figure 6.11 a) SEM image of a 60 wt.% NCF/G electrode after 10 min electrochemical sol-gel deposition time. EDX images showing the distribution of b) carbon, c) oxygen and d) silicon atoms on the electrode surface.

On the contrary and as seen in Figure 6.12, the 60 wt.% NCF/G electrode that underwent 20 min electrodeposition exhibits a more homogeneous and thicker sol-gel layer morphology, as seen from the SEM image and the EDX silicon and oxygen containing regions.

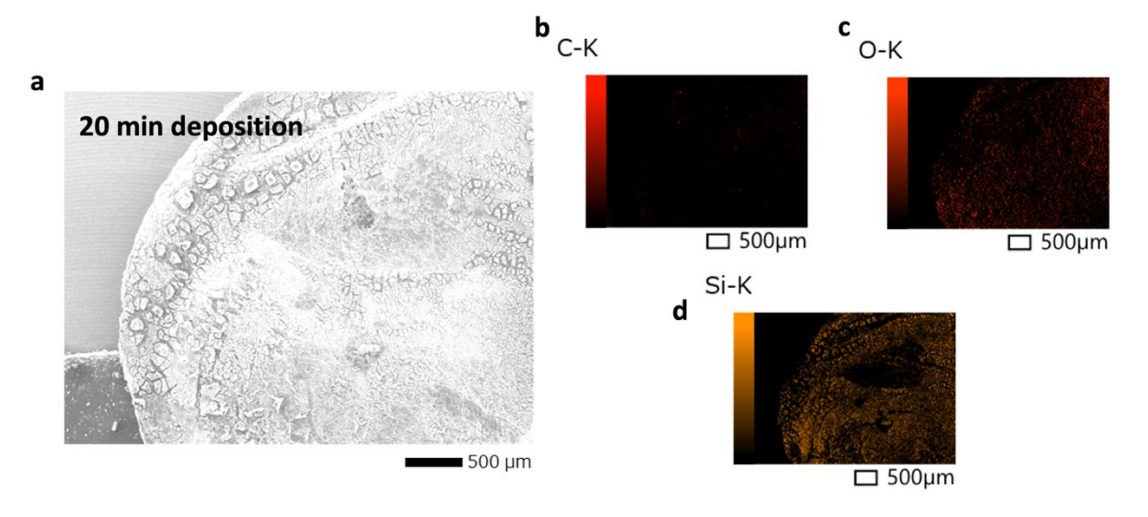


Figure 6.12 a) SEM image of a 60 wt.% NCF/G electrode after 20 min electrochemical sol-gel deposition time. EDX images showing the distribution of b) carbon, c) oxygen and d) silicon atoms on the electrode surface.

A zoomed region on the 20 min electrodeposited sample (Figure 6.13) shows a close-up of the sol-gel layer morphology that appears flake-like and lighter in colour, and the bottom electrode surface that is apparent by the darker shade. The electrodeposited flakes are clearly based on silicon (Figure 6.13d).

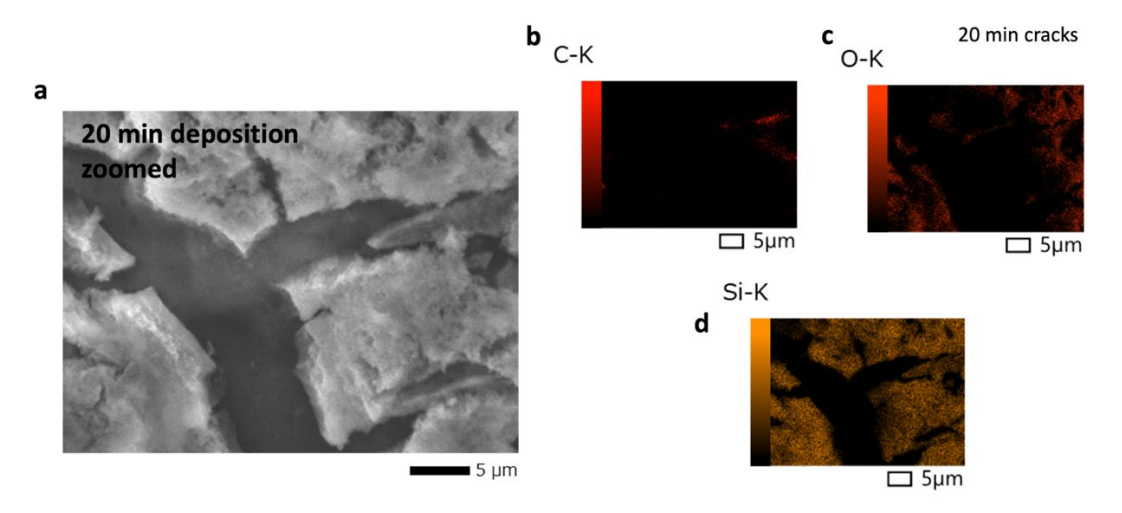


Figure 6.13 a) SEM image of a zoomed region on a 60 wt.% NCF/G electrode after 20 min electrochemical sol-gel deposition time. EDX images showing the distribution of b) carbon, c) oxygen and d) silicon atoms on the electrode surface.

As the goal is the generation of a sol-gel layer that evidenced by the presence of Si-O-Si bonds, the silicon to oxygen ratios were determined by the EDX for all the samples under examination and the results are shown in Table 6-2. The results concur to the formation of covalent Si-O-Si bonds rather than $Si-O_2$.

Table 6-2 Comparative Silicon to Oxygen mass ratio

Electrode	% Oxygen mass	%Silicon mass	O : Si ratio	
Pristine	37.5	-	-	
10 min electrodeposition	38.5	3.15	<1:2	
20 min electrodeposition	41.3	11.2	~1:2	

The sol-gel layer binding properties on nanocellulose were further investigated by performing FT-IR measurements on the pristine and 20 min electrodeposited 60 wt.% electrodes, and the resulting spectra are demonstrated in Figure 6.14. The peaks were assigned to the corresponding bond vibrations, and a summary is provided in Table 6-3.

Table 6-3 IR characteristic peak interpretation for a 60 wt.% NCF/graphite electrode that is pristine and after performing electrochemical sol-gel deposition.

Wavenumber/ cm ⁻¹ (Pristine electrode)	Bond	Wavenumber/ cm ⁻¹ (after electrochemical sol-gel deposition)	Bond	
3332	-OH (stretch)	3377	-OH (stretch)/S	
2876	-C-H (stretch)	2955	-C-H (stretch)	
1583	-COO- (asymm)	1732	-C=O	
1411	-COO- (symm)	1577	-COO- (asymm)	
1316	CH ₂ (bend)	1441	-COO- (symm)	
1099	-C-O (stretch, alc)	1163	-C-O (stretch, alc)	
1053	-C-O-C (stretch)	1033	-C-O-C (stretch)	
		940	Si-OH	
		798	Si-O-C	
		440	Si-O-Si	

By comparing the two spectra, the binding of the silicon-containing sol-gel layer on the pristine electrode is evident. Characteristic silicon peaks appear in the electrodeposited electrode sample, including Si-OH (940 cm⁻¹), Si-O-Si (440 cm⁻¹) and Si-O-C (798 cm⁻¹). The organosilane is also bound on the NCF surface hydroxyl groups, which is apparent from the intensity drop of the -OH peak intensity at 3329 cm⁻¹. Some of the organosilane is also bound on the NCF surface carboxymethyl groups, which is apparent by the appearance of a sharp peak at 1732 cm⁻¹, characteristic of the vibration of the carbonyl group. The intensity of characteristic peaks of the NCF backbone structure that appear from 1053 cm⁻¹ to 1583 cm⁻¹ are also decreased, indicating structural changes at the electrode and covalent binding of the sol-gel layer. The existence of these peaks shows that not all of the electrode surface is covered by the electrodeposited layer and there are inhomogeneities and space for further optimisation.[184-189]

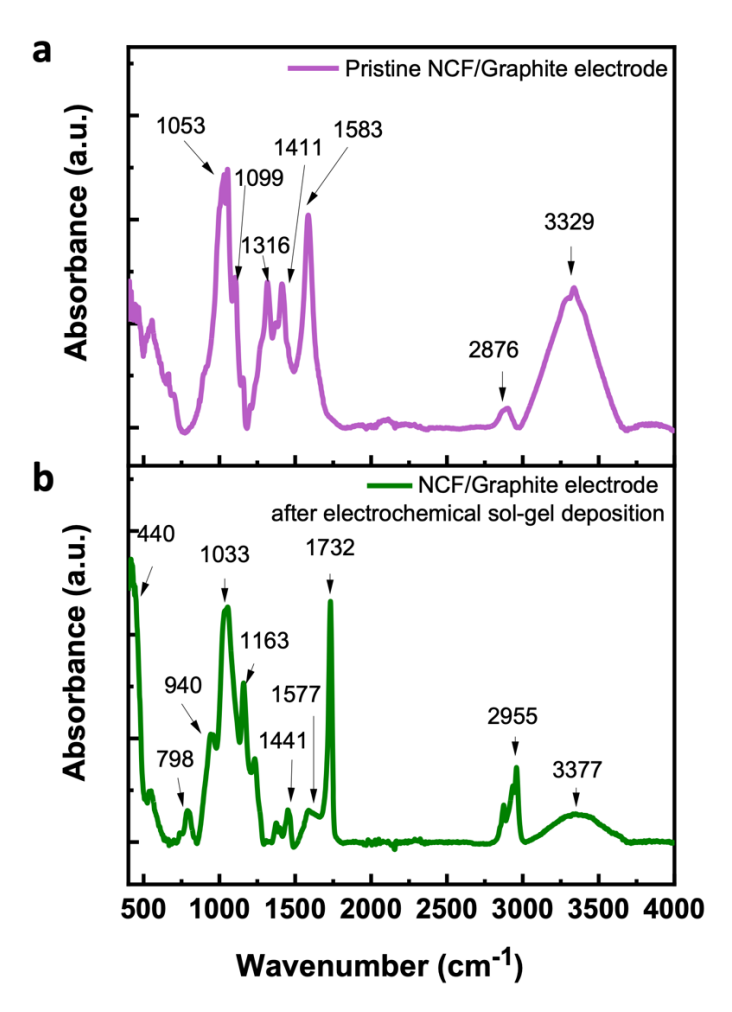


Figure 6.14 FT-IR spectra for a 60 wt.% NCF/G electrode a) after performing electrochemical solgel deposition, b) at the pristine state.

6.5 Chapter summary

In this chapter, three NCF/G electrode compositions with variable NCF content ranging from 50 wt.% to 67 wt.%, were assessed in Al-based battery cells. Variable-rate CV experiments and subsequent current deconvolution showed that increasing NCF content contributed to improved pseudocapacitive characteristics and ion mobility properties, as evidenced by the calculated diffusion coefficient values using the Randles-Ševčík equation. The highest pseudocapacitive charge storage was achieved for the 67 wt.% NCF/G electrode at 72% charge proportion. At the same time, it was observed that by increasing NCF content, the faradaic diffusion-limited current contribution is transformed to pseudocapacitive. As a result, chloroaluminate anion mass transport within the bulk of the electrode is improved.

Galvanostatic charge and discharge profiles of the 60 wt.% and 67 wt.% NCF/G electrode demonstrating the highest pseudocapacitive characteristics were acquired and compared. Graphite conditioning over the first few cycles is also manifested by the initial decline in coulombic efficiency due to ion trapping and further expansion of the graphitic structure for

Chapter 6

the creation of more intercalation sites. The 67 wt.% electrode specific capacity reached a maximum of 64 mAh g⁻¹ at 5 mA g⁻¹. Comparing the two compositions at faster charge rates, the 67 wt.% NCF-based cell showed a specific capacity of 44.9 mAh g⁻¹ at 60 mA g⁻¹ with a coulombic efficiency of 99%. The 60 wt.% NCF counterpart demonstrated a specific capacity of 32 mA h g⁻¹ at the same charge rate, and a an interestingly lower coulombic efficiency of 88%. This is consistent with the ion mobility and pseudocapacitive properties of the higher-NCF containing electrode, which absorbs higher amounts of ionic liquid electrolyte, leading to higher ion availability for charge storage and resulting in improved capacity.

Flexible pouch cells made of a 60 wt.% NCF/G positive electrode, Al foil negative electrode, a glass fibre separator and Lewis acidic EMImCl-AlCl $_4$ ionic liquid electrolyte, were assembled to show the mechanical flexibility properties of the NCF-based electrode in full Al-based cells. EIS spectra were recorded both at the non-bent and the bent state, and the results showed an acceptable increase of 16% for the R_{Ω} value upon bending the cell by 114°. Finally, within the same context of flexible batteries, electrochemical sol-gel deposition is implemented for the facilitation of a covalently bonded NCF/G electrode-electrolyte interface, that can withstand stress and not detach upon mechanical deformation. As a first step, a silanol-based gel layer is deposited and bound on the NCF surface functional groups electrode surface, as revealed by SEM/EDX and FT-IR experiments. Further optimisation of the process in terms of deposition time, sol-gel layer thickness and homogeneity are needed, as well as the subsequent immobilisation of the ionic liquid electrolyte to fabricate the covalently-bonded electrode-electrolyte interface

Chapter 7 Conclusions and Future Work

7.1 Conclusions

To date, flexible, safe and, ideally, recyclable batteries are required to power modern electronic devices like wearables. The propagation of current Li-ion flexible battery technologies has been limited, as the individual components are not entirely deformable. Here, nanocellulose is integrated with graphite, to produce intrinsically flexible NCF/G battery electrodes, that are also composed of abundant and safe materials. These electrodes are both tested in Li-ion environment and in aluminium-graphite batteries, with the latter being considered a safer alternative battery chemistry, especially for close-to-skin electronic applications. The NCF/G electrochemical and mechanical properties were thus studied.

The microstructure of five NCF/G electrode compositions containing increased amount of NCF was examined via SEM in Chapter 4. It was revealed that the lower NCF contents of 40 and 50 wt.% NCF exhibited a loosely bound graphite-NCF network. On the other hand, higher NCF content of 60 and 67 wt.%, demonstrated the formation of a continuous film on the surface of graphite particles. When an excess 70 wt.% NCF amount was used, NCF was the dominant electrode compartment, causing graphite particle separation. AFM images revealed the structure of NCF at the nanoscale, where it was highlighted that the NCF compact network as shown in the SEM images, in actually comprised of smaller, organised nanofibrils. The NCF/G electrode flexibility was evaluated by performing EIS at the non-bent electrode and under three different bending angles. Upon transitioning from the flat state to an extreme 180° bending angle without breaking, the electrode underwent negligible conductivity σ loss from 13.6 × 10⁻⁸ S cm⁻¹, to 9.01 × 10⁻⁸ S cm⁻¹.

The electrode morphology can be directly correlated with the electrochemical performance characteristics that were determined from variable-rate CV and EIS analysis in Chapter 4. The five electrode compositions with variable NCF content were assessed in Li $^+$ environment halfcells, in order to understand the role of nanocellulose in ion mass transport and charge storage mechanism. The focus was on the monitoring of pseudocapacitive charge storage contributions with increasing NCF content, as pseudocapacitive behaviour is associated with reduced ion diffusion limitations. The variable-rate CV experiments and subsequent current deconvolution analysis showed a clear trend of improved pseudocapacitive characteristics with increasing NCF content, peaking at 60 wt.% NCF/G, with 43% charge contribution. Diffusion coefficient values for the cathodic reaction were then calculated, and the maximum value is indeed attributed to the 60 wt.% NCF/G at 1.22×10^{-8} cm 2 s $^{-1}$. Correlating the electrochemical trends to

the electrode morphologies, the electrodes (60 and 67 wt.%) where NCF formed a compact film around graphite, showed the highest diffusion coefficient, and Q_{Pseudocapacitive} values, due to the facilitation of more efficient ion mass transport, as compared to the ones where the NCF network was looser (40 and 50 wt.%). Notably, the 70 wt.% NCF/G was characterised by the existence of low current density, stemming from capacitive current only, as no redox reactions could be facilitated. EIS data also concurred to these findings, showcasing decrease in charge transfer resistance, with increasing NCF content, with the lowest attributed to the 60 wt.% NCF sample at 250 Ohm. The molecular interactions between NCF and Li⁺ were also confirmed by solid state NMR experiments, where after Li⁺ graphite intercalation, Li⁺ are located into two different environments; 1) in Li⁺-intercalated graphite and 2) in an NCF network that acts as an ion reservoir. The latter is confirmed by the close proximity (<1 nm) of Li⁺ to the H⁺ from the NCF surface groups. This is indicative of Li⁺ movement through the nanochannels.

Apart from NCF content, NCF nanoarchitecture is also investigated as a crucial parameter that affects ion mass transport, and charge storage phenomena. In Chapter 5, three electrode compositions with variable electrospun nanocellulose fibre (EL-NCF) content ranging from 50, 60 and 67 wt.% EL-NCF content, were assessed in Li⁺ environment half-cells. Electrospinning is a method where well-distinguished fibrous and porous mats can be produced, as seen from the acquired SEM images. This structural change causes different interactions between the electrode materials, as well as with the electrode/electrolyte interface. From the Dunn analysis, the total current was deconvoluted in the respective faradaic, capacitive and pseudocapacitive contributions. EL-NCF still contributes to improved pseudocapacitive characteristics with increasing EL-NCF content from 50 to 60 wt.%, peaking at 60 wt.% content with 37% charge contribution. Comparing the results with the non-electrospun architecture, the contribution is slightly lower than the 60 wt.% NCF counterparts. Interestingly, the capacitive current underwent a massive drop from 31 to 6%, and was turned to faradaic current, which was increased from 26 to 57%. These phenomena are possibly owed to the higher EL-NCF surface area and different contact with graphite particles, yielding higher faradaic and lower capacitive current proportions. Pseudocapacitive contributions are still considered high within the EL-NCF composition. EIS data and diffusion coefficient liaise with this trend, with the maximum D being $5.88 \times 10^{-9}~\text{cm}^2~\text{s}^{-1}$ for 60 wt.% EL-NCF content. It remains lower than the 60 wt.% EL-NCF counterpart at 11.22×10^{-8} cm² s⁻¹, consistent with the lower pseudocapacitive characteristics.

An alternative battery chemistry was used to test the versatility of NCF in Chapter 6. Three NCF/G electrode compositions from 50, 60 and 67 o 70 wt.% NCF, were assessed in Al-based full battery cells, containing ionic liquid EMImCl-AlC $_3$ (r = 1.5) electrolyte. In a similar manner, increasing NCF content contributed to improved pseudocapacitive characteristics and ion mobility properties, as evidenced by the calculated diffusion coefficient values, with the highest

pseudocapacitive value achieved by the 67 wt.% NCF/G electrode, at 72%. Also, the increasing NCF content caused a transformation of faradaic current to pseudocapacitive, showing that chloroaluminate anion mass transport within the bulk of the electrode was improved. Charge discharge curves of the 60 and 67 wt.% NCF/G electrodes were recorded, and the 67 wt.% electrode specific capacity reached a maximum of 64 mA h g⁻¹ at 5 mA g⁻¹. Comparing the two compositions at 60 mA g⁻¹charge rate, the 67 wt.% NCF electrode achieved a higher specific capacity of 44.9 mA h g⁻¹ (CE = 99%) compared to 32 mA h g⁻¹ (CE = 88%) for the 60 wt.% NCF counterpart. This is consistent with the ion mobility and pseudocapacitive properties, as the electrode containing higher amount of NCF is probably absorbing higher amounts of ionic liquid electrolyte, leading to higher ion availability.

The flexibility of the NCF/G electrode in the Aluminium-graphite battery was demonstrated by the assemble and of flexible pouch cells with a PP casing, where EIS spectra were recorded at the non-bent and the bent state of the cell. The results showed a negligible increase of 16% for the R_{Ω} value upon cell bending.

Finally, on the basis of fabricating all-flexible battery components, electrochemical sol-gel deposition is used to manufacture a covalently bonded NCF/G electrode-electrolyte interface, that can withstand stress and not detach upon mechanical deformation. As a first step, an organosilane-based layer is deposited and bound on the NCF surface functional groups, as revealed by SEM/EDX and FT-IR experiments.

This thesis documented the development of intrinsically flexible NCF/G battery electrodes that can be implemented in both Li⁺ and Al-based systems. It was demonstrated that nanocellulose acts as more than a flexible binder, by promoting ion mass transport within the electrode. Nanocellulose content and architecture are also tightly correlated to ion mass transport and charge storage mechanism fluctuations. This work paves the way for the development of fully flexible, safe and sustainable batteries, for future use in modern electronic wearable devices.

7.2 Future work

This work demonstrated the development of fully flexible NCF/G electrodes, where the role of NCF in charge storage mechanisms was also deciphered, however there are still several research questions that remain open. Potential routes for future research using this work as a reference point, are discussed below.

7.2.1 Optimisation and fulfilment of electrochemical sol-gel deposition of ionic liquid electrolyte

Electrochemical sol-gel deposition of a silanol-based layer on the NCF/G surface was endeavoured for the first time, as described in Chapter 6. Optimisation of the procedure in terms of deposition time and tailoring of the precursor solution composition are essential in order to accomplish a homogeneously deposited sol-gel layer. Further investigation is needed in terms of structural characterisation, as from initial data it is shown that the silanol-based layer forms covalent bonds directly with the NCF surface functional groups. NCF content and structure within the electrode would be expected to affect the binding properties with the solgel layer. The second step of the route is yet to be realised, where the ionic liquid electrolyte is deposited and bound on the intermediate sol-gel layer.

7.2.2 In depth structural studies of graphite/NCF charged and discharged electrodes

Solid state ²⁷Al-NMR experiments at the charged and discharged state of the NCF/G electrode would be extremely useful in order to reveal the molecular environments around AlCl₄ upon intercalation and de-intercalation of the anion into graphite.[190] Interactions with the NCF matrix would be highlighted, offering a better understanding of the ion mass transport properties of NCF within the Al-graphite battery. Understanding the mechanism of diffusion through the nanochannels will provide an overview of the key-differences between AlCl₄ anion transport and Li⁺ cation mechanism. Possibly, ions interact with different parts of NCF, so that mass transfer across the electrode is enabled. In operando electrochemical atomic force microscopy on the other hand, is a powerful tool for the monitoring of structural alterations upon charging and discharging of a battery electrode [191]. As a result, morphological changes in the atomic scale where nanofibrils are visible could be recorded upon cycling the NCF/G electrode. This measurement will shed light on possible NCF swelling phenomena and NCF-ion interacting regions, indicative of ion mass transport. The measurement could be performed for any battery chemistry, however, comparison between Li⁺ and AlCl₄⁻ ions, would be useful as the different ion radius would manifest as different extent of swelling and opening of the nanochannels. This study would ideally be complimentary with solid state NMR experiments.

7.2.3 Modelling and machine learning

Finally, with the rise of Artificial Intelligence and Machine Learning, the behaviour of materials within battery systems can be pre-investigated and tailored, in terms of capacity, rate capability, efficiency etc. Optimisation strategies can be recommended, by adapting the electrode materials structure, architecture and content. Modelling of NCF interactions with other materials, would offer direct insights on the preparation of electrodes where the full potential of the biopolymer is used, reducing cost and time, but increasing the efficiency of experimental procedures. [192, 193]

7.2.4 Monolithic integration with flexible electronic devices

By demonstrating the mechanical flexibility of battery electrodes based on nanocellulose, the next step forward would be the integration with flexible electronic devices. Considering the requirements for integration, mechanical properties of nanocellulose-based electrodes can be further optimised to achieve fully deformable and stretchable character. The ultimate goal would be the monolithic integration of battery and electronic devices, to achieve seamless architectural connectivity between the two compartments. In such a case, compact and lightweight configurations can be achieved via simplified co-fabrication of the electronic and power source parts, where delamination risk can be minimised. Performance-wise, a shorter distance between the components can increase energy efficiency by reducing losses due to resistance. As a result, nanocellulose-based batteries could be implemented as a building block for fully reconfigurable electronics-battery designs, that also align with ecological requisites. [194, 195]

List of publications

- 1. E. Founta, M. Caravetta, M. Thielke, A. J. B. Sobrido, L. W. Gordon, T. Prodromakis, C. Ponce de León, D.G. Georgiadou and T. Schoetz, "Understanding Charge Storage Mechanisms in Flexible Nanocellulose/Graphite Battery Electrodes", *ChemElectroChem* (2025) 2500096 (https://doi.org/10.1002/celc.202500096).
- **2.** <u>E. Founta</u>, C. Ponce de León, T.Schoetz, D.G. Georgiadou, "Recent progress on flexible cellulose-based energy storage systems for wearable devices", *Journal of Materials Chemistry A* (2025) (under submission).
- **3.** <u>E. Founta</u>, H. Srinkat, C. Ponce de León, D.G. Georgiadou, T. Schoetz, "Aluminium-graphite/nanocellulose battery with covalently bonded ionic liquid electrolyte" (in preparation).

Conference participation & proceedings

- 1. <u>E. Founta</u>, T. Schoetz, D.G. Georgiadou, T. Prodromakis and C. Ponce de León, "Nanocellulose-based flexible electrodes for safe and sustainable energy storage" (oral), ECS Meeting Abstracts (2022), MA2022-02 275, (DOI 10.1149/MA2022-023275mtgabs). 242nd ECS Conference, Atlanta USA
- 2. <u>E. Founta</u>, T. Schoetz, C. Ponce de León, T. Prodromakis and D.G. Georgiadou, "Towards Flexible and Sustainable Energy Storage: Molecular-scale Understanding of Nanocellulose/Graphite Battery Electrodes" (oral), InnoLAE 2023, Cambridge UK
- 3. <u>E. Founta</u>, T. Schoetz, C. Ponce de León, T. Prodromakis and D.G. Georgiadou, "Molecular-level Insights into Flexible and Sustainable Nanocellulose/Graphite Battery Electrodes for Future Energy Storage" (poster), The Faraday Institution Conference 2023, Birmingham UK
- 4. <u>E. Founta</u>, M. Caravetta, M. Thielke, A. B. J. Sobrido, L. W. Gordon, T. Prodromakis, C. Ponce de León, D. G. Georgiadou and T. Schoetz, "Fundamental understanding of charge storage mechanisms in flexible graphite/nanocellulose composite electrodes" (oral), InnoLAE 2025, Cambridge UK

Appendix A Supporting solid state NMR data

A.1 Solid state NMR Li spectra of graphite/nanocellulose fibre electrodes

The NMR data and spectra presented in this Appendix were acquired by Dr Leo W Gordon at the City College of New York.

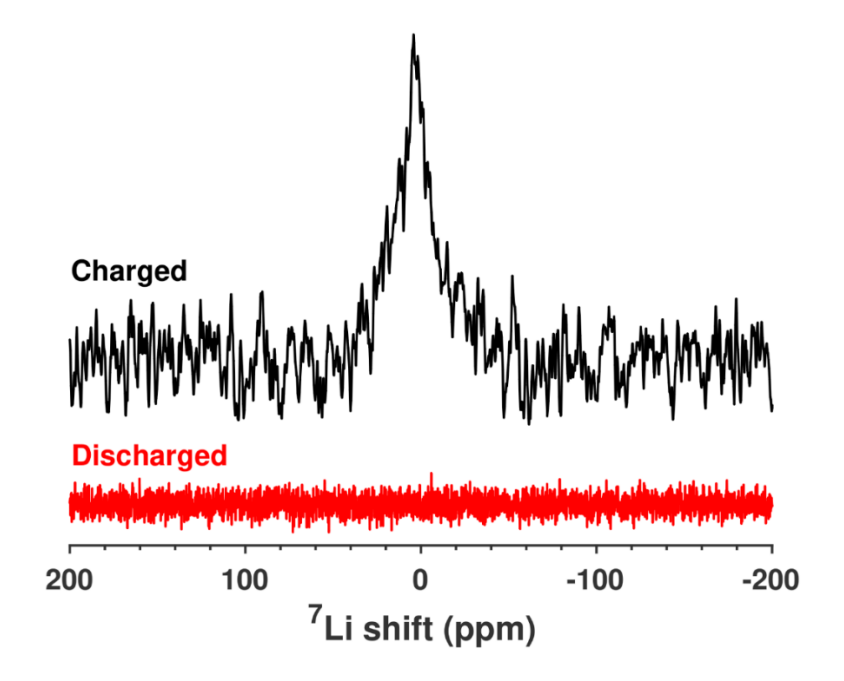


Figure A 1 Solid state ⁷Li NMR acquired for a 60 wt.% NCF electrode at the charged and discharged state. A two-electrode symmetric cell was assembled and charged until 1V. As a result, one of the 60 wt.% NCF electrodes was at the charged (Li⁺ intercalation) and the other one at the discharged state (Li⁺ de-intercalation). The presence of a ⁷Li signal at the charged state confirms Li⁺ intercalation at the 60 wt.% NCF/G electrode.

A.2 NMR Fitting parameters from DMFit

SAMPLE, EXPERIMENT	SITE 1 SHIFT (PPM)	SITE 2 SHIFT (PPM)	SITE 1 RELATIVE INTEGRATION (%)	SITE 2 RELATIVE INTEGRATION (%)	SITE 1 LINEWIDTH (HZ)	SITE 2 LINEWIDTH (HZ)
BEFORE INTERCALATION, SINGLE PULSE	9.36	-32.17	86.88	13.12	10471	8647
BEFORE INTERCALATION, CP-MAS	9.36	-32.17	69.88	30.12	7847	13903
AFTER INTERCALATION, SINGLE PULSE	7.07	-24.50	71.17	28.83	10642	13988
AFTER INTERCALATION, CP-MAS	7.07	-24.50	45.56	54.44	8217	21309

- [1] D. G. Mackanic, M. Kao, and Z. Bao, "Enabling Deformable and Stretchable Batteries," Advanced Energy Materials, vol. 10, no. 29, p. 2001424, 2020, doi: https://doi.org/10.1002/aenm.202001424.
- [2] W. Liu, M.-S. Song, B. Kong, and Y. Cui, "Flexible and Stretchable Energy Storage: Recent Advances and Future Perspectives," *Advanced Materials*, vol. 29, no. 1, p. 1603436, 2017, doi: https://doi.org/10.1002/adma.201603436.
- [3] D. M. Zolin L., Curtil D., Chaussy D., Penazzi N., Beneventi D., Gerbaldi C., "Flexible Cellulose-Based Electrodes: Towards Eco-friendly All-paper Batteries," *Chemical Engineering Transactions*, vol. 41, pp. 361-366, 2014.
- [4] M. M. Titirici, "Sustainable Batteries—Quo Vadis?," *Advanced Energy Materials*, vol. 11, no. 10, 2021, doi: 10.1002/aenm.202003700.
- [5] D. Larcher and J. M. Tarascon, "Towards greener and more sustainable batteries for electrical energy storage," *Nature Chemistry*, vol. 7, no. 1, pp. 19-29, 2015/01/01 2015, doi: 10.1038/nchem.2085.
- [6] F. Degen, "Lithium-ion battery cell production in Europe: Scenarios for reducing energy consumption and greenhouse gas emissions until 2030," *Journal of Industrial Ecology*, vol. 27, no. 3, pp. 964-976, 2023, doi: https://doi.org/10.1111/jiec.13386.
- [7] F. Degen, M. Winter, D. Bendig, and J. Tübke, "Energy consumption of current and future production of lithium-ion and post lithium-ion battery cells," *Nature Energy*, vol. 8, no. 11, pp. 1284-1295, 2023/11/01 2023, doi: 10.1038/s41560-023-01355-z.
- [8] Q. Meng *et al.*, "Reevaluating Flexible Lithium-Ion Batteries from the Insights of Mechanics and Electrochemistry," *Electrochemical Energy Reviews*, vol. 5, no. 2, p. 30, 2022/11/21 2022, doi: 10.1007/s41918-022-00150-w.
- [9] C. Y. Chan, P.-K. Lee, Z. Xu, and D. Y. W. Yu, "Designing high-power graphite-based dualion batteries," *Electrochimica Acta*, vol. 263, pp. 34-39, 2018/02/10/ 2018, doi: https://doi.org/10.1016/j.electacta.2018.01.036.
- [10] D.-Y. Wang *et al.*, "Advanced rechargeable aluminium ion battery with a high-quality natural graphite cathode," *Nature Communications*, vol. 8, no. 1, p. 14283, 2017/02/13 2017, doi: 10.1038/ncomms14283.
- [11] J. Asenbauer, T. Eisenmann, M. Kuenzel, A. Kazzazi, Z. Chen, and D. Bresser, "The success story of graphite as a lithium-ion anode material fundamentals, remaining challenges, and recent developments including silicon (oxide) composites," *Sustainable Energy & Fuels*, 10.1039/D0SE00175A vol. 4, no. 11, pp. 5387-5416, 2020, doi: 10.1039/D0SE00175A.
- [12] W. Luo *et al.*, "Surface and Interface Engineering of Silicon-Based Anode Materials for Lithium-Ion Batteries," *Advanced Energy Materials*, vol. 7, no. 24, p. 1701083, 2017, doi: https://doi.org/10.1002/aenm.201701083.
- [13] Z. Zhu, G. Xiao, J. Chen, and S. Fu, "Wood nanotechnology: a more promising solution toward energy issues: a mini-review," *Cellulose*, vol. 27, no. 15, pp. 8513-8526, 2020, doi: 10.1007/s10570-020-03404-2.

- [14] T. Rasheed, M. T. Anwar, A. Naveed, and A. Ali, "Biopolymer Based Materials as Alternative Greener Binders for Sustainable Electrochemical Energy Storage Applications," *ChemistrySelect*, vol. 7, no. 39, p. e202203202, 2022, doi: https://doi.org/10.1002/slct.202203202.
- [15] X. Du, Z. Zhang, W. Liu, and Y. Deng, "Nanocellulose-based conductive materials and their emerging applications in energy devices A review," *Nano Energy*, vol. 35, pp. 299-320, 2017/05/01/2017, doi: https://doi.org/10.1016/j.nanoen.2017.04.001.
- [16] S. S. Jeong, N. Böckenfeld, A. Balducci, M. Winter, and S. Passerini, "Natural cellulose as binder for lithium battery electrodes," *Journal of Power Sources*, vol. 199, pp. 331-335, 2012/02/01/ 2012, doi: https://doi.org/10.1016/j.jpowsour.2011.09.102.
- [17] S. Lei et al., "Opportunities for biocompatible and safe zinc-based batteries," Energy & Environmental Science, 10.1039/D2EE02267B vol. 15, no. 12, pp. 4911-4927, 2022, doi: 10.1039/D2EE02267B.
- [18] H. Au, M. Crespo-Ribadeneyra, and M.-M. Titirici, "Beyond Li-ion batteries: performance, materials diversification, and sustainability," *One Earth,* vol. 5, no. 3, pp. 207-211, 2022/03/18/ 2022, doi: https://doi.org/10.1016/j.oneear.2022.02.014.
- [19] Y. Ye, L. Yu, E. Lizundia, Y. Zhu, C. Chen, and F. Jiang, "Cellulose-Based Ionic Conductor: An Emerging Material toward Sustainable Devices," *Chemical Reviews*, vol. 123, no. 15, pp. 9204-9264, 2023/08/09 2023, doi: 10.1021/acs.chemrev.2c00618.
- [20] S. Jing, L. Wu, A. P. Siciliano, C. Chen, T. Li, and L. Hu, "The Critical Roles of Water in the Processing, Structure, and Properties of Nanocellulose," *ACS Nano*, vol. 17, no. 22, pp. 22196-22226, 2023/11/28 2023, doi: 10.1021/acsnano.3c06773.
- [21] S. Peter, N. Lyczko, D. Gopakumar, H. J. Maria, A. Nzihou, and S. Thomas, "Nanocellulose and its derivative materials for energy and environmental applications," *Journal of Materials Science*, vol. 57, no. 13, pp. 6835-6880, 2022/04/01 2022, doi: 10.1007/s10853-022-07070-6.
- [22] M. Gubitosi *et al.*, "Stable, metastable and unstable cellulose solutions," *Royal Society Open Science*, vol. 4, no. 8, p. 170487, 2017, doi: doi:10.1098/rsos.170487.
- [23] S. P. Saric, R. K. Schofield, and B. A. Keen, "The dissociation constants of the carboxyl and hydroxyl groups in some insoluble and sol-forming polysaccharides," *Proceedings of the Royal Society of London. Series A. Mathematical and Physical Sciences*, vol. 185, no. 1003, pp. 431-447, 1946, doi: doi:10.1098/rspa.1946.0029.
- [24] "Cellulose." Wikipedia. https://en.wikipedia.org/wiki/Cellulose (accessed 1.10.2024.
- [25] L.-L. Lu *et al.*, "Wood-Inspired High-Performance Ultrathick Bulk Battery Electrodes," *Advanced Materials*, vol. 30, no. 20, p. 1706745, 2018, doi: https://doi.org/10.1002/adma.201706745.
- [26] X. Wang, H. Hua, X. Xie, P. Zhang, and J. Zhao, "Hydroxyl on the filler surface promotes Li+ conduction in PEO all-solid-state electrolyte," *Solid State Ionics*, vol. 372, p. 115768, 2021/12/01/ 2021, doi: https://doi.org/10.1016/j.ssi.2021.115768.
- [27] Z. Wang, Y.-H. Lee, S.-W. Kim, J.-Y. Seo, S.-Y. Lee, and L. Nyholm, "Why Cellulose-Based Electrochemical Energy Storage Devices?," *Advanced Materials*, vol. 33, no. 28, p. 2000892, 2021, doi: https://doi.org/10.1002/adma.202000892.
- [28] J. H. Park, S. H. Kim, and K. H. Ahn, "Role of carboxymethyl cellulose binder and its effect on the preparation process of anode slurries for Li-ion batteries," *Colloids and*

- Surfaces A: Physicochemical and Engineering Aspects, vol. 664, p. 131130, 2023/05/05/2023, doi: https://doi.org/10.1016/j.colsurfa.2023.131130.
- [29] T. Xu *et al.*, "Advanced Nanocellulose-Based Composites for Flexible Functional Energy Storage Devices," *Advanced Materials*, vol. 33, no. 48, p. 2101368, 2021, doi: https://doi.org/10.1002/adma.202101368.
- [30] N. Lingappan, L. Kong, and M. Pecht, "The significance of aqueous binders in lithium-ion batteries," *Renewable and Sustainable Energy Reviews*, vol. 147, p. 111227, 2021/09/01/2021, doi: https://doi.org/10.1016/j.rser.2021.111227.
- [31] P. S. Salini, S. V. Gopinadh, A. Kalpakasseri, B. John, and M. Thelakkattu Devassy, "Toward Greener and Sustainable Li-Ion Cells: An Overview of Aqueous-Based Binder Systems," *ACS Sustainable Chemistry & Engineering*, vol. 8, no. 10, pp. 4003-4025, 2020/03/16 2020, doi: 10.1021/acssuschemeng.9b07478.
- J. Fei, Q. Sun, Y. Cui, J. Li, and J. Huang, "Sodium carboxyl methyl cellulose and polyacrylic acid binder with enhanced electrochemical properties for ZnMoO4·0.8H2O anode in lithium ion batteries," *Journal of Electroanalytical Chemistry*, vol. 804, pp. 158-164, 2017/11/01/ 2017, doi: https://doi.org/10.1016/j.jelechem.2017.09.061.
- [33] C. Zhong, J.-Z. Wang, S.-L. Chou, K. Konstantinov, M. Rahman, and H.-K. Liu, "Nanocrystalline NiO hollow spheres in conjunction with CMC for lithium-ion batteries," *Journal of Applied Electrochemistry*, vol. 40, no. 7, pp. 1415-1419, 2010/07/01 2010, doi: 10.1007/s10800-010-0118-6.
- [34] W. Zhang, M. Qian, G. Luo, X. Feng, C. Wu, and W. Qin, "Improved lithium ion storage performance of Ti3C2Tx MXene@S composite with carboxymethyl cellulose binder," *Journal of Colloid and Interface Science*, vol. 641, pp. 15-25, 2023/07/01/ 2023, doi: https://doi.org/10.1016/j.jcis.2023.03.074.
- [35] Y. Guo *et al.*, "Accelerating the Li-ion transmission of free-standing thick electrodes by using CMC-Li as ion-conducting binder," *Materials Today Sustainability*, vol. 21, p. 100304, 2023/03/01/ 2023, doi: https://doi.org/10.1016/j.mtsust.2022.100304.
- [36] L.-L. Chen *et al.*, "Nonmetal Current Collectors: The Key Component for High-Energy-Density Aluminum Batteries," *Advanced Materials*, vol. 32, no. 42, p. 2001212, 2020, doi: https://doi.org/10.1002/adma.202001212.
- [37] L. Qiu, Z. Shao, D. Wang, F. Wang, W. Wang, and J. Wang, "Carboxymethyl cellulose lithium (CMC-Li) as a novel binder and its electrochemical performance in lithium-ion batteries," *Cellulose*, vol. 21, no. 4, pp. 2789-2796, 2014/08/01 2014, doi: 10.1007/s10570-014-0274-7.
- [38] L. Jabbour, C. Gerbaldi, D. Chaussy, E. Zeno, S. Bodoardo, and D. Beneventi, "Microfibrillated cellulose–graphite nanocomposites for highly flexible paper-like Li-ion battery electrodes," *Journal of Materials Chemistry*, 10.1039/C0JM01219J vol. 20, no. 35, pp. 7344-7347, 2010, doi: 10.1039/C0JM01219J.
- [39] G. A. Elia et al., "An Overview and Future Perspectives of Aluminum Batteries," Advanced Materials, vol. 28, no. 35, pp. 7564-7579, 2016, doi: https://doi.org/10.1002/adma.201601357.
- [40] F. Ambroz, T. J. Macdonald, and T. Nann, "Trends in Aluminium-Based Intercalation Batteries," *Advanced Energy Materials*, vol. 7, no. 15, p. 1602093, 2017, doi: https://doi.org/10.1002/aenm.201602093.

- [41] M.-C. Lin *et al.*, "An ultrafast rechargeable aluminium-ion battery," *Nature*, vol. 520, no. 7547, pp. 324-328, 2015/04/01 2015, doi: 10.1038/nature14340.
- [42] D. Y. Wang and Others, "Advanced rechargeable aluminium ion battery with a high-quality natural graphite cathode," *Nat. Commun.*, vol. 8, p. 14283, 2017, doi: 10.1038/ncomms14283.
- [43] D. Pawcenis, M. Leśniak, M. Szumera, M. Sitarz, and J. Profic-Paczkowska, "Effect of hydrolysis time, pH and surfactant type on stability of hydrochloric acid hydrolyzed nanocellulose," *International Journal of Biological Macromolecules*, vol. 222, pp. 1996-2005, 2022/12/01/ 2022, doi: https://doi.org/10.1016/j.ijbiomac.2022.09.289.
- [44] S. Leijonmarck, A. Cornell, G. Lindbergh, and L. Wågberg, "Single-paper flexible Li-ion battery cells through a paper-making process based on nano-fibrillated cellulose," *Journal of Materials Chemistry A*, 10.1039/C3TA01532G vol. 1, no. 15, pp. 4671-4677, 2013, doi: 10.1039/C3TA01532G.
- [45] M. Yu et al., "Freestanding and Sandwich-Structured Electrode Material with High Areal Mass Loading for Long-Life Lithium–Sulfur Batteries," *Advanced Energy Materials*, vol. 7, no. 11, p. 1602347, 2017, doi: https://doi.org/10.1002/aenm.201602347.
- [46] X. Yue *et al.*, "A novel 3D bacterial cellulose network as cathodic scaffold and hydrogel electrolyte for zinc-ion batteries," *Journal of Power Sources*, vol. 557, p. 232553, 2023/02/15/ 2023, doi: https://doi.org/10.1016/j.jpowsour.2022.232553.
- [47] Y. Sun et al., "Direct atomic-scale confirmation of three-phase storage mechanism in Li4Ti5O12 anodes for room-temperature sodium-ion batteries," *Nature Communications*, vol. 4, no. 1, p. 1870, 2013/05/21 2013, doi: 10.1038/ncomms2878.
- [48] J.-H. Kim, D. Lee, Y.-H. Lee, W. Chen, and S.-Y. Lee, "Nanocellulose for Energy Storage Systems: Beyond the Limits of Synthetic Materials," *Advanced Materials*, vol. 31, no. 20, p. 1804826, 2019, doi: 10.1002/adma.201804826.
- [49] X. Wang, C. Yao, F. Wang, and Z. Li, "Cellulose-Based Nanomaterials for Energy Applications," *Small*, vol. 13, no. 42, Nov 2017, doi: 10.1002/smll.201702240.
- [50] T. Saito and A. Isogai, "Ion-exchange behavior of carboxylate groups in fibrous cellulose oxidized by the TEMPO-mediated system," *Carbohydrate Polymers*, vol. 61, no. 2, pp. 183-190, 2005/08/04/ 2005, doi: https://doi.org/10.1016/j.carbpol.2005.04.009.
- [51] S. Farag, H. M. Ibrahim, A. Amr, M. S. Asker, and A. El-shafie, "Preparation and Characterization of Ion Exchanger Based on Bacterial Cellulose for Heavy Metal Cation Removal," *Egyptian Journal of Chemistry*, vol. 62, no. Special Issue (Part 2) Innovation in Chemistry, pp. 457-465, 2019, doi: 10.21608/ejchem.2019.12622.1787.
- [52] D. Miyashiro, R. Hamano, and K. Umemura, "A Review of Applications Using Mixed Materials of Cellulose, Nanocellulose and Carbon Nanotubes," *Nanomaterials*, vol. 10, no. 2, p. 186, 2020. [Online]. Available: https://www.mdpi.com/2079-4991/10/2/186.
- [53] J. Wei et al., "Advanced Cellulosic Materials Toward High-Performance Metal Ion Batteries," *Advanced Energy Materials*, vol. 14, no. 23, p. 2400208, 2024, doi: https://doi.org/10.1002/aenm.202400208.
- [54] N. Lavoine, I. Desloges, A. Dufresne, and J. Bras, "Microfibrillated cellulose Its barrier properties and applications in cellulosic materials: A review," *Carbohydrate Polymers*, vol. 90, no. 2, pp. 735-764, 2012/10/01/ 2012, doi: https://doi.org/10.1016/j.carbpol.2012.05.026.

- [55] H. V. Lee, S. B. A. Hamid, and S. K. Zain, "Conversion of Lignocellulosic Biomass to Nanocellulose: Structure and Chemical Process," *The Scientific World Journal*, vol. 2014, no. 1, p. 631013, 2014, doi: https://doi.org/10.1155/2014/631013.
- [56] W. Chen, H. Yu, S.-Y. Lee, T. Wei, J. Li, and Z. Fan, "Nanocellulose: a promising nanomaterial for advanced electrochemical energy storage," *Chemical Society Reviews*, 10.1039/C7CS00790F vol. 47, no. 8, pp. 2837-2872, 2018, doi: 10.1039/C7CS00790F.
- [57] P. Jacek, F. Dourado, M. Gama, and S. Bielecki, "Molecular aspects of bacterial nanocellulose biosynthesis," *Microbial Biotechnology*, vol. 12, no. 4, pp. 633-649, 2019, doi: https://doi.org/10.1111/1751-7915.13386.
- [58] R. Masoodi, R. F. El-Hajjar, K. M. Pillai, and R. Sabo, "Mechanical characterization of cellulose nanofiber and bio-based epoxy composite," *Materials & Design (1980-2015)*, vol. 36, pp. 570-576, 2012/04/01/ 2012, doi: https://doi.org/10.1016/j.matdes.2011.11.042.
- [59] D. A. Gopakumar, V. Arumughan, D. Pasquini, S.-Y. Leu, A. K. H.P.S, and S. Thomas, "Chapter 3 Nanocellulose-Based Membranes for Water Purification," in *Nanoscale Materials in Water Purification*, S. Thomas, D. Pasquini, S.-Y. Leu, and D. A. Gopakumar Eds.: Elsevier, 2019, pp. 59-85.
- [60] R. T. Varghese et al., "A review on the best bioadsorbent membrane- nanocellulose for effective removal of pollutants from aqueous solutions," *Carbohydrate Polymer Technologies and Applications*, vol. 3, p. 100209, 2022/06/01/ 2022, doi: https://doi.org/10.1016/j.carpta.2022.100209.
- [61] M. Z. Ansari, S. N. Banitaba, S. Khademolqorani, I. Kamika, and V. V. Jadhav, "Overlooked Promising Green Features of Electrospun Cellulose-Based Fibers in Lithium-Ion Batteries," *ACS Omega*, vol. 8, no. 46, pp. 43388-43407, 2023/11/21 2023, doi: 10.1021/acsomega.3c05068.
- [62] M. W. Thielke *et al.*, "Full Lignin-Derived Electrospun Carbon Materials as Electrodes for Supercapacitors," (in English), *Frontiers in Materials*, Original Research vol. 9, 2022-May-17 2022, doi: 10.3389/fmats.2022.859872.
- [63] C.-W. Kim, D.-S. Kim, S.-Y. Kang, M. Marquez, and Y. L. Joo, "Structural studies of electrospun cellulose nanofibers," *Polymer*, vol. 47, no. 14, pp. 5097-5107, 2006/06/28/2006, doi: https://doi.org/10.1016/j.polymer.2006.05.033.
- [64] M. M. Hassan, X.-Y. Wang, A. A. Bristi, R. Yang, X. Li, and Q. Lu, "Composite scaffold of electrospun nano-porous cellulose acetate membrane casted with chitosan for flexible solid-state sodium-ion batteries," *Nano Energy*, vol. 128, p. 109971, 2024/09/01/ 2024, doi: https://doi.org/10.1016/j.nanoen.2024.109971.
- [65] Y. Kuang *et al.*, "Conductive Cellulose Nanofiber Enabled Thick Electrode for Compact and Flexible Energy Storage Devices," *Advanced Energy Materials*, vol. 8, no. 33, p. 1802398, 2018, doi: https://doi.org/10.1002/aenm.201802398.
- [66] D. Viet, S. Beck-Candanedo, and D. G. Gray, "Dispersion of cellulose nanocrystals in polar organic solvents," *Cellulose*, vol. 14, no. 2, pp. 109-113, 2007/04/01 2007, doi: 10.1007/s10570-006-9093-9.
- [67] L. Szabó, R. Milotskyi, G. Sharma, and K. Takahashi, "Cellulose processing in ionic liquids from a materials science perspective: turning a versatile biopolymer into the cornerstone of our sustainable future," *Green Chemistry*, 10.1039/D2GC04730F vol. 25, no. 14, pp. 5338-5389, 2023, doi: 10.1039/D2GC04730F.

- [68] R. Gordon, R. Orias, and N. Willenbacher, "Effect of carboxymethyl cellulose on the flow behavior of lithium-ion battery anode slurries and the electrical as well as mechanical properties of corresponding dry layers," *Journal of Materials Science*, vol. 55, no. 33, pp. 15867-15881, 2020/11/01 2020, doi: 10.1007/s10853-020-05122-3.
- [69] L. Qiu, Z. Shao, M. Liu, J. Wang, P. Li, and M. Zhao, "Synthesis and electrospinning carboxymethyl cellulose lithium (CMC-Li) modified 9,10-anthraquinone (AQ) high-rate lithium-ion battery," *Carbohydrate Polymers*, vol. 102, pp. 986-992, 2014/02/15/ 2014, doi: https://doi.org/10.1016/j.carbpol.2013.09.105.
- [70] J.-H. Lee, U. Paik, V. A. Hackley, and Y.-M. Choi, "Effect of Carboxymethyl Cellulose on Aqueous Processing of Natural Graphite Negative Electrodes and their Electrochemical Performance for Lithium Batteries," *Journal of The Electrochemical Society*, vol. 152, no. 9, p. A1763, 2005/07/21 2005, doi: 10.1149/1.1979214.
- [71] J. Brady, T. Dürig, P. I. Lee, and J. X. Li, "Chapter 7 Polymer Properties and Characterization," in *Developing Solid Oral Dosage Forms (Second Edition)*, Y. Qiu, Y. Chen, G. G. Z. Zhang, L. Yu, and R. V. Mantri Eds. Boston: Academic Press, 2017, pp. 181-223.
- [72] S. Majumder, A. Sharif, and M. E. Hoque, "Chapter 9 Electrospun Cellulose Acetate Nanofiber: Characterization and Applications," in *Advanced Processing, Properties, and Applications of Starch and Other Bio-Based Polymers*, F. M. Al-Oqla and S. M. Sapuan Eds.: Elsevier, 2020, pp. 139-155.
- [73] E. Erbas Kiziltas, A. Kiziltas, K. Rhodes, N. W. Emanetoglu, M. Blumentritt, and D. J. Gardner, "Electrically conductive nano graphite-filled bacterial cellulose composites," *Carbohydrate Polymers*, vol. 136, pp. 1144-1151, 2016/01/20/ 2016, doi: https://doi.org/10.1016/j.carbpol.2015.10.004.
- [74] P. Isacsson *et al.*, "Highly Conducting Nanographite-Filled Paper Fabricated via Standard Papermaking Techniques," *ACS Applied Materials & Interfaces*, vol. 12, no. 43, pp. 48828-48835, 2020/10/28 2020, doi: 10.1021/acsami.0c13086.
- [75] K. Gao, Z. Shao, X. Wang, Y. Zhang, W. Wang, and F. Wang, "Cellulose nanofibers/multi-walled carbon nanotube nanohybrid aerogel for all-solid-state flexible supercapacitors," *RSC Advances*, 10.1039/C3RA42050G vol. 3, no. 35, pp. 15058-15064, 2013, doi: 10.1039/C3RA42050G.
- [76] K. Gao et al., "Cellulose nanofiber–graphene all solid-state flexible supercapacitors," Journal of Materials Chemistry A, 10.1039/C2TA00386D vol. 1, no. 1, pp. 63-67, 2013, doi: 10.1039/C2TA00386D.
- [77] U. M. Casado, M. I. Aranguren, and N. E. Marcovich, "Preparation and characterization of conductive nanostructured particles based on polyaniline and cellulose nanofibers," *Ultrasonics Sonochemistry*, vol. 21, no. 5, pp. 1641-1648, 2014/09/01/ 2014, doi: https://doi.org/10.1016/j.ultsonch.2014.03.012.
- [78] X. Zhang, X. Wu, C. Lu, and Z. Zhou, "Dialysis-Free and in Situ Doping Synthesis of Polypyrrole@Cellulose Nanowhiskers Nanohybrid for Preparation of Conductive Nanocomposites with Enhanced Properties," *ACS Sustainable Chemistry & Engineering*, vol. 3, no. 4, pp. 675-682, 2015/04/06 2015, doi: 10.1021/sc500853m.
- [79] S. Duluard *et al.*, "Electrochromic devices based on in situ polymerised EDOT and Prussian Blue: influence of transparent conducting oxide and electrolyte composition—towards up-scaling," *New Journal of Chemistry,* 10.1039/C1NJ20231F vol. 35, no. 10, pp. 2314-2321, 2011, doi: 10.1039/C1NJ20231F.

- [80] X. Yin *et al.*, "Facile Synthesis of Poly(3,4-ethylenedioxythiophene) Film via Solid-State Polymerization as High-Performance Pt-Free Counter Electrodes for Plastic Dye-Sensitized Solar Cells," *ACS Applied Materials & Interfaces*, vol. 5, no. 17, pp. 8423-8429, 2013/09/11 2013, doi: 10.1021/am401719e.
- [81] T. Wang and L. T. Drzal, "Cellulose-Nanofiber-Reinforced Poly(lactic acid) Composites Prepared by a Water-Based Approach," *ACS Applied Materials & Interfaces*, vol. 4, no. 10, pp. 5079-5085, 2012/10/24 2012, doi: 10.1021/am301438g.
- [82] R. J. Moon, A. Martini, J. Nairn, J. Simonsen, and J. Youngblood, "Cellulose nanomaterials review: structure, properties and nanocomposites," *Chemical Society Reviews*, 10.1039/C0CS00108B vol. 40, no. 7, pp. 3941-3994, 2011, doi: 10.1039/C0CS00108B.
- [83] S. Ifuku, M. Nogi, K. Abe, K. Handa, F. Nakatsubo, and H. Yano, "Surface Modification of Bacterial Cellulose Nanofibers for Property Enhancement of Optically Transparent Composites: Dependence on Acetyl-Group DS," *Biomacromolecules*, vol. 8, no. 6, pp. 1973-1978, 2007/06/01 2007, doi: 10.1021/bm070113b.
- [84] M. Ogden, R. Hoefgen, U. Roessner, S. Persson, and G. A. Khan, "Feeding the Walls: How Does Nutrient Availability Regulate Cell Wall Composition?," *International Journal of Molecular Sciences*, vol. 19, no. 9, p. 2691, 2018. [Online]. Available: https://www.mdpi.com/1422-0067/19/9/2691.
- [85] S. Cao, J. Chen, Q. Yang, C. Xiong, R. Fan, and Z. Shi, "Highly sulfur-loaded dual-conductive cathodes based on nanocellulose for lithium-sulfur batteries," *Journal of Materials Science*, vol. 59, no. 2, pp. 563-576, 2024/01/01 2024, doi: 10.1007/s10853-023-09217-5.
- [86] Y. Xia et al., "Exploitation of function groups in cellulose materials for lithium-ion batteries applications," *Carbohydrate Polymers*, vol. 325, p. 121570, 2024/02/01/ 2024, doi: https://doi.org/10.1016/j.carbpol.2023.121570.
- [87] J.-H. Lee, Y.-M. Choi, U. Paik, and J.-G. Park, "The effect of carboxymethyl cellulose swelling on the stability of natural graphite particulates in an aqueous medium for lithium ion battery anodes," *Journal of Electroceramics*, vol. 17, no. 2, pp. 657-660, 2006/12/01 2006, doi: 10.1007/s10832-006-8975-4.
- [88] D. Chen, Z. Lou, K. Jiang, and G. Shen, "Device Configurations and Future Prospects of Flexible/Stretchable Lithium-Ion Batteries," *Advanced Functional Materials*, vol. 28, no. 51, p. 1805596, 2018, doi: https://doi.org/10.1002/adfm.201805596.
- [89] F. Mo, G. Liang, Z. Huang, H. Li, D. Wang, and C. Zhi, "An Overview of Fiber-Shaped Batteries with a Focus on Multifunctionality, Scalability, and Technical Difficulties," *Advanced Materials*, vol. 32, no. 5, p. 1902151, 2020, doi: https://doi.org/10.1002/adma.201902151.
- [90] C. Xie *et al.*, "Hybrid Lithium-Ion/Metal Electrodes Enable Long Cycle Stability and High Energy Density of Flexible Batteries," *Advanced Functional Materials*, vol. 32, no. 34, p. 2203242, 2022, doi: https://doi.org/10.1002/adfm.202203242.
- [91] J. Quan et al., "Interface Engineering of a Sandwich Flexible Electrode PAn@CoHCF Rooted in Carbon Cloth for Enhanced Sodium-Ion Storage," ACS Applied Materials & Interfaces, vol. 13, no. 20, pp. 23794-23802, 2021/05/26 2021, doi: 10.1021/acsami.1c04931.

- [92] S. H. Ha, K. H. Shin, H. W. Park, and Y. J. Lee, "Flexible Lithium-Ion Batteries with High Areal Capacity Enabled by Smart Conductive Textiles," *Small*, vol. 14, no. 43, p. 1703418, 2018, doi: https://doi.org/10.1002/smll.201703418.
- [93] Y.-H. Lee *et al.*, "Wearable Textile Battery Rechargeable by Solar Energy," *Nano Letters*, vol. 13, no. 11, pp. 5753-5761, 2013/11/13 2013, doi: 10.1021/nl403860k.
- [94] K. Lee, J. H. Choi, H. M. Lee, K. J. Kim, and J. W. Choi, "Solution-Processed Metal Coating to Nonwoven Fabrics for Wearable Rechargeable Batteries," *Small*, vol. 14, no. 43, p. 1703028, 2018, doi: https://doi.org/10.1002/smll.201703028.
- [95] C. Jiang et al., "Flexible Interface Design for Stress Regulation of a Silicon Anode toward Highly Stable Dual-Ion Batteries," *Advanced Materials*, vol. 32, no. 17, p. 1908470, 2020, doi: https://doi.org/10.1002/adma.201908470.
- [96] B. Liu et al., "Hierarchical Three-Dimensional ZnCo2O4 Nanowire Arrays/Carbon Cloth Anodes for a Novel Class of High-Performance Flexible Lithium-Ion Batteries," *Nano Letters*, vol. 12, no. 6, pp. 3005-3011, 2012/06/13 2012, doi: 10.1021/nl300794f.
- [97] O. A. Kuznetsov, S. Mohanty, E. Pigos, G. Chen, W. Cai, and A. R. Harutyunyan, "High energy density flexible and ecofriendly lithium-ion smart battery," *Energy Storage Materials*, vol. 54, pp. 266-275, 2023/01/01/ 2023, doi: https://doi.org/10.1016/j.ensm.2022.10.023.
- [98] Y. Mao et al., "Carbon Foam-Supported VS2 Cathode for High-Performance Flexible Self-Healing Quasi-Solid-State Zinc-Ion Batteries," *Small*, vol. 19, no. 25, p. 2207998, 2023, doi: https://doi.org/10.1002/smll.202207998.
- [99] C. Zou et al., "Flexible Aluminum-Air Battery Based on High-Performance Three-Dimensional Dual-Network PVA/KC/KOH Composite Gel Polymer Electrolyte," *Langmuir*, vol. 40, no. 19, pp. 9999-10007, 2024/05/14 2024, doi: 10.1021/acs.langmuir.4c00159.
- [100] A. Rahmanudin, Z. Khan, K. Tybrandt, and N. Kim, "Sustainable stretchable batteries for next-generation wearables," *Journal of Materials Chemistry A*, 10.1039/D3TA03482H vol. 11, no. 42, pp. 22718-22736, 2023, doi: 10.1039/D3TA03482H.
- [101] S. Ahankari, P. Paliwal, A. Subhedar, and H. Kargarzadeh, "Recent Developments in Nanocellulose-Based Aerogels in Thermal Applications: A Review," *ACS Nano*, vol. 15, no. 3, pp. 3849-3874, 2021/03/23 2021, doi: 10.1021/acsnano.0c09678.
- [102] P. Srichola *et al.*, "Recycling of Nanocellulose from Polyester–Cotton Textile Waste for Modification of Film Composites," *Polymers*, vol. 15, no. 15, p. 3324, 2023. [Online]. Available: https://www.mdpi.com/2073-4360/15/15/3324.
- [103] Y. Tang, Y. Zhang, W. Li, B. Ma, and X. Chen, "Rational material design for ultrafast rechargeable lithium-ion batteries," *Chemical Society Reviews*, 10.1039/C4CS00442F vol. 44, no. 17, pp. 5926-5940, 2015, doi: 10.1039/C4CS00442F.
- [104] Z. Zhang and P. Ramadass, "Lithium-Ion Battery Systems and Technology," in Encyclopedia of Sustainability Science and Technology, R. A. Meyers Ed. New York, NY: Springer New York, 2012, pp. 6122-6149.
- [105] Z. Jiang, C. Huang, S. Zhang, W. Luo, Y. Cheng, and X. Yang, "Cellulose-based high-loading flexible electrode for lithium-ion battery with high volumetric energy density," *Chemical Engineering Journal*, vol. 489, p. 151189, 2024/06/01/ 2024, doi: https://doi.org/10.1016/j.cej.2024.151189.

- [106] K. Kim, R. M. Loh, R. Martinez, C. K. Chan, and Y. Hwa, "Failure Modes of Flexible LiCoO2 Cathodes Incorporating Polyvinylidene Fluoride Binders with Different Molecular Weights," *ACS Applied Materials & Interfaces*, vol. 16, no. 5, pp. 5926-5936, 2024/02/07 2024, doi: 10.1021/acsami.3c17310.
- [107] V. Gopalakrishnan, A. Sundararajan, P. Omprakash, and D. Bhat Panemangalore, "Review—Energy Storage through Graphite Intercalation Compounds," *Journal of The Electrochemical Society*, vol. 168, no. 4, p. 040541, 2021/04/29 2021, doi: 10.1149/1945-7111/abf973.
- [108] P. Bhauriyal, A. Mahata, and B. Pathak, "The staging mechanism of AlCl4– intercalation in a graphite electrode for an aluminium-ion battery," *Phys. Chem. Chem. Phys.*, vol. 19, p. 7980, 2017, doi: 10.1039/C7CP00453B.
- [109] S. Yang, Y. Huang, S. Su, G. Han, and J. Liu, "Hybrid humics/sodium carboxymethyl cellulose water-soluble binder for enhancing the electrochemical performance of a Liion battery cathode," *Powder Technology*, vol. 351, pp. 203-211, 2019/06/01/ 2019, doi: https://doi.org/10.1016/j.powtec.2019.04.027.
- [110] H. Popp, M. Koller, M. Jahn, and A. Bergmann, "Mechanical methods for state determination of Lithium-Ion secondary batteries: A review," *Journal of Energy Storage*, vol. 32, p. 101859, 2020/12/01/ 2020, doi: https://doi.org/10.1016/j.est.2020.101859.
- [111] Y. Zhou et al., "Decoupling Ionic and Electronic Pathways in Low-Dimensional Hybrid Conductors," *Journal of the American Chemical Society*, vol. 141, no. 44, pp. 17830-17837, 2019/11/06 2019, doi: 10.1021/jacs.9b09009.
- [112] X. Xu and Y.-L. Hsieh, "Aqueous exfoliated graphene by amphiphilic nanocellulose and its application in moisture-responsive foldable actuators," *Nanoscale*, 10.1039/C9NR01602C vol. 11, no. 24, pp. 11719-11729, 2019, doi: 10.1039/C9NR01602C.
- [113] R. Koppolu, N. Blomquist, C. Dahlström, and M. Toivakka, "High-Throughput Processing of Nanographite–Nanocellulose-Based Electrodes for Flexible Energy Devices," Industrial & Engineering Chemistry Research, vol. 59, no. 24, pp. 11232-11240, 2020/06/17 2020, doi: 10.1021/acs.iecr.0c01112.
- [114] D. Bresser, D. Buchholz, A. Moretti, A. Varzi, and S. Passerini, "Alternative binders for sustainable electrochemical energy storage the transition to aqueous electrode processing and bio-derived polymers," *Energy & Environmental Science*, 10.1039/C8EE00640G vol. 11, no. 11, pp. 3096-3127, 2018, doi: 10.1039/C8EE00640G.
- [115] M. Casalegno, F. Castiglione, M. Passarello, A. Mele, S. Passerini, and G. Raos, "Association and Diffusion of Li+ in Carboxymethylcellulose Solutions for Environmentally Friendly Li-ion Batteries," *ChemSusChem*, vol. 9, no. 14, pp. 1804-1813, 2016, doi: https://doi.org/10.1002/cssc.201600160.
- [116] D. Shin, H. Park, and U. Paik, "Cross-linked poly(acrylic acid)-carboxymethyl cellulose and styrene-butadiene rubber as an efficient binder system and its physicochemical effects on a high energy density graphite anode for Li-ion batteries," *Electrochemistry Communications*, vol. 77, pp. 103-106, 2017/04/01/ 2017, doi: https://doi.org/10.1016/j.elecom.2017.02.018.
- [117] W. Haselrieder, S. Ivanov, D. K. Christen, H. Bockholt, and A. Kwade, "Impact of the Calendering Process on the Interfacial Structure and the Related Electrochemical Performance of Secondary Lithium-Ion Batteries," *ECS Transactions*, vol. 50, no. 26, p. 59, 2013/04/01 2013, doi: 10.1149/05026.0059ecst.

- [118] O. El Baradai et al., "Microfibrillated Cellulose Based Ink for Eco-Sustainable Screen Printed Flexible Electrodes in Lithium Ion Batteries," *Journal of Materials Science & Technology*, vol. 32, no. 6, pp. 566-572, 2016/06/01/ 2016, doi: https://doi.org/10.1016/j.jmst.2016.02.010.
- [119] K. Park *et al.*, "Improved Li-ion kinetics of the anode by kneading process of binder for lithium-ion batteries with high energy density," *Electrochimica Acta,* vol. 464, p. 142900, 2023/10/01/ 2023, doi: https://doi.org/10.1016/j.electacta.2023.142900.
- [120] S. Byun et al., "Alkali Metal Ion Substituted Carboxymethyl Cellulose as Anode Polymeric Binders for Rapidly Chargeable Lithium-Ion Batteries," *ENERGY & ENVIRONMENTAL MATERIALS*, vol. 7, no. 1, p. e12509, 2024, doi: https://doi.org/10.1002/eem2.12509.
- [121] K. C. Kil and U. Paik, "Lithium salt of carboxymethyl cellulose as an aqueous binder for thick graphite electrode in lithium ion batteries," *Macromolecular Research*, vol. 23, no. 8, pp. 719-725, 2015/08/01 2015, doi: 10.1007/s13233-015-3094-1.
- [122] D. O. Shin *et al.*, "Electrolyte-free graphite electrode with enhanced interfacial conduction using Li+-conductive binder for high-performance all-solid-state batteries," *Energy Storage Materials*, vol. 49, pp. 481-492, 2022/08/01/ 2022, doi: https://doi.org/10.1016/j.ensm.2022.04.029.
- [123] H. S. Françon, Y. C. Gorur, C. Montanari, P. A. Larsson, and L. Wågberg, "Toward Li-ion Graphite Anodes with Enhanced Mechanical and Electrochemical Properties Using Binders from Chemically Modified Cellulose Fibers," *ACS Applied Energy Materials*, vol. 5, no. 8, pp. 9333-9342, 2022/08/22 2022, doi: 10.1021/acsaem.2c00525.
- [124] C. Wang, M. Tian, Y. Xin, X. Zhang, and X. Yang, "Self-supporting three-dimensional carboxymethyl cellulose conductive sponges used as electrodes for lithium-ion batteries," *Cellulose*, vol. 26, no. 13, pp. 8025-8036, 2019/09/01 2019, doi: 10.1007/s10570-019-02644-1.
- [125] L. Wang *et al.*, "Recent advances in interface engineering of silicon anodes for enhanced lithium-ion battery performance," *Energy Storage Materials*, vol. 66, p. 103243, 2024/02/25/ 2024, doi: https://doi.org/10.1016/j.ensm.2024.103243.
- [126] L. Jabbour, D. Chaussy, D. Beneventi, M. Destro, N. Penazzi, and C. Gerbaldi, "Use of paper-making techniques for the production of Li-ion paper-batteries," *Nordic Pulp & Paper Research Journal*, vol. 27, no. 2, pp. 472-475, 2012, doi: doi:10.3183/npprj-2012-27-02-p472-475.
- [127] L. Jabbour, M. Destro, C. Gerbaldi, D. Chaussy, N. Penazzi, and D. Beneventi, "Aqueous processing of cellulose based paper-anodes for flexible Li-ion batteries," *Journal of Materials Chemistry*, 10.1039/C2JM15117K vol. 22, no. 7, pp. 3227-3233, 2012, doi: 10.1039/C2JM15117K.
- [128] L. Jabbour et al., "Cellulose/graphite/carbon fibres composite electrodes for Li-ion batteries," Composites Science and Technology, vol. 87, pp. 232-239, 2013/10/18/2013, doi: https://doi.org/10.1016/j.compscitech.2013.07.029.
- [129] D. Beneventi *et al.*, "Pilot-scale elaboration of graphite/microfibrillated cellulose anodes for Li-ion batteries by spray deposition on a forming paper sheet," *Chemical Engineering Journal*, vol. 243, pp. 372-379, 2014/05/01/ 2014, doi: https://doi.org/10.1016/j.cej.2013.12.034.

- [130] B. Lu, A. Xu, and J. Wang, "Cation does matter: how cationic structure affects the dissolution of cellulose in ionic liquids," *Green Chemistry*, 10.1039/C3GC41733F vol. 16, no. 3, pp. 1326-1335, 2014, doi: 10.1039/C3GC41733F.
- [131] T. Zhao, P. Xiao, M. Luo, S. Nie, F. Li, and Y. Liu, "Eco-Friendly Lithium Separators: A Frontier Exploration of Cellulose-Based Materials," *International Journal of Molecular Sciences*, vol. 25, no. 13, p. 6822, 2024. [Online]. Available: https://www.mdpi.com/1422-0067/25/13/6822.
- [132] J. Drofenik *et al.*, "Cellulose as a binding material in graphitic anodes for Li ion batteries: a performance and degradation study," *Electrochimica Acta*, vol. 48, no. 7, pp. 883-889, 2003/02/20/ 2003, doi: https://doi.org/10.1016/S0013-4686(02)00784-3.
- [133] R. Stephanie, C. Y. Park, P. A. Shinde, E. Alhajri, N. R. Chodankar, and T. J. Park, "Aqueous aluminum ion system: A future of sustainable energy storage device," *Energy Storage Materials*, vol. 68, p. 103336, 2024/04/01/ 2024, doi: https://doi.org/10.1016/j.ensm.2024.103336.
- [134] R. Borah, F. R. Hughson, J. Johnston, and T. Nann, "On battery materials and methods," *Materials Today Advances*, vol. 6, p. 100046, 2020/06/01/ 2020, doi: https://doi.org/10.1016/j.mtadv.2019.100046.
- [135] G. A. Elia *et al.*, "Insights into the reversibility of aluminum graphite batteries," *Journal of Materials Chemistry A*, 10.1039/C7TA01018D vol. 5, no. 20, pp. 9682-9690, 2017, doi: 10.1039/C7TA01018D.
- [136] T. Dutta and J. Mary Gladis, "Recent developments on electrode materials and electrolytes for aluminium-ion batteries," *Journal of Energy Storage*, vol. 86, p. 111287, 2024/05/10/ 2024, doi: https://doi.org/10.1016/j.est.2024.111287.
- [137] T. Schoetz, B. Craig, C. Ponce de Leon, A. Bund, M. Ueda, and C. T. J. Low, "Aluminium-poly(3,4-ethylenedioxythiophene) rechargeable battery with ionic liquid electrolyte," *Journal of Energy Storage*, vol. 28, p. 101176, 2020/04/01/ 2020, doi: https://doi.org/10.1016/j.est.2019.101176.
- [138] L. Geng, G. Lv, X. Xing, and J. Guo, "Reversible Electrochemical Intercalation of Aluminum in Mo6S8," *Chemistry of Materials*, vol. 27, no. 14, pp. 4926-4929, 2015/07/28 2015, doi: 10.1021/acs.chemmater.5b01918.
- [139] L. W. Gordon, A. L. Jadhav, M. Miroshnikov, T. Schoetz, G. John, and R. J. Messinger, "Molecular-Scale Elucidation of Ionic Charge Storage Mechanisms in Rechargeable Aluminum–Quinone Batteries," *The Journal of Physical Chemistry C*, vol. 126, no. 33, pp. 14082-14093, 2022/08/25 2022, doi: 10.1021/acs.jpcc.2c04272.
- [140] H. Wang et al., "Binder-Free V2O5 Cathode for Greener Rechargeable Aluminum Battery," ACS Applied Materials & Interfaces, vol. 7, no. 1, pp. 80-84, 2015/01/14 2015, doi: 10.1021/am508001h.
- [141] Y. Hu et al., "A Binder-Free and Free-Standing Cobalt Sulfide@Carbon Nanotube Cathode Material for Aluminum-Ion Batteries," *Advanced Materials*, vol. 30, no. 2, p. 1703824, 2018, doi: https://doi.org/10.1002/adma.201703824.
- [142] T. Cai et al., "Stable CoSe2/carbon nanodice@reduced graphene oxide composites for high-performance rechargeable aluminum-ion batteries," Energy & Environmental Science, 10.1039/C8EE00822A vol. 11, no. 9, pp. 2341-2347, 2018, doi: 10.1039/C8EE00822A.

- [143] S. Wang, K. V. Kravchyk, F. Krumeich, and M. V. Kovalenko, "Kish Graphite Flakes as a Cathode Material for an Aluminum Chloride–Graphite Battery," *ACS Applied Materials & Interfaces*, vol. 9, no. 34, pp. 28478-28485, 2017/08/30 2017, doi: 10.1021/acsami.7b07499.
- [144] Y. Li, Y. Lu, P. Adelhelm, M.-M. Titirici, and Y.-S. Hu, "Intercalation chemistry of graphite: alkali metal ions and beyond," *Chemical Society Reviews*, 10.1039/C9CS00162J vol. 48, no. 17, pp. 4655-4687, 2019, doi: 10.1039/C9CS00162J.
- [145] Y. Zhang, S. Liu, Y. Ji, J. Ma, and H. Yu, "Emerging Nonaqueous Aluminum-Ion Batteries: Challenges, Status, and Perspectives," *Advanced Materials*, vol. 30, no. 38, p. 1706310, 2018, doi: https://doi.org/10.1002/adma.201706310.
- [146] S. Wang *et al.*, "Aluminum Chloride-Graphite Batteries with Flexible Current Collectors Prepared from Earth-Abundant Elements," *Advanced Science*, vol. 5, no. 4, p. 1700712, 2018, doi: https://doi.org/10.1002/advs.201700712.
- [147] P. Bhauriyal, A. Mahata, and B. Pathak, "The staging mechanism of AlCl4 intercalation in a graphite electrode for an aluminium-ion battery," *Physical Chemistry Chemical Physics*, 10.1039/C7CP00453B vol. 19, no. 11, pp. 7980-7989, 2017, doi: 10.1039/C7CP00453B.
- [148] M. S. Wu, B. Xu, L. Q. Chen, and C. Y. Ouyang, "Geometry and fast diffusion of AlCl4 cluster intercalated in graphite," *Electrochim. Acta*, vol. 195, p. 158, 2016, doi: 10.1016/j.electacta.2016.02.144.
- [149] M. C. C. Lin and Others, "An ultrafast rechargeable aluminium-ion battery," *Nature*, vol. 520, p. 324, 2015, doi: 10.1038/nature14340.
- [150] O. M. Leung *et al.*, "Solid Polymer Electrolytes with Enhanced Electrochemical Stability for High-Capacity Aluminum Batteries," *Advanced Energy Materials*, vol. 14, no. 8, p. 2303285, 2024, doi: https://doi.org/10.1002/aenm.202303285.
- [151] T. Schoetz, C. P. de Leon, M. Ueda, and A. Bund, "Perspective—State of the Art of Rechargeable Aluminum Batteries in Non-Aqueous Systems," *Journal of The Electrochemical Society*, vol. 164, no. 14, p. A3499, 2017/11/14 2017, doi: 10.1149/2.0311714jes.
- [152] E. Jónsson, "Ionic liquids as electrolytes for energy storage applications A modelling perspective," *Energy Storage Materials*, vol. 25, pp. 827-835, 2020/03/01/ 2020, doi: https://doi.org/10.1016/j.ensm.2019.08.030.
- [153] P. Gaijon, A. Kant, S. Ghosh, and M. R. Singh, "Chapter 19 Progressive function of ionic liquids in polymer chemistry," in *Advanced Applications of Ionic Liquids*, J. A. Siddique, S. P. Ansari, A. A. P. Khan, and A. M. Asiri Eds.: Elsevier, 2023, pp. 479-495.
- [154] T. Schoetz, O. Leung, C. P. de Leon, C. Zaleski, and I. Efimov, "Aluminium Deposition in EMImCl-AlCl3 Ionic Liquid and Ionogel for Improved Aluminium Batteries," *Journal of The Electrochemical Society*, vol. 167, no. 4, p. 040516, 2020/02/21 2020, doi: 10.1149/1945-7111/ab7573.
- [155] O. M. Leung, T. Schoetz, T. Prodromakis, and C. Ponce de Leon, "Review—Progress in Electrolytes for Rechargeable Aluminium Batteries," *Journal of The Electrochemical Society*, vol. 168, no. 5, p. 056509, 2021/05/12 2021, doi: 10.1149/1945-7111/abfb36.
- [156] B. Craig, T. Schoetz, A. Cruden, and C. Ponce de Leon, "Review of current progress in non-aqueous aluminium batteries," *Renewable and Sustainable Energy Reviews*, vol. 133, p. 110100, 2020/11/01/ 2020, doi: https://doi.org/10.1016/j.rser.2020.110100.

- [157] J. H. Xu, D. E. Turney, A. L. Jadhav, and R. J. Messinger, "Effects of graphite structure and ion transport on the electrochemical properties of rechargeable aluminum-graphite batteries," *ACS Appl. Energy Mater.*, vol. 2, p. 7799, 2019, doi: 10.1021/acsaem.9b01184.
- [158] J. V. Rani, V. Kanakaiah, T. Dadmal, M. S. Rao, and S. Bhavanarushi, "Fluorinated Natural Graphite Cathode for Rechargeable Ionic Liquid Based Aluminum–Ion Battery," *Journal of The Electrochemical Society*, vol. 160, no. 10, p. A1781, 2013/08/20 2013, doi: 10.1149/2.072310jes.
- [159] J. Yu et al., "Pencil-Drawing Graphite Nanosheets: A Simple and Effective Cathode for High-Capacity Aluminum Batteries," Small Methods, vol. 6, no. 4, p. 2200026, 2022, doi: https://doi.org/10.1002/smtd.202200026.
- [160] Y. Wu *et al.*, "3D Graphitic Foams Derived from Chloroaluminate Anion Intercalation for Ultrafast Aluminum-Ion Battery," *Advanced Materials*, vol. 28, no. 41, pp. 9218-9222, 2016, doi: https://doi.org/10.1002/adma.201602958.
- [161] H. Huang *et al.*, "Design and construction of few-layer graphene cathode for ultrafast and high-capacity aluminum-ion batteries," *Energy Storage Mater.*, vol. 27, p. 396, 2020, doi: 10.1016/j.ensm.2020.02.011.
- [162] L. Zhang, L. Chen, H. Luo, X. Zhou, and Z. Liu, "Large-Sized Few-Layer Graphene Enables an Ultrafast and Long-Life Aluminum-Ion Battery," *Advanced Energy Materials*, vol. 7, no. 15, p. 1700034, 2017, doi: https://doi.org/10.1002/aenm.201700034.
- [163] Y. Gao, C. Zhu, Z. Chen, and G. Lu, "Understanding Ultrafast Rechargeable Aluminumlon Battery from First-Principles," *The Journal of Physical Chemistry C*, vol. 121, no. 13, pp. 7131-7138, 2017/04/06 2017, doi: 10.1021/acs.jpcc.7b00888.
- [164] J. H. Xu, T. Schoetz, J. R. McManus, V. R. Subramanian, P. W. Fields, and R. J. Messinger, "Tunable Pseudocapacitive Intercalation of Chloroaluminate Anions into Graphite Electrodes for Rechargeable Aluminum Batteries," *Journal of The Electrochemical Society*, vol. 168, no. 6, p. 060514, 2021/06/08 2021, doi: 10.1149/1945-7111/ac0648.
- [165] W.-L. Song, S. Li, G. Zhang, J. Tu, H.-S. Chen, and S. Jiao, "Cellulose-derived flake graphite as positive electrodes for Al-ion batteries," *Sustainable Energy & Fuels*, 10.1039/C9SE00656G vol. 3, no. 12, pp. 3561-3568, 2019, doi: 10.1039/C9SE00656G.
- [166] K. V. Kravchyk, S. Wang, L. Piveteau, and M. V. Kovalenko, "Efficient aluminum chloride-natural graphite battery," *Chem. Mater.*, vol. 29, p. 4484, 2017, doi: 10.1021/acs.chemmater.7b01060.
- [167] , "Mass Transport," in *Electrochemistry of Metal Complexes*, 2015, pp. 33-59.
- [168] A. J. Bard, L. R. Faulkner, and H. S. White, *Electrochemical methods: fundamentals and applications*. John Wiley & Sons, 2022.
- [169] T. Schoetz, L. W. Gordon, S. Ivanov, A. Bund, D. Mandler, and R. J. Messinger, "Disentangling faradaic, pseudocapacitive, and capacitive charge storage: A tutorial for the characterization of batteries, supercapacitors, and hybrid systems," *Electrochimica Acta*, vol. 412, p. 140072, 2022/04/20/ 2022, doi: https://doi.org/10.1016/j.electacta.2022.140072.
- [170] Y. Jiang and J. Liu, "Definitions of Pseudocapacitive Materials: A Brief Review," *ENERGY & ENVIRONMENTAL MATERIALS*, vol. 2, no. 1, pp. 30-37, 2019, doi: https://doi.org/10.1002/eem2.12028.

- [171] M. Wang et al., "Introducing a Pseudocapacitive Lithium Storage Mechanism into Graphite by Defect Engineering for Fast-Charging Lithium-Ion Batteries," ACS Applied Materials & Interfaces, vol. 14, no. 14, pp. 16279-16288, 2022/04/13 2022, doi: 10.1021/acsami.2c02169.
- [172] J. Wang, J. Polleux, J. Lim, and B. Dunn, "Pseudocapacitive contributions to electrochemical energy storage in TiO 2 (Anatase) nanoparticles," *J. Phys. Chem. C*, vol. 111, p. 14925, 2007, doi: 10.1021/jp074464w.
- [173] K. L. Briggman and D. D. Bock, "Volume electron microscopy for neuronal circuit reconstruction," *Current Opinion in Neurobiology*, vol. 22, no. 1, pp. 154-161, 2012/02/01/ 2012, doi: https://doi.org/10.1016/j.conb.2011.10.022.
- [174] D. Massiot *et al.*, "Modelling one- and two-dimensional solid-state NMR spectra," *Magnetic Resonance in Chemistry*, vol. 40, no. 1, pp. 70-76, 2002, doi: https://doi.org/10.1002/mrc.984.
- [175] L. Liu and D. Mandler, "Electrochemical Deposition of Sol-Gel Films," in *Handbook of Sol-Gel Science and Technology: Processing, Characterization and Applications*, L. Klein, M. Aparicio, and A. Jitianu Eds. Cham: Springer International Publishing, 2018, pp. 531-568.
- [176] L. Liu and D. Mandler, "Sol–Gel Coatings by Electrochemical Deposition," in *The Sol-Gel Handbook*, 2015, pp. 373-414.
- [177] T. N. Myasoedova, R. Kalusulingam, and T. S. Mikhailova, "Sol-Gel Materials for Electrochemical Applications: Recent Advances," *Coatings*, vol. 12, no. 11, p. 1625, 2022. [Online]. Available: https://www.mdpi.com/2079-6412/12/11/1625.
- [178] T. Enoki, M. Endo, M. Suzuki, T. Enoki, M. Endo, and M. Suzuki, "GICs and Batteries," in *Graphite Intercalation Compounds and Applications*: Oxford University Press, 2003, sec. Oxford Academic, p. 0.
- [179] M. Noel and R. Santhanam, "Electrochemistry of graphite intercalation compounds," Journal of Power Sources, vol. 72, no. 1, pp. 53-65, 1998/03/30/ 1998, doi: https://doi.org/10.1016/S0378-7753(97)02675-X.
- [180] L. Rabinovich, J. Gun, O. Lev, D. Aurbach, B. Markovsky, and M. D. Levi, "Sol-Gel-Derived Carbon Ceramic Electrodes: A New Lithium Intercalation Anode," *Advanced Materials*, vol. 10, no. 8, pp. 577-580, 1998, doi: https://doi.org/10.1002/(SICI)1521-4095(199805)10:8<577::AID-ADMA577>3.0.CO;2-1.
- [181] W. Tang *et al.*, "Aqueous rechargeable lithium batteries as an energy storage system of superfast charging," *Energy & Environmental Science*, 10.1039/C3EE24249H vol. 6, no. 7, pp. 2093-2104, 2013, doi: 10.1039/C3EE24249H.
- [182] T. Placke and M. Winter, "Boosting Aqueous Batteries by Conversion-Intercalation Graphite Cathode Chemistry," *Joule*, vol. 3, no. 5, pp. 1184-1187, 2019/05/15/ 2019, doi: https://doi.org/10.1016/j.joule.2019.04.007.
- [183] E. S. Ferreira, D. S. da Silva, T. A. L. Burgo, B. C. Batista, and F. Galembeck, "Graphite exfoliation in cellulose solutions," *Nanoscale*, 10.1039/C7NR02365K vol. 9, no. 29, pp. 10219-10226, 2017, doi: 10.1039/C7NR02365K.
- [184] M. I. H. Mondal, M. S. Yeasmin, and M. S. Rahman, "Preparation of food grade carboxymethyl cellulose from corn husk agrowaste," *International Journal of Biological Macromolecules*, vol. 79, pp. 144-150, 2015/08/01/ 2015, doi: https://doi.org/10.1016/j.ijbiomac.2015.04.061.

- [185] L.-L. Tan, W.-J. Ong, S.-P. Chai, and A. R. Mohamed, "Reduced graphene oxide-TiO2 nanocomposite as a promising visible-light-active photocatalyst for the conversion of carbon dioxide," *Nanoscale Research Letters*, vol. 8, no. 1, p. 465, 2013/11/06 2013, doi: 10.1186/1556-276X-8-465.
- [186] B. Arkles and G. Larson, Silicon Compounds: Silanes & Silicones. 2013.
- [187] E. Herth, R. Zeggari, J.-Y. Rauch, F. Remy-Martin, and W. Boireau, "Investigation of amorphous SiOx layer on gold surface for Surface Plasmon Resonance measurements," *Microelectronic Engineering*, vol. 163, pp. 43-48, 2016/09/01/ 2016, doi: https://doi.org/10.1016/j.mee.2016.04.014.
- [188] S. San, Á. del Prado, F. Martinez-Viviente, I. Mártil, D. Bravo, and F. López, "Rapid thermal annealing effects on the structural properties and density of defects in SiO2 and SiNx: H films deposited by electron cyclotron resonance," *Journal of Applied Physics*, vol. 87, pp. 1187-1192, 02/01 2000.
- [189] B. C. Smith, "The C=O bond, part III: Carboxylic acids," *Spectroscopy (Santa Monica)*, vol. 33, pp. 14-20, 03/01 2018.
- [190] J. H. Xu, A. L. Jadhav, D. E. Turney, and R. J. Messinger, "Molecular-level environments of intercalated chloroaluminate anions in rechargeable aluminum-graphite batteries revealed by solid-state NMR spectroscopy," *J. Mater. Chem. A*, vol. 8, p. 16006, 2020, doi: 10.1039/D0TA02611E.
- [191] Z. Zhang *et al.*, "Characterizing Batteries by In Situ Electrochemical Atomic Force Microscopy: A Critical Review," *Advanced Energy Materials*, vol. 11, no. 38, p. 2101518, 2021, doi: https://doi.org/10.1002/aenm.202101518.
- [192] A. Valizadeh and M. H. Amirhosseini, "Machine Learning in Lithium-Ion Battery: Applications, Challenges, and Future Trends," *SN Computer Science*, vol. 5, no. 6, p. 717, 2024/07/22 2024, doi: 10.1007/s42979-024-03046-2.
- [193] C. Chen, Y. Zuo, W. Ye, X. Li, Z. Deng, and S. P. Ong, "A Critical Review of Machine Learning of Energy Materials," *Advanced Energy Materials*, vol. 10, no. 8, p. 1903242, 2020, doi: https://doi.org/10.1002/aenm.201903242.
- [194] Z. Zhao and H. Wu, "Monolithic integration of flexible lithium-ion battery on a plastic substrate by printing methods," *Nano Research*, vol. 12, no. 10, pp. 2477-2484, 2019/10/01 2019, doi: 10.1007/s12274-019-2471-z.
- [195] M. Koo et al., "Bendable Inorganic Thin-Film Battery for Fully Flexible Electronic Systems," Nano Letters, vol. 12, no. 9, pp. 4810-4816, 2012/09/12 2012, doi: 10.1021/nl302254v.